Spin structure of the nucleon at low x and Q^2 in the COMPASS experiment at CERN

Marcin Stolarski

Ph.D. thesis
performed under supervision of Professor Barbara Badełek

Faculty of Physics, Warsaw University

Warsaw 2006

Abstract

COMPASS is an experiment at CERN, which uses a polarized secondary muon beam of 160 GeV energy and a polarized ^{6}LiD target. In this thesis the results concerning the spin dependent cross section asymmetry A_1^d and spin dependent structure function g_1^d obtained from COMPASS 2002 and 2003 data are presented. The A_1^d was extracted in a wide kinematic range: $x \in (1.6 \cdot 10^{-5} - 0.6)$ and $Q^2 \in (10^{-3} - 100)$ GeV^2 and found consistent with zero for $x < 0.01$. In case of the g_1^d structure function the above kinematic range was restricted to $Q^2 < 1$ GeV^2. So far the only experiment which measured g_1^d below $x < 0.01$ was the SMC. For $x < 0.002$ the statistical errors obtained here are ten times smaller than those of the SMC. Due to this high precision a special attention was given to studies of systematic uncertainties. In particular the software alignment of the COMPASS spectrometer needed to reduce systematic errors is described in details. Finally the g_1^d was confronted with the Regge model but the comparison was inconclusive.

Contents

Chapter 1

Introduction

Discovery of the atom core, called nucleus, by Rutherford in 1911 begins a modern era of understanding the structure of matter. At the beginning of the 1930s it became known that in the nucleus there are nucleons: protons and neutrons. For many years these two varieties were called elementary particles, *i.e.* particles without internal structure. As time passed more and more such "elementary particles", the so called hadrons, were discovered. Presently their number exceeds a few hundred. In 1964 Gell-Mann proposed a quark concept [1] so that all the known hadrons were supposed to be built of three quarks or a quark–antiquark pair. At that time only three quark types were needed: *up*, *down* and *strange*, to built up all known hadrons. Soon theorists postulated that a new quark type the so called *charm* quark should exist. Indeed a few years later in 1974 a J/Ψ meson, built of charm quark–antiquark pair, was discovered [2], [3]. Only after this discovery the quark concept was widely accepted.

In the late 1960s the energy of the electron beams was high enough that the internal structure of the nucleons could be studied. Results of the Deep Inelastic Scattering (DIS) pointed towards a hypothesis that inside nucleons there are point-like objects called partons [4]. They were soon related to the quarks.

In the middle of 1970s the first DIS experiments with polarized beams started to operate at SLAC: E80 [5] and E130 [6] to investigate a new degree of freedom, the spin. They were initiated by V.W. Hughes. Polarized DIS experiments were later continued at CERN by the European Muon Collaboration (EMC). The EMC discovered [7], [8] that the Ellis-Jaffe sum rule [9] is violated, a fact known as a "spin-crisis". In the simplest approach of the Quark Parton Model (QPM) in the nucleon there are three valence quarks, which have spin equal 1/2. The spin of two quarks is parallel to the nucleon spin and one quark has its spin anti–parallel. In this way a nucleon spin equal 1/2 is recovered. In this simplest approach the quantity which measures a fraction of the nucleon spin carried by the quarks, $\Delta\Sigma$, is equal to 1. Taking into account relativistic effects, $\Delta\Sigma \approx 0.6$ is expected [10]. A value measured by the EMC was $\Delta\Sigma = 0.12 \pm 0.09 \pm 0.14$, far from the expectations. It was a surprise as the QPM successfully described *e.g.* hadron charges, their anomalous magnetic moments and mass differences between hadrons. Further experiments, *i.e.* Spin Muon Collaboration (SMC) [11] at CERN, E142 [12], E143 [13], E154 [14], E155 [15] at SLAC and HERMES [16], [17] at DESY confirmed the EMC observation with a better accuracy.

In a more realistic approach the spin of the nucleon may be carried by quarks, $\Delta\Sigma$, gluons, ΔG, and by orbital momentum of quarks and gluons, L_q, L_g respectively.

$$\frac{1}{2} = \frac{1}{2}\Delta\Sigma + \Delta G + L_q + L_g \tag{1.1}$$

The main goal of the COMPASS[1] experiment [18] at CERN is a precise measurement of ΔG. Among its other physics goals there are studies of the spin dependent structure function g_1 of the proton and the deuteron, flavour dependent quark polarization in a nucleon and parton distributions in a transversally polarized target.

In this thesis results of the A_1^d and g_1^d measurements at the low x and low Q^2 from 2002 and 2003 runs are given. The measurements were performed in a wide kinematic range $x \in (1.6 \cdot 10^{-5} - 0.6)$ and $Q^2 \in (10^{-3} - 100)$ GeV^2. So far the region $10^{-4} < x < 0.01$ was only explored by the SMC [19] (for details see [20]). In the analysis the author used the data which were already reconstructed.

A successful reconstruction procedure depends strongly on the correct software alignment of the detector. The author was responsible for this procedure during two years of data taking, when he was supported by the Bonn University. In the A_1^d and g_1^d analysis at low Q^2 the author selected the proper data sample, implemented the asymmetry extraction methods into a computer program, and performed extended systematic studies of the A_1^d and g_1^d. Most of external information needed for the A_1^d and g_1^d extraction was taken from standard COMPASS programs.

Most of the analysed data belong to the non-perturbative region, $Q^2 < 1$ GeV^2 where QCD cannot be applied. Therefore they cannot be used for $\Delta\Sigma$ measurements. However, the knowledge of g_1 is important in the whole phase space and not only for $Q^2 > 1$ GeV^2. In the low x and low Q^2 region new phenomena are expected; there are also theoretical predictions about g_1 behaviour in the non-perturbative region. Finally even though QCD cannot be used for low Q^2 our ultimate goal is to strive for understanding the nucleon structure as a whole including the problem of confinement.

The structure of this thesis is the following. In chapter 2 the formalism of DIS is introduced and the spin dependent and spin independent structure functions are discussed. The description of the COMPASS detector is presented in chapter 3. The alignment procedure used in COMPASS is described in chapter 4. Chapter 5 deals with the data analysis where data selection and systematic studies are discussed in details. Finally the results for the A_1^d and g_1^d are given in chapter 6. There also the g_1^d comparison with the Regge model is presented. Natural units, *i.e.* $\hbar c = 1$, are used everywhere.

[1] COMPASS is an acronym for COmmon Muon and Proton Apparatus for Structure and Spectroscopy.

Chapter 2

The Formalism

In this chapter a brief introduction to the Deep Inelastic Scattering (DIS) is given. Definitions of kinematic variables needed for the DIS description are presented. Then nucleon structure functions are introduced for the unpolarized (F_1, F_2) and the polarized (g_1, g_2) scattering. A connection between these functions and a cross section for the *virtual photon – nucleon* photo-absorption is given. Finally spin asymmetries A_1 and A_2 are introduced. They are functions of *virtual photon – nucleon* cross section and they are experimental observables.

2.1 Deep Inelastic Scattering and the structure functions

DIS is an interaction between a gauge boson and a component of a nucleon in a lepton–nucleon scattering $lN \to l'X$. After the interaction the initial nucleon is destroyed. In case of COMPASS the source of gauge bosons are muons and events can be mediated by two types of the gauge bosons: γ and Z^0. However, in COMPASS the energy in the μN centre of mass system is $\sqrt{s} \approx 17$ GeV, which is much less than the Z^0 mass, $M_{Z^0} \approx 92$ GeV. In such conditions the contribution from Z^0 is negligible compared to γ. Finally, the electromagnetic coupling constant, α, which describes the strength of the electromagnetic interaction is small, $\alpha \approx 1/137$. This means that in most of the interactions only one photon is exchanged, whereas a multi-photon exchanges are strongly suppressed, and can be neglected if the atomic number Z of the target nucleus is small, which is the case in COMPASS.

2.1.1 Kinematic variables

Two kinematic variables are needed to fully describe a DIS process at a given energy. Let us define four vectors of the incoming and scattered muon (k, k') and of the proton (p) in the laboratory system:

$$k = (E, \vec{k}) = (E, 0, 0, |\vec{k}|) \tag{2.1}$$

$$k' = (E', \vec{k'}) = (E', |\vec{k}| \sin\theta\cos\varphi, |\vec{k}| \sin\theta \sin\varphi, |\vec{k}| \cos\theta) \tag{2.2}$$

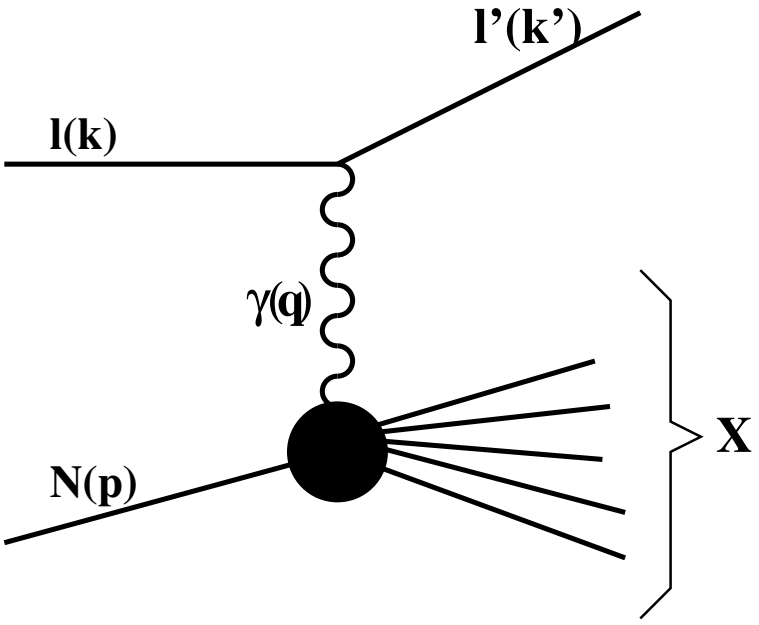

Figure 2.1: A basic Feynman diagram for a deep inelastic scattering of lepton off a nucleon $lN \to l'X$. Particles are characterized by the four-momenta, defined in section 2.1.1.

$$p = (E_p, \vec{p}) = (M, 0, 0, 0) \tag{2.3}$$

where E, E' are the initial and the final lepton energies, $\vec{k}, \vec{k'}$ are the three momenta of the incoming and the scattered muon and M is taken as the proton mass. The coordinate system of COMPASS was chosen in such a way that the 'z-axis' corresponds to the beam axis, 'y-axis' is in upward direction and 'x-axis' so at to make the system right-handed. The definition of the angles is presented in figure 2.2. In the figure there are also other angles, which are defined further in the text.

A natural way of describing a DIS process is using Lorentz invariant variables. Of the five listed below only two are independent:

$$Q^2 = -q^2 = (k - k')^2 \overset{lab}{=} 2(m^2 - EE' + |\vec{k}||\vec{k'}|\cos\theta) \tag{2.4}$$

$$\nu = \frac{pq}{M} \overset{lab}{=} E - E' \tag{2.5}$$

$$y = \frac{pq}{pk} \overset{lab}{=} \frac{\nu}{E} \tag{2.6}$$

$$x = \frac{Q^2}{2pq} \overset{lab}{=} \frac{Q^2}{2M\nu} \tag{2.7}$$

$$W^2 = (p+q)^2 = M^2 + 2M\nu - Q^2 = M^2 + Q^2\left(\frac{1}{x} - 1\right) \tag{2.8}$$

Here $-Q^2$ and ν are the squared mass of the virtual photon and its energy in the laboratory system, respectively. The dimensionless y is in range $y \in (0, 1)$, while $x \in (0, 1)$ is the Bjorken variable; its interpretation within the Quark Parton Model (QPM) was given by

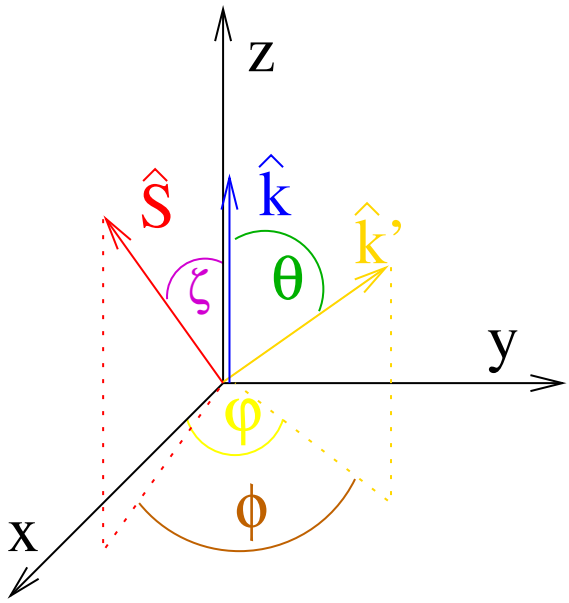

Figure 2.2: Definition of angles used in this thesis. See text for details.

Feynman [21]. According to it, x is a fraction of the nucleon momentum carried by the parton which interacted with the virtual photon. The definition holds in the so called infinite nucleon momentum frame, where partons do not have transverse momentum and their mass can be neglected. Finally, W^2 is the squared mass of the final hadron system. In DIS a photon is interacting with a component of a nucleon. Nucleon excitation process, possibly followed by its de–excitation are not DIS. In order to reduce a yield of these unwanted events W^2 should be larger than several GeV^2

2.1.2 Cross section and the structure functions

The differential cross section for a DIS process can be written [22] as:

$$\frac{d\sigma}{dE'd\Omega} = \frac{\alpha^2}{Q^2}\frac{E'}{ME}L_{\mu\nu}W^{\mu\nu} \tag{2.9}$$

where $L_{\mu\nu}, W^{\mu\nu}$ are four–rank lepton and hadron tensors. $L_{\mu\nu}$ describes a photon emission from the lepton and can be calculated using the QED formalism. $W^{\mu\nu}$ contains information about the structure of the nucleon. It cannot be fully calculated using the QCD formalism. Emission of the photon and its interaction with the nucleon are supposed to be independent processes[1]. These tensors can be decomposed into two parts: symmetric and anti-symmetric. The symmetric part of them governs the unpolarized scattering, while the anti-symmetric part depends upon the helicity of interacting particles and therefore describes the spin-dependent lepton-nucleon scattering. In order to measure the anti-symmetric tensor elements, both the beam and the target have to be polarized. In the case when only a γ interactions are considered and the current conservation at hadron vertex is assumed $W^{\mu\nu}$, can be parametrized by 4 independent functions [22]. The symmetric

[1] Therefore there are two independent tensors.

"unpolarized" part can be expressed in terms of the structure functions F_1 and F_2, while the "polarized" part in terms of g_1 and g_2. The functions cannot be obtained from the QCD, they have to be measured in experiments. The structure functions describe the internal structure of a nucleon. Due to the factorization of the QCD the functions are universal; measured in one process they can be used in a different one. This makes them very important observables, accessible only in the high energy physics experiments.

In COMPASS the polarized target has spin equal 1. In that case there are four additional structure functions denoted b_{1-4} [23]. However, these functions are expected to be small for the deuteron case [23], [24], therefore in this analysis they were neglected.

To summarize, in this thesis it is assumed that the total cross section (σ) depends upon the four structure functions. Two of them describe the unpolarized (spin-independent) scattering $\bar{\sigma}(F_1, F_2)$, the remaining two describe the cross section for the polarized scattering, $\Delta\sigma(g_1, g_2)$.

$$\sigma = \bar{\sigma} - \frac{1}{2} h_l \Delta\sigma \tag{2.10}$$

where h_l is the lepton helicity. The spin dependent cross section, $\Delta\sigma$, can be decomposed into a linear combination of two parts, $\sigma_{||}$ and $\sigma_{\perp}$:

$$\Delta\sigma = cos\zeta \Delta\sigma_{||} + \sin\zeta \cos\phi \Delta\sigma_{\perp} \tag{2.11}$$

where ζ, defined in figure 2.2, is an angle between spin vector of a nucleon S and z-axis. $\Delta\sigma_{||}$ denotes the cross section in a case where the two spins are mutually parallel (antiparallel) while $\Delta\sigma_{\perp}$ describes the case of mutually orthogonal spin vectors. In COMPASS both spin configurations are studied. In this thesis only data with $\zeta = 0$ or π and $h_l = -1$ are used.

the mutually parallel configuration of the spins are used.

2.1.3 Virtual photon-hadron scattering

Description of the lepton-hadron interaction may be rewritten using a formalism of virtual photon–hadron interaction. The cross section for that process may be described by a Compton scattering amplitudes. The amplitudes depend upon the helicity of the virtual photon and of the hadron. In a case of a spin-1/2 target there are four independent amplitudes, which govern the $\gamma^* N$ scattering; for spin-1 target there are already 8 such amplitudes [23]. All these amplitudes, and therefore cross sections are connected to the structure functions discussed in the previous paragraph:

$$\sigma_2^T(+1,+1;+1,+1) \sim F_1 - g_1 + (\kappa - 1) g_2 \tag{2.12}$$

$$\sigma_1^T(+1,0;+1,0) \sim F_1 \tag{2.13}$$

$$\sigma_0^T(+1,-1;+1,-1) \sim F_1 + g_1 - (\kappa - 1) g_2 \tag{2.14}$$

$$\sigma_1^{TL}(+1,0;0,+1) \approx \sigma_1^{TL}(+1,0;0,+1) \sim \sqrt{\kappa - 1}(g_1 + g_2) \tag{2.15}$$

$$\sigma_0^{TT}(+1,-1;-1+1) \sim 0 \tag{2.16}$$

$$\sigma_1^L(0,+1;0,+1) \approx \sigma_0^L(0,0;0,0) \sim -F_1 + \frac{\kappa}{2x} F_2 \tag{2.17}$$

where $\sigma_i^{\gamma_{pol}}(s_{\gamma^*}, s_N; s'_{\gamma^*}, s'_N)$ denotes the absorption cross section; $i = s_{\gamma^*} + s_N$ is the third component of the total angular momentum of the $\gamma^* N$ system; γ_{pol} denotes transverse and

longitudinal photon polarization; (s_{γ^*}, s_N) and (s'_{γ^*}, s'_N) are the third component of the spin vectors of the photon and of the hadron, before and after the interaction, respectively; κ is the kinematical factor equal to $1 + 4x^2M^2/Q^2 = 1 + 2xM/\nu = 1 + \gamma^2$. In the case of COMPASS κ is very close to 1. In all the above equations the structure functions b_{1-4} were omitted. If we define:

$$\sigma^T = (\sigma_0^T + \sigma_1^T + \sigma_2^T)/3 \tag{2.18}$$

and

$$\sigma^L = (\sigma_1^L + \sigma_0^L)/2 \tag{2.19}$$

then the ratio of two

$$R = \sigma^L/\sigma^T = \frac{\kappa}{2x}\frac{F_2}{F_1} - 1 \tag{2.20}$$

gives the R function, which will be used later.

2.1.4 The spin dependent cross section asymmetries and the structure functions

Let us define the A_1, A_2 spin dependent cross section asymmetries in a case of the spin-1 target as follows

$$A_1 = \frac{3}{2}\frac{\sigma_0^T - \sigma_2^T}{\sigma_0^T + \sigma_1^T + \sigma_2^T}, \quad A_2 = \frac{3}{2}\frac{\sigma_0^{TL} - \sigma_1^{TL}}{\sigma_0^T + \sigma_1^T + \sigma_2^T} \tag{2.21}$$

using equations (2.12) – (2.17) we get:

$$A_1 = \frac{g_1 - \gamma^2 g_2}{F_2}, \quad A_2 = \gamma\frac{g_1 + g_2}{F_1} \tag{2.22}$$

From the definition $|A_1| \leq 1$, whereas $|A_2| < \sqrt{\frac{1+A_1}{2}R}$, is the so called Soffer limit [25]. It is worth to mention that for A_1 and A_2 asymmetries the contributions from b_{1-4} cancel out [23].

The observable measured in COMPASS is in fact:

$$A_{||} = \frac{\Delta\sigma_{||}}{2\bar{\sigma}} = D(A_1 + \eta A_2) \tag{2.23}$$

where $D \in (0, 1)$ is a depolarization factor, which gives information about a spin transfer from the muon to the virtual photon. It is precisely defined and discussed in section 5.3.3. The quantity $\eta \approx \gamma\frac{1-y}{1-y/2}$ is small in the COMPASS case.

The A_2 asymmetry was measured in several experiments: E155X [26], E155 [27], E143 [28] at SLAC and the SMC [29] at CERN. Results of the A_2 measurements versus x are shown in figure 2.3. The figure comes from [26] where details are given. The dashed curve shows the Soffer limit of A_2. The solid line represents the A_2 values expected from the so called Wandzura-Wilczek relation [30].

The results show that the asymmetry is small, comparable to zero below $x = 0.05$. In equation (2.23) the A_2 asymmetry is multiplied by the factor η, which is small in the COMPASS case, therefore the term ηA_2 can be neglected in the expression for $A_{||}$. The

same is valid for the γA_2 factor, in the expression for the g_1 below which, follows from equation (2.22):

$$g_1 = \frac{F_1}{1+\gamma^2}(A_1 + \gamma A_2) \tag{2.24}$$

With the additional assumption that $\gamma^2 \approx 0$ one gets:

$$A_{||} \approx DA_1, \qquad g_1 \approx A_1 F_1 \approx A_1 \frac{F_2}{2x(1+R)} \tag{2.25}$$

Methods of the experimental determination of $A_{||}$ are given in sections 5.4 and A. The possible systematic effects connected to the neglecting of the A_2 asymmetry were taken into account in the systematic error of the measured A_1^d and g_1^d. Results of these studies are presented in section 5.7.7.

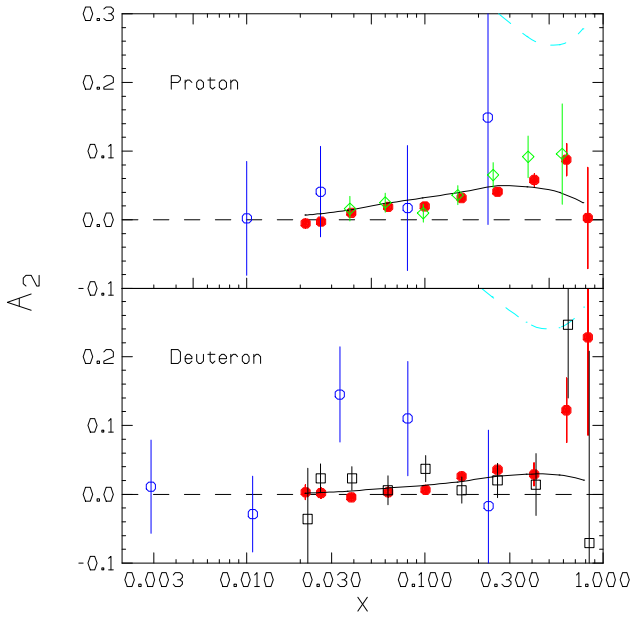

Figure 2.3: Asymmetry A_2 for proton and deuteron measured at SLAC by E155X [26] (solid circles), E143 [28] (diamonds), E155 [27] (open squares), and at CERN by the SMC [29] (open circles). The errors are statistical; the systematic errors are negligible. The plot comes from [26] where more details are given.

2.2 Structure functions

In this part of the thesis short description of structure functions is given. The emphasis is put on F_2 and g_1 structure functions. These functions are easier to measure in experiments, and therefore more precisely known, compared to their partners F_1 and g_2. The b_{1-4} structure functions are not discussed.

First the interpretation of the F_2 and g_1 in the QPM model is given. It is followed by scaling violation and QCD predictions for F_2 and g_1. Finally structure functions at low x and (or) low Q^2 region are briefly discussed.

2.2.1 F_1 and F_2 in QPM

QPM gives the simplest description of the internal structure of the nucleon. According to the model inside a nucleon there are partons: point–like particles, which do not interact with each other. The QPM model is defined in the so called "infinite momentum frame". In this frame nucleon momentum is very large, so that nucleon and parton masses can be neglected and in addition the partons do not have transverse momenta with respect to the nucleon momentum. In the DIS process a virtual photon interacts elastically with a parton, which carries a fraction x of the proton momentum, cf. section 2.1. The partons which can interact with a virtual photon are quarks. Gluons, which do not carry the electric charge, cannot interact with a photon directly.

In the simplest approach, the so called *naive* QPM, the nucleon is composed of three quarks. From the quantum number of these quarks all the quantum numbers of the nucleon should be reproduced. In QPM these quarks are called valence quarks. Apart of them in the nucleon there are gluons and the so called *sea* quarks. In the QPM the F_1 and F_2 can be defined as:

$$F_1(x) = \frac{1}{2x}F_2(x) = \frac{1}{2}\sum_i e_i^2 q_i(x) \tag{2.26}$$

where the sum is over all (anti)quark flavours. Here e_i is the electric charge of a quark of flavour i, $q_i(x)$ is proportional to the density probability of finding a parton of a flavour i with a fraction x of the nucleon momentum[2]. The $2xF_1 = F_2$ is the so called Callan-Gross relation [22]. The fact that F_1 and F_2 depend only on one variable, x, is the so called Bjorken scaling. For the first time it was observed at SLAC in the 60's [31].

It is more convenient to rewrite equation (2.26) to a form where the quark spin orientation with respect to the nucleon spin is explicitly shown. The quantities $q^+(x)$ and $q^-(x)$ are probability densities $q(x)$ for a parton with a spin parallel and anti-parallel to the spin of the nucleon, respectively. In case of spin–1 targets, *e.g.* a deuteron, an additional distribution $q^0(x)$ is needed. Its represents quarks which are polarized in the direction perpendicular to the direction of the target spin. As b_{1-4} are neglected then $2q^0(x) = q^+(x) + q^-(x)$ and equation (2.26) becomes:

$$F_1(x) = \frac{1}{2x}F_2(x) = \frac{1}{2}\sum_i e_i^2 (q_i^+(x) + q_i^-(x)) \tag{2.27}$$

which is the same for both spin–1/2 and spin–1 targets.

2.2.2 F_2 in QCD

Bjorken scaling was found to be violated. This violation is particularly strong in the low x region. For a constant x, increasing of Q^2 results in an increase of F_2. The latter can be explained as follows. Larger Q^2 means larger photon resolution. A parton which at lower Q^2 seemed to be a single quark, for larger Q^2 may be viewed *e.g.* as a quark which emitted a gluon which in turn converted into a $q\bar{q}$ pair. In this way the parton densities at low x increase with increasing Q^2. Analogously parton densities at large x are expected to decrease with Q^2.

[2]For simplicity $q_i(x)$ will be called the density probability further in the text.

The QCD predictions for the F_2 are based on the so called Dokshitzer-Gribov-Lipatov-Altarelli-Parisi evolution, DGLAP, [32], [33], [34] [35]: from a parton distribution known at one Q^2, one can obtain a parton distribution at any Q^2 provided the initial and final Q^2 values are larger than the QCD scale. Within the evolution formalism parton distributions can be approximated by:

$$p_0(x,Q^2) \sim \sum_{n=0}^{\infty} C_n^0(x)\alpha_s^n \left(\ln \frac{Q^2}{Q_0^2}\right)^n \tag{2.28}$$

where $p_0(x,Q^2)$ are parton densities[3], α_s is the strong coupling constant, $C_n^0(x)$ are calculable within the QCD formalism and Q_0^2 is a reference Q^2 value. This is the so called leading logarithm approximation; it is often referred to as the so called leading order. It is also possible to make further corrections to parton distributions, *e.g.* $p_1(x,Q^2) \sim p_0(x,Q^2) + \sum_{n=1}^{\infty} C_{n-1}^1 \alpha_s^n (lnQ^2/Q_0^2)^{n-1}$. These particular corrections are usually called next–to–leading logarithm approximation, often referred to as the next–to–leading order. More details can be found in [36].

Later it was proved [37], [38], [39], [40] that not only lnQ^2-type corrections are important but in addition C_n^i may be expressed as:

$$C_n^i(x) \sim \sum_{m=0}^{n} A_m^i \left(\ln \frac{1}{x}\right)^m \tag{2.29}$$

where A_m^i are calculable constants. It is evident that in the low x kinematic domain a sum of $A_m^i(\ln(1/x))^m$, for $m \neq 0$, may be non–negligible or even dominant. The evolution of parton distributions at fixed Q^2 is governed by the $(\ln(1/x))^m$ corrections, the so called Balitsky-Fadin-Kuraev-Lipatov evolution, BFKL, [37], [38], [39], [40]. The BFKL effects were searched for at HERA [41], [42], [43] and at the Tevatron [44] with inconclusive results. Finally the Ciafaloni-Catani-Fiorani-Marchesini evolution, CCFM, [45], [46], [47] unifies DGLAP and BFKL. As x decreases the parton densities become so large that the unitary would be broken. Therefore it is expected that a new phenomenon, the so called *saturation*, should occur in this region: the observed parton densities should be smaller than expected from DGLAP, BFKL or CCFM evolutions. This is included in the Gribov-Levin-Riskin, GLR, [48] formulation of the parton evolution. Different regions of the (x,Q^2) phase space and different evolution types are shown schematically in figure 2.4. The "size" and the density of partons are also indicated there.

2.2.3 F_2 at low Q^2

As Q^2 drops below $Q^2 \approx 1$ GeV^2 the α_s becomes so large that perturbative QCD cannot be used to describe the DIS process. A most commonly known F_2 description in this region is based on two theoretical concepts: the Regge model [49] and the (Generalized) Vector Meson Dominance models, (G)VMD, *e.g.* [50]. The Regge model is a generalization of the Yukawa concept concerning the nucleon-nucleon interactions. In the Regge model the hadron-hadron interaction is described by an exchange of the so called *Regge poles* in s or t channel. As an example the $\pi^- p \to \pi^0 n$ interaction may be described as an exchange of

[3]Index '0' indicates how much accurate approximation is used, higher value of the index indicate better approximation

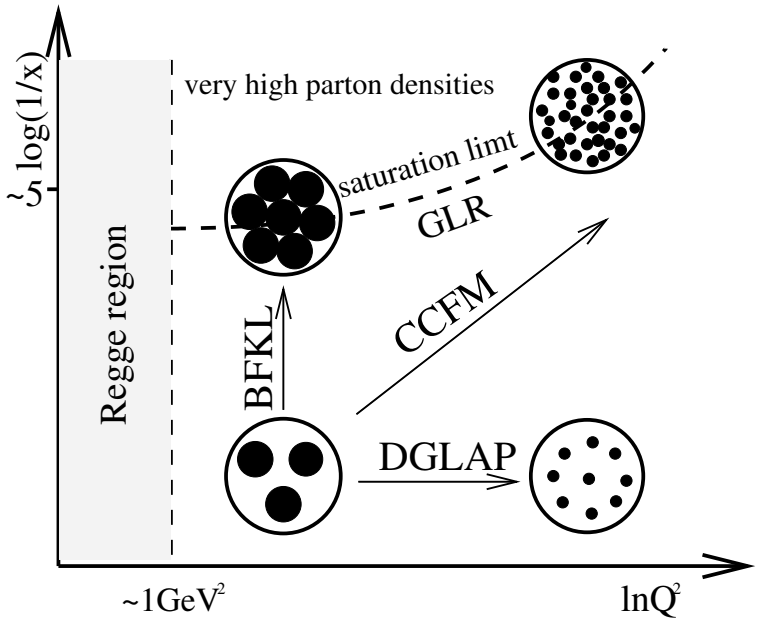

Figure 2.4: Schematic view of the different regimes in the QCD evolution of parton densities.

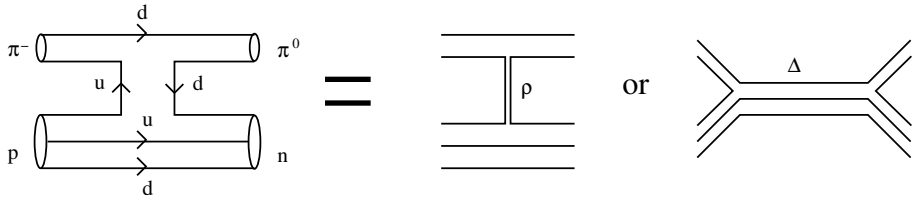

Figure 2.5: Regge model based description of the $\pi^- p \to \pi^0 n$ interaction by an exchange of ρ meson or Δ baryon. Figure comes from [51]

ρ meson or Δ baryon, cf. figure 2.5. An amplitude for such a process is: $A(s,t) \sim s^{\alpha(t)}$. Using an optical theorem one can connect the amplitude with the total cross section hence with the F_2. In general the structure function F_2 in the Regge model may be seen as:

$$F_2(W^2, Q^2) = \frac{4\pi\alpha}{Q^2} \sum_i \beta_i(Q^2)(W^2)^{\alpha_i(0)-1} \tag{2.30}$$

The sum is over all exchanged Regge poles and $\alpha_i(0)$ is the so called Regge intercept of the Regge trajectory $\alpha(t)$. The Regge model gives only F_2 energy (s or W^2) dependence but not its Q^2 dependence. The latter may be obtain *e.g.* from (G)VMD. In these models the virtual photon emitted from the lepton fluctuates into a vector meson, which interacts with the nucleon. According to the perturbative approach a photon fluctuation into a vector meson may travel a distance $d \sim 2E_\gamma/(Q^2 + M^2)$, where E_γ is the energy of the photon and M^2 is the mass of the vector meson. For a 100 GeV real photon a fluctuation into ρ meson can travel a distance around 80 fm, which is much more than the proton radius.

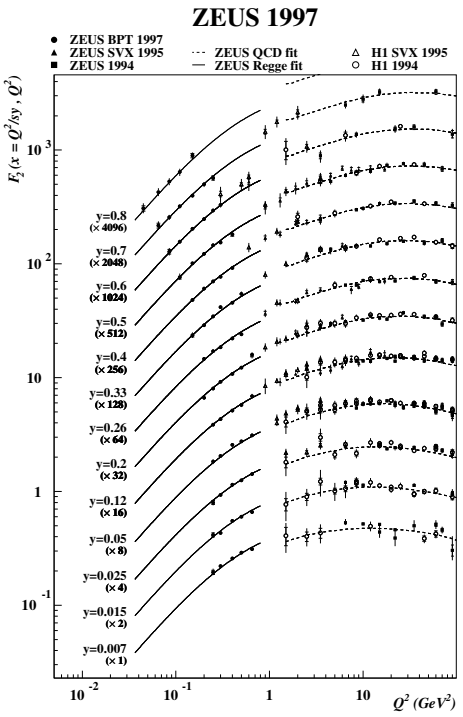

Figure 2.6: F_2 in the low x, low Q^2 region, HERA data. Figure is taken from [52].

Joining the Regge and (G)VMD concepts, the F_2 structure function in the low Q^2 region may be parametrized as [52]:

$$F_2(x,Q^2) = \left(\frac{Q^2}{4\pi^2\alpha}\right)\left(\frac{M_0^2}{M_0^2+Q^2}\right)\left(A_{\mathcal{R}}\left(\frac{Q^2}{x}\right)^{\alpha_{\mathcal{R}}-1} + A_{\mathcal{P}}\left(\frac{Q^2}{x}\right)^{\alpha_{\mathcal{P}}-1}\right) \tag{2.31}$$

where $A_{\mathcal{R}}$, $A_{\mathcal{R}}$, M_0 are constants, $M_0^2 \approx 1$ GeV^2, $\alpha_{\mathcal{R}} = 0.5$, $\alpha_{\mathcal{P}} = 1.08$ are the so called Reggeon and Pomeron[4] intercepts, respectively and $Q^2/x \approx W^2$. In figure 2.6 the HERA data [52] are shown, the solid line for $Q^2 < 1$ GeV^2 is the fit to the data based on equation (2.31). The shape of the data is well described by the fit. For $Q^2 > 1$ GeV^2, QCD predictions are shown (dashed line), which also agree well with the data.

2.2.4 Spin dependent structure function g_1

Contrary to the F_2 the g_1 spin dependent structure function is much less precisely measured. The main reason is that measurements were made only in the fixed target experiments, which have limited phase space: there are no large Q^2, especially for small x. The comparison of measurement quality for the F_2 and g_1 structure functions is presented in figure 2.7. In the figure data for $Q^2 > 1$ GeV^2 are shown together with QCD predictions.

In the QPM model the g_1 structure function has a form similar to the unpolarized

[4]The concept of the Pomeron pole was introduced to account for diffractive and elastic hadron scattering.

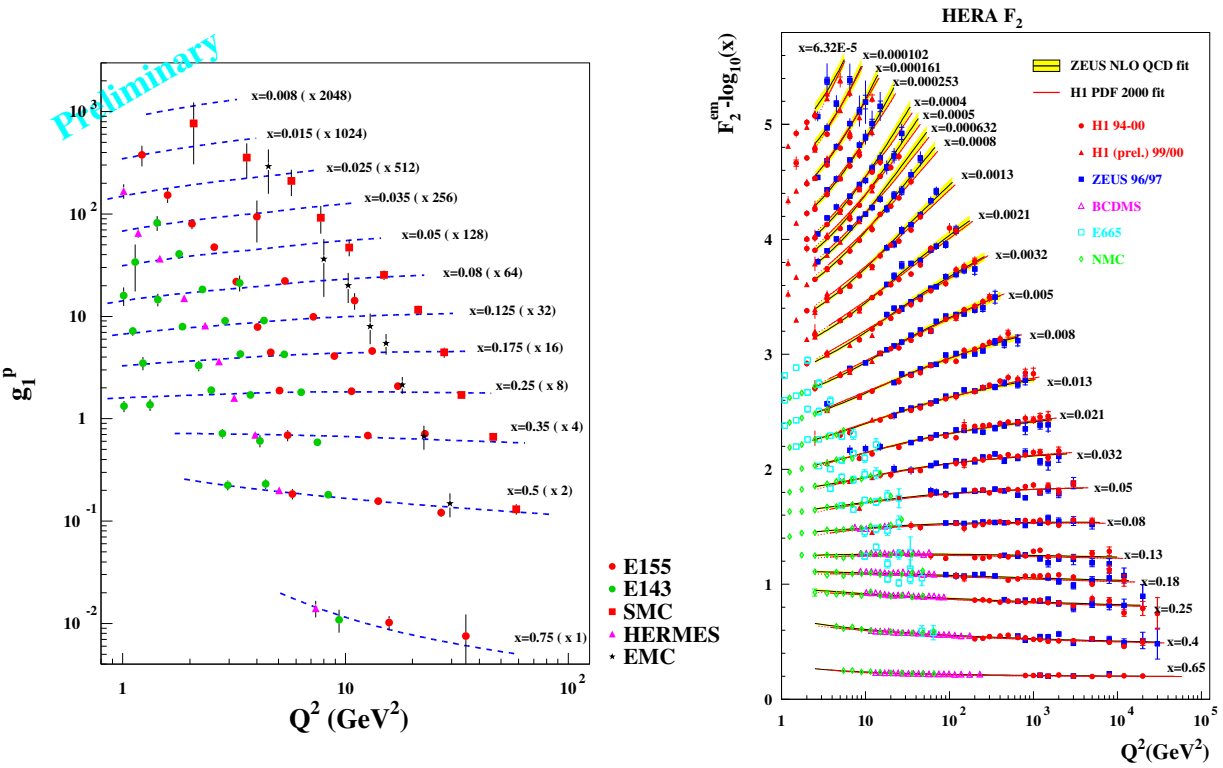

Figure 2.7: Comparison of measurements of g_1 and F_2 structure functions. Figures from [53] (left) and [54] (right).

structure function F_1:

$$g_1(x) = \frac{1}{2}\sum_i e_i^2(q_i^+(x) - q_i^-(x)) \equiv \frac{1}{2}\sum_q e_q^2\,\Delta q(x) \tag{2.32}$$

Roughly speaking the g_1 measures electric charge weighted difference between quarks with spins parallel and anti-parallel to the nucleon spin. Therefore the $g_1(x)$ or rather the $\Gamma_1 = \int_0^1 g_1(x)dx$ contains information about quark contribution to the nucleon spin. A special attention should be given to low x measurements of g_1^d for $Q^2 > 1$ GeV^2. In the SMC [55] in the measured range $\int_{0.003}^{0.7} g_1^d(x)dx = 0.036 \pm 0.005$, whereas a contribution from an unmeasured range was estimated to $\int_{0.0}^{0.003} g_1^d(x)dx = -0.015^{+0.010}_{-0.023}$; (observe the large error). Extrapolation of g_1^d to $x = 1$, was not critical, the SMC value was $0.000^{+0.000}_{-0.001}$. Due to COMPASS measurements [56] the uncertainty of the extrapolation to unmeasured low x region will decrease significantly [57].

QPM prediction for g_1^d can be in a natural way improved using the QCD formalism cf. [58], [59]. In a leading order of the DGLAP evolution the gluon distribution does not enter the g_1^d definition, therefore g_1^d is defined only by quark distributions. The situation changes if next-to-leading order corrections are applied. However, it is worth to consider the following combinations: $g_1^S = g_1^p + g_1^n \approx 1/2 g_1^d$ and $g_1^{NS} = g_1^p - g_1^n$, which are called flavour singlet and non–singlet, respectively. In case of g_1^{NS} the gluon distribution is cancells out at any order of the evolution.

Contrary to F_2, the g_2 structure function does not have an interpretation in the QPM.

In the QPM by definition $g_2 = 0$.

2.2.5 g_1 in the low x region

Measurements of g_1^d for $Q^2 > 1$ GeV^2 and small x do not exist. There was a hope that this region would be explored by the "Polarized HERA", but the project was cancelled. Another accelerator at which this region maybe probed is eRHIC [60].

The behaviour of g_1 in the low x region can be predicted within the QCD. Polarized parton densities, Δp, may be expressed as:

$$\Delta p(x, Q^2) \sim \sum_n \left[\alpha_s \ln\left(\frac{Q^2}{Q_0^2}\right) \ln\left(\frac{1}{x}\right) \right]^n \tag{2.33}$$

and g_1 becomes then [61],[62]

$$g_1(x) \sim \exp \sqrt{\ln\left(\frac{1}{x}\right)} \tag{2.34}$$

However, it was found [63], that including the $\ln(1/x)$ terms is not sufficient in the low x region. In fact g_1 there is governed by the so called double logarithmic corrections: $\ln^2(1/x)$. Including them [64], [65] one obtains:

$$g_1^S(x \to 0) \sim x^{-0.8} \qquad g_1^{NS}(x \to 0) \sim x^{-0.4} \tag{2.35}$$

2.2.6 Regge model prediction

The structure function g_1 at low x and low Q^2 may be described by the models based on the Regge concept. These models give a description of g_1 at fixed Q^2, $Q^2 \ll W^2$.

$$g_1^{S,NS}(x, Q^2) \sim \beta(Q^2) x^{-\alpha_{S,NS}(0)} \tag{2.36}$$

Intercepts $\alpha_{S,NS}(0)$ correspond to the the exchanged Regge poles; in the case of $g_1^{S,NS}$ these are f_1 and a_1 mesons, respectively. It is expected [66], [67] that

$$\alpha_S(0) \approx \alpha_{NS}(0) \leq 0 \tag{2.37}$$

A test of the Regge model of g_1 is performed in this thesis. Other predictions of the low x behaviour of g_1 based on the Regge concept, give:

- $g_1(x \to 0) \sim \ln x$ [68],
- $g_1(x \to 0) \sim 2 \ln\left(\frac{1}{x}\right) - 1$ [69],
- $g_1(x \to 0) \sim \frac{1}{x \ln^2 x}$ [68], disproved, cf. [62]

2.2.7 g_1 in the low x and low Q^2 region

The low x and low Q^2 region of the phase space is of particular interest for this analysis since most of the data measured by COMPASS belong to this region. As it was pointed out in sections 2.2.2 and 2.2.3 two phenomena are expected to be important at low x and

low Q^2: non–perturbative effects and multi-parton interactions. The g_1 behaviour in this region may thus be described by two-component models [70], [71], *i.e.* :

$$g_1(x,Q^2) = g_1^{part}(x,Q^2) + g_1^{VMD}(x,Q^2) \tag{2.38}$$

The partonic part, g_1^{part}, is basically the QCD improved parton model, suitably extrapolated to low Q^2; its low x behavior is controlled by $\ln^2\left(\frac{1}{x}\right)$. The second part, $g_1^{VMD}(x,Q^2)$, is described by (G)VMD–type model. The magnitude of VMD contribution can either be extracted from the data or can be constrained by the Drell-Hearn-Gerasimov-Hosoda-Yamamoto (DHGHY) sum rule [72], [73], [74].

The model [70] was confronted with the SMC [11], [19] and the E143 [75] A_1^p data. The SMC measurement had too large errors and the comparison was inconclusive. The E143 data preferred small negative value of C, the contribution the VMD. The results are shown in figure 2.8, which comes from [70].

In the approach of [71], the DHGHY sum rule was employed. In the photoproduction limit the DHGHY sum rule relates the first moment of g_1 with the anomalous magnetic moment of the nucleon, which is measured. It was found that $C \in (-0.24, -0.30)$, which together with the previous result point towards a negative contribution of the VMD-mechanism to g_1.

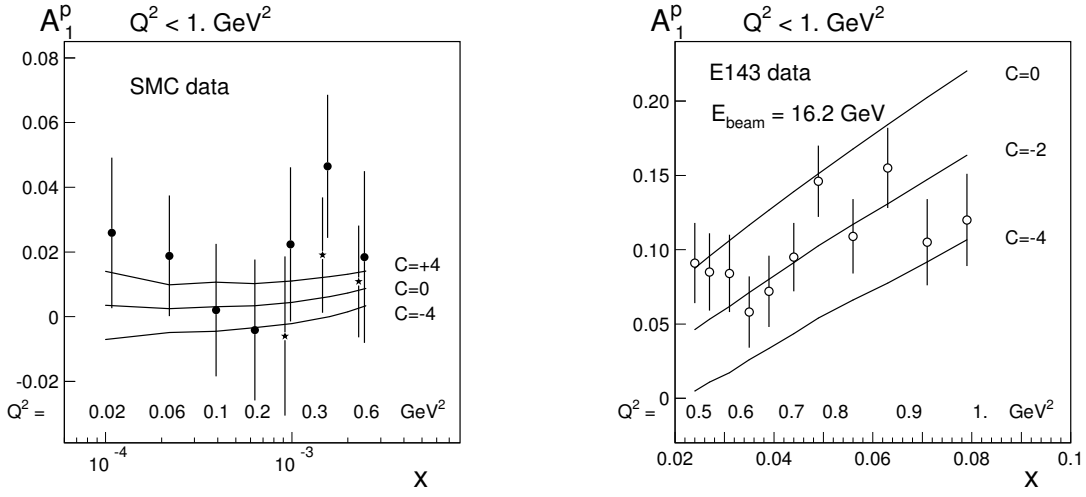

Figure 2.8: Comparison of the model [70] to the data measured by SMC [11], [19] and E143 [75]. The figure is from [70].

2.2.8 Summary

Structure functions describe the internal structure of the nucleons and are universal. Therefore it is very important to know them in the whole phase space. The unpolarized structure functions F_1 and F_2 are measured quite precisely in a wide range of x and Q^2 contrary to the polarized structure functions g_1 and g_2. In the case of g_1 the measurement at large Q^2 and low x are crucial to test sum rules. In this thesis the results for g_1^d at low x and low Q^2 are presented. Although the obtained results cannot be used for the QCD analysis they contribute to understand the nucleon structure in the non–perturbative region.

Chapter 3

Experimental Setup

COMPASS is a fixed target experiment, fourth in line of the muonproduction experiments at CERN at which the (spin) structure of the nucleon is studied. In COMPASS the polarized muon beam interacts with the polarized ^{6}LiD target. In this chapter information concerning the beam, target and the COMPASS spectrometer are presented. Also an overview of the trigger system and of the data analysis chain is given.

3.1 The muon beam

Muon accelerators have not been built yet. Instead secondary muons beams are used. At CERN the proton beam is accelerated in the Super Proton Synchrotron (SPS) up to the energy of 450 GeV. After 12 s acceleration a beam of 2.5×10^{13} protons is extracted during 4.8 s and hits the external beryllium target. In these interactions secondary pions and kaons are produced. Momentum selected pions and kaons are then transported through a 500 m long decay channel. For pions selected by COMPASS the average momentum is 180 GeV. About 7% of the pions decay into muons. To select the latter at the end of the decay tunnel there is a hadron absorber. COMPASS selects positive muons at 160 GeV with roughly 5% momentum spread. The beam momentum is measured in a set of hodoscopes called the Beam Momentum Station (BMS). The measured precision is about $\delta p/p \approx 0.5\%$. After the BMS the muon beam is focused on the COMPASS polarized target where the beam spot has the RMS width of about 0.8×0.8 cm^2. The beam contains on average 2×10^8 muons per SPS spill.

The $\pi \to \mu\nu$ decay channel is a parity violating one; as a result the muons are naturally polarized along their momentum. The 100% muon polarization is obtained in the decaying pion rest frame. In the laboratory frame muon polarization is a function of the ratio of the pion (E_π) and the muon (E_μ) energy and is given by the formula:

$$P_{\mu^\pm} \approx \pm \frac{m_\pi^2 + (1 - 2\frac{E_\pi}{E_\mu})m_\mu^2}{m_\pi^2 - m_\mu^2} \tag{3.1}$$

The sign of polarization depends of muon charge. Beam polarization was not measured by COMPASS; instead a value of -0.76 ± 0.03, expected from the SMC measurements [76] was employed.

3.2 The polarized target

The COMPASS target is composed of two cylindrical cells, 60 cm long and 3 cm in the diameter. The cells are separated by a 10 cm long gap. Both cells are filled with a lithium deuteride (^{6}LiD). The ^{6}Li nucleus can be considered to large extent as He+D system, see [77]. Therefore the ^{6}LiD might be described as two polarizable (spin 1) deuterons and an unpolarized (spin 0) helium core. The total amount of the polarizable material is approximately 50 % (4 out of 8 nucleons).

Apart from ^{6}LiD there are other materials and impurities in the target, mainly ^{4}He and ^{3}He, ^{7}Li, ^{1}H, ^{2}D, ^{64}Cu, ^{59}Ni (the last two come from the polarization measurement system). Target composition is summarized in table 3.1.

element	number of moles
^{1}H	0.102
^{2}D	44.537
^{3}He	3.621
^{4}He	10.912
^{6}Li	42.843
^{7}Li	1.795
^{12}C	0.008
^{19}F	0.016
^{59}Ni	0.0057
^{64}Cu	0.0136

Table 3.1: COMPASS target composition for 2002 [78].

The target is placed in the magnetic field created by a super-conducting magnet system taken from the SMC, [79]. The system consists of a solenoid providing 2.5 T field and a dipole magnet providing the field of 0.5 T, the direction of which can be changed. The dipole is used to reverse the target polarization and during the transverse polarization data taking. The reversal of the polarization is done almost every 8 hours in order to decrease some of the systematic errors, cf. section 5.5.1.

Nucleons cannot be significantly polarized using the standard method based on the Zeemann effect. Their magnetic moments are too small. In a low temperature (0.5 K) and a strong magnetic field (2.5 T) expected nuclear polarizations are: 0.005 and 0.001 for proton and deuteron respectively, which can be compared with an electron polarization of 0.998. To achieve a high level of a nuclear polarization a technique called the Dynamic Nuclear Polarization (DNP) [80] is used. The principle of the method is the following[1].

Polarized material is kept at a low temperature and in a strong magnetic field. Conditions are chosen in such a way that a very high electron polarization is achieved. The target is then exposed to the microwave radiation of energy needed to flip simultaneously both the proton and the electron spins. This energy depends on the value of the total spin of the e-p system (0 or 1). For a chosen microwave radiation energy only one spin state, 0 or 1, is flipped. The electron relaxates to the lower energy state within milliseconds while

[1]For simplicity only the electron-proton state (e-p) is considered.

the proton, due to its small magnetic moment, has a small probability to change its spin orientation. Moreover the double spin-flip transition is forbidden. This leads to a build-up of a proton polarization. The idea of DNP is presented in figure 3.1.

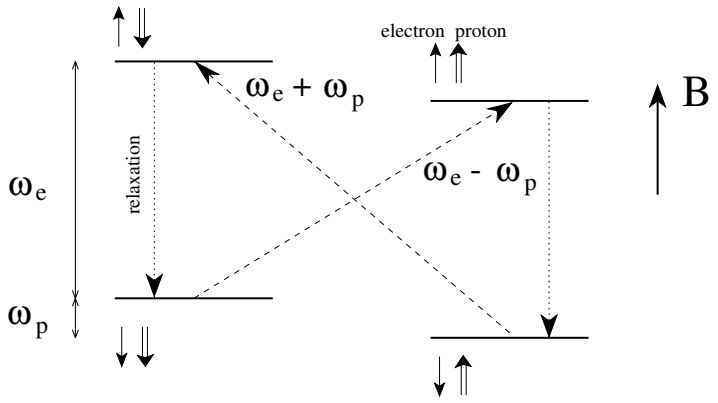

Figure 3.1: Energy levels for an e-p state in a strong magnetic field, B. Arrows indicate directions of the proton $\Uparrow$ and electron $\uparrow$ spins; ω_e and ω_p are Lamor frequencies of the electron and the proton, respectively. Figure comes from [81].

In COMPASS the build-up of the polarization using DNP takes several days. After the polarization has achieved a reasonable level ($\sim$50%) the microwaves are switched off and the temperature is lowered to about 50 mK. In this mode, the so called "frozen spin", the deuteron polarization can be maintained for about 1000 hours. The cells of the COMPASS target are polarized in opposite directions. Simultaneous data taking with such cells allows to decrease the systematic error of the asymmetry measurement.

3.3 The spectrometer

The COMPASS spectrometer is schematically shown in figure 3.2. It consists of two main parts: Large Angle Spectrometer (LAS) and Small Angle Spectrometer (SAS). The LAS (SAS) is used to measure low (high) momentum particles emitted at large (small) angles with respect to the beam axis. LAS is a part of the COMPASS detector which does not have an equivalent in the SMC. Each of the spectrometers contains a magnet: SM1 in LAS and SM2 in SAS. Their magnetic field strength $\int Bdl$ is 1 Tm and 4.4 Tm, respectively.

In the region before the target there are two stations of Scintillating Fibers (FI), [82], and three stations of Silicon detectors (SI), [83]. Positions and angles of the incoming muon tracks are measured in these detectors. The beam momentum is measured in the BMS, cf. section 3.1.

Downstream the polarized target, the second part of the COMPASS detector starts, the LAS. The detectors installed in this part of the spectrometer usually have a good resolution of 100-200 μm, which is needed to achieve a good spatial resolution of tracks and a good precision of the vertex reconstruction as COMPASS does not have a dedicated vertex detector. Detectors of different types are installed in the LAS area. The variety of types is caused by two factors: costs and allowed maximal particle flux. Closest to the beam axis there are the FI detectors. Further from the centre there are the Micromega (MM) detectors, [84], the drift chambers (DC), [85], the Gaseous Electron Multiplier (GEM or GM), [86], the Straw detectors (ST), [87], and the Multi-Wire Proportional Chambers (MWPC),

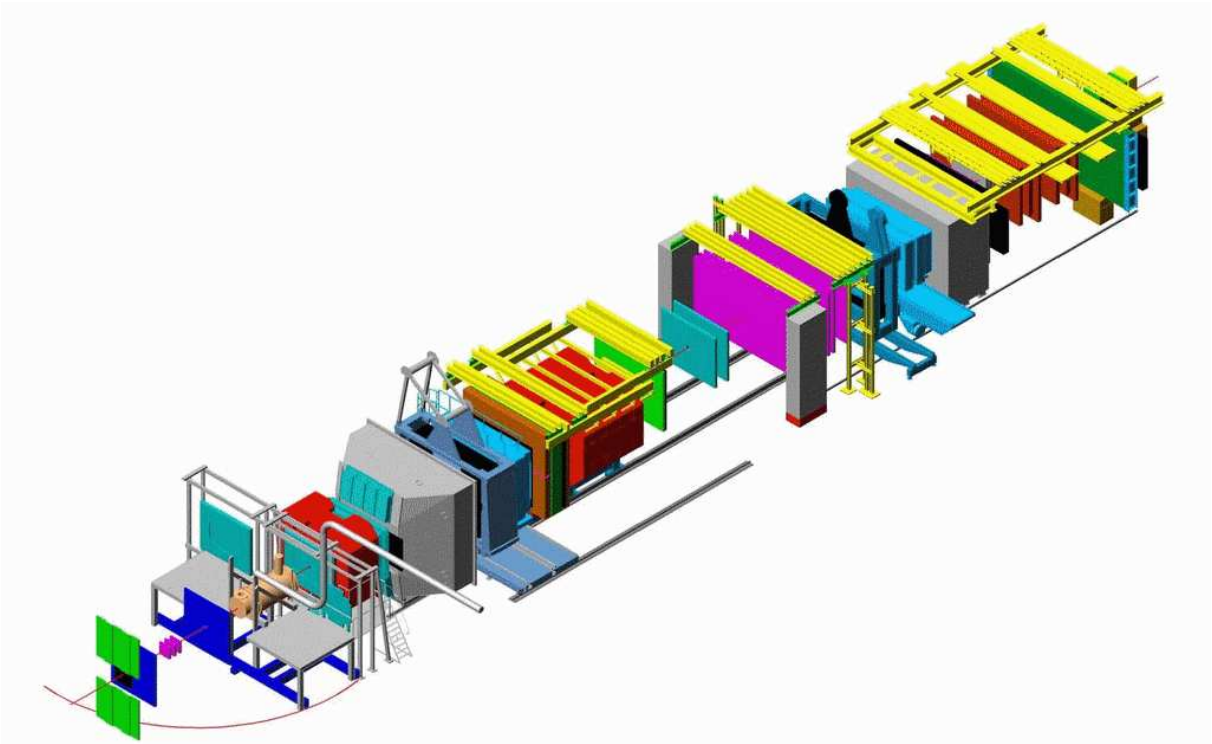

Figure 3.2: Sketch of the COMPASS spectrometer.

[88]. Some of these detectors are based on new concepts, planned for the future LHC experiments. COMPASS plays an important role in testing those new types of equipment. Most of the detectors have a hole in the centre. In case of the GM and the DC this hole can be switched on or off depending on the beam intensity.

In the LAS there is a Cherenkov detector (RICH), [89], for particle identification, *i.e.* a separation between pions, kaons and protons. Muons and electrons are also detected, but *e.g.* muons and pions cannot be distinguished due to similar masses[2]. Pions, kaons and protons with momentum greater than 2, 8, 18 GeV, respectively, can be identified. Information from the RICH is not used in this analysis.

Finally at the end of the LAS there is the first hadron calorimeter, HCAL1, and a muon filter made of iron. The only particles which can pass through it are muons. To measure them there is a group of detectors called Muon Wall A (MWA) around the filter. HCAL1 and the muon filter have a 1×1 m^2 hole in the central part. This allows hadrons and muons which are passing near the beam axis to be measured in the second spectrometer.

In the second spectrometer there is no need to put many precise detectors, because the large distance from the target creates good angular separation. There are MWPC, ST and DW [90] detectors, In addition a few GM and FI are also mounted there. Finally there is an electron calorimeter (ECAL2), a hadron calorimeter (HCAL2), a hadron absorber and a Muon Wall B (MWB). The second spectrometer ends almost 50 m away from the target centre. More details about COMPASS spectrometer can be found in table 3.2.

The RICH detector cannot distinguish between muons and pions. The separation can be done if those particles pass through the hadron absorbers. Additional information comes from HCAL1 and HCAL2. A pion deposits almost its whole energy in the calorimeters, whereas a muon is a minimum ionizing particle and the deposit left in the calorimeters is

[2]The separation between them will be discussed later.

small, about a few GeV.

There are also dedicated detectors (hodoscopes) which search for the scattered muons. More detailed discussion of these detectors and the COMPASS trigger system is presented in the next section.

3.4 Triggering system

The COMPASS electronic system may record about 40k events per spill. In every spill about 2×10^8 muons from the beam and from the halo cross the spectrometer. Most of these do not interact in the target. Dedicated electronic systems were built in order to select events for which an interaction in the target has occurred.

Interacting muons loss their energy and are scattered at a non-zero angle. To search for these muons at least two detectors, a few meters away from each other, are needed. It is faciliated by the so called *coincidence matrix*, which tells whether the observed signal position in the two hodoscopes might come from a scattered muon (positive coincidence) or rather from the beam halo (negative coincidence).

Veto detectors, which are installed before the target, have a hole in the middle. Muons which cross the target do not create any signal, but muons which are away from the beam axis do. A signature of scattered muon is therefore a positive signal from the coincidence matrix and no signal from the veto counters.

Due to its rich physics programme, the COMPASS spectrometer records processes which cover large kinematic range of variables *i.e.* $Q^2 \in (10^{-3} - 10^2)$ GeV^2, $x \in (10^{-5} - 1)$. Different sets of hodoscopes are needed to select different classes of events. COMPASS has 4 different sets of hodoscopes called: inner, ladder, middle and outer. The inner hodoscopes are the smallest, *e.g.* 0.18 m $\times$ 0.32 m as compared to the outer hodoscope of 4.8m $\times$ 2.2 m. Most of the events from the low x and low Q^2 domain are measured in the inner hodoscopes.

For the inner, ladder and partially middle hodoscopes there were still too many events fulfilling the demanded criteria. Additional reduction comes from calorimeters. A 6 GeV energy deposit in calorimeters was required to reduce: radiative events, μe scattering events and low energy halo tracks. This additional criterium lowers the number of selected events to a level at which they may be recorded. Since 2003, there is also a pure calorimetric trigger: an event is recorded if large enough energy deposit (8-18 GeV) calorimetric trigger in calorimeters was found [3].

To summarize, the trigger criteria are as follows:

- a positive signal from coincidence matrix,
- no signal in veto counters,
- large enough energy deposit in HCAL1 and HCAL2[4].

If the above criteria are met an event is recorded. Typical trigger rates per spill are given in table 3.3. In most cases the trigger name comes from a corresponding hodoscope set.

[3] The threshold for the calorimetric trigger has changed every year.

[4] For certain triggers the calorimeter information is not taken into account.

Detector name	no. of planes	position (m)	size (m^2)	resolution (μm)
FI01	2	-7.60	0.04×0.04	120
SI01	4	-4.90	0.07×0.05	10
SI02	4	-4.30	0.07×0.05	10
SI03	4	-3.60	0.07×0.05	10
FI02	3	-2.85	0.04×0.04	120
target	-	-0.35		
FI03	3	1.20	0.05×0.05	120
MM01	4	1.45	0.4×0.4	110
MM02	4	1.95	0.4×0.4	110
FI04	3	2.15	0.05×0.05	120
MM03	4	2.45	0.4×0.4	110
DC01	8	2.65	1.8×1.3	250
SM1	-	283-443	-	-
DC02	8	4.65	1.4×1.2	300
GM01	4	4.80	0.32×0.32	110
DC03	8	5.05	1.8×1.3	300
GM02	4	5.20	0.32×0.32	110
ST03	12	5.45	3.2×2.7	400
GM03	4	5.60	0.32×0.32	110
FI05	2	5.85	0.08×0.08	150
RICH	-	590-940	-	-
PS01	4	9.50	1.8×1.2	600
GM04	4	9.60	0.32×0.32	110
ST04	6	10.15	3.2×2.7	400
PA01	3	13.74	1.8×1.2	600
GM05	4	13.84	0.32×0.32	110
MA01	8	14.15	4.8×4.1	2900
FI06	3	15.00	0.1×0.1	200
MA02	8	15.30	4.8×4.1	2900
PA02	3	15.70	1.8×1.2	600
GM06	4	15.80	0.32×0.32	110
SM2	-	1600-2000	-	-
PA03	3	20.15	1.8×1.2	600
GM07	4	20.20	0.32×0.32	110
PA04	3	20.45	1.8×1.2	600
GM08	4	20.50	0.32×0.32	110
PA05	3	20.75	1.8×1.2	600
GM09	4	20.80	0.32×0.32	110
FI07	2	21.30	0.1×0.1	200
ST05	6	24.55	3.2×2.7	400
ST06	6	25.85	3.2×2.7	400
DW03	4	28.65	5.2×2.6	1500
DW04	4	30.10	5.2×2.6	1500
DW05	4	30.40	5.2×2.6	1500
PA11	3	30.70	1.8×1.2	600
PA06	3	31.00	1.8×1.2	600
GM10	4	31.05	0.32×0.32	110
DW06	4	31.30	5.2×2.6	1500
FI08	2	32.00	0.12×0.12	200
PB12	3	41.90	1.6×1.8	600
MB01	6	42.85	4.7×2.2	1400
PB34	3	44.00	1.6×1.8	600
MB02	6	44.90	4.7×2.2	1400
PB56	3	46.20	1.6×1.8	600

Table 3.2: Detectors in the COMPASS spectrometer during 2003.

Triggers for which the energy deposit in the hadron calorimeters is required are called $semi - inclusive$; triggers for which only scattered muon is required are called *inclusive*.

There are also other trigger types like: *i*) veto triggers (if a signal is detected in the veto detectors), *ii*) beam trigger (if a signal is detected in SI and FI), *iii*) random trigger (the data acquisition system fires randomly). Usually for these triggers there is only one particle which crosses the spectrometer. Reconstruction of such cases is very simple. This allows a good detector calibration, efficiency study and the alignment of the spectrometer. The latter is discussed in detail in section 4.

trigger name	rate/spill
inner trigger	12000
ladder trigger	6500
middle trigger	1500
outer trigger	10000
inclusive middle trigger	5000
calorimetric trigger	6500
total	41000

Table 3.3: Typical trigger rates in COMPASS in 2003.

3.5 Data analysis chain

Raw events are later processed by a reconstruction program CORAL. The reconstructed data are stored in the so called "mini Data Summary Tree", mDST, format. The PHysics Analysis Software Tools, PHAST, is the framework for data analysis in COMPASS at the level of the mDST. It provides an access to events and information concerning reconstructed events and an environment for development of physics analysis codes. Further analysis is performed in the ROOT framework. Apart from these COMPASS uses a few Monte-Carlo (MC) programs. The physics interactions are simulated in a few generators *i.e.* LEPTO [91], AROMA [92] and PYTHIA [93]. Generated events are later put through COMGEANT, a program based on [94], which simulates the COMPASS spectrometer. In further steps events are reconstructed by CORAL and then read by PHAST. In this analysis the Monte Carlo information was of a very limited use.

Chapter 4

Alignment of the COMPASS spectrometer

A good alignment of the spectrometer is crucial for the correct event reconstruction. Position of the detectors after installation in the experimental area is known with a rough precision of 1-2 mm but most of the detectors in the COMPASS spectrometer have a resolution much better than that, cf. table 3.2. Inaccurate alignment results in detectors hits not correlated with tracks, giving rise to reconstruction inefficiencies. Moreover many tracks may not even be found, because there would not be enough hits which could be correlated with them.

The author was responsible for the alignment of the COMPASS spectrometer for almost two years. Alignment is a difficult task. There are many detectors planes, more than 300; for each plane a set of parameters should be optimized. Many detector types have different sizes (from 4×4 cm^2 up to 4.8×2.2 m^2) and resolutions (from 10 μm up to 10 cm). To make the situation even more complex the alignment in the presence of the magnetic field had to be performed as well. For a detailed description of the COMPASS alignment program and procedure see [95].

4.1 Alignment parameters

There are many types of the detector parameters which can be optimized. Among them there are three which are mostly crucial:

- a transverse detector offset perpendicular to the wires, δu,
- a rotational detector offset in a plane perpendicular to the beam axis, $\delta\theta$,
- a longitudinal detector offset along the beam line, δz.

The transverse offset of the detector plane along the wires, δv, cannot be directly corrected for since planes give no information about positions along this direction. However, if a detector contains *e.g.* two planes with a non-zero angle between them then after combining the alignment results the δv can be corrected for.

Other alignment parameters which can be optimized are the rotational offsets with respect to the planes which are not perpendicular to the beam axis ($\delta\theta_u$, $\delta\theta_v$). Such

deviations exist *e.g.* for ST and MM. They are much less important than δu, $\delta\theta$ and δz and therefore were not corrected for.

A *pitch* of a detector is a distance between two adjoining strips, pads or wires. There is a possibility that a real detector has a pitch slightly different than the designed one. To correct the pitch an additional parameter was introduced, $\delta pitch$. A value $(1+\ \delta pitch)$ is used as a multiplicative factor of the pitch. It can also partially correct the $\delta\theta_u$ misalignment. The pitch correction parameter is usually strongly correlated with the longitudinal detector offset, δz. In fact if all the tracks were of the same origin then the correlation would be strict: $\delta p = \delta z/z$. Even if the tracks are not of the same origin, the $\delta pitch$ parameter might be used to partially correct the 'z' misalignment.

4.2 Alignment program

Charged particles which travel through the spectrometer leave hits in the detectors. From those hits tracks are reconstructed. The difference, ΔS, between the hit position measured in the detector and expected from the track model may be approximated by a linear function of two independent sets of parameters:

- track parameters, α_t (*e.g.* in the simplest case when magnetic fields are off, tracks are approximated by straight lines)
- alignment parameters, α_a

The idea of the alignment method used in the experiment is to find such values of the alignment parameters for which the following χ^2 is minimal:

$$\chi^2 = \sum_{i=1}^{n_{track}} \sum_{j=1}^{n_{det}} \frac{[\Delta S(u_{ij}, \alpha_{it}, \alpha_a)]^2}{\sigma_j^2} \tag{4.1}$$

where u_{ij} is a hit position of the 'i' track in the 'j' detector and σ_j is a resolution of the 'j' detector.

The χ^2 minimalization, equation (4.1), can be done analytically by requesting that the partial derivatives of χ^2 over all alignment and track parameters are zero. This statement, after some algebra, leads to a matrix equation in a form:

$$\left(\begin{array}{c|c|c|c} \sum C_i & \dots & G_i & \dots \\ \hline \vdots & \ddots & 0 & 0 \\ \hline G_i^T & 0 & \Gamma_i & 0 \\ \hline \vdots & 0 & 0 & \ddots \end{array}\right) \left(\begin{array}{c} \alpha_a \\ \hline \vdots \\ \hline \alpha_{it} \\ \hline \vdots \end{array}\right) = \left(\begin{array}{c} \sum b_i \\ \hline \vdots \\ \hline \beta_i \\ \hline \vdots \end{array}\right) \tag{4.2}$$

where $\sum C_i$ and $\sum b_i$ include only derivatives of ΔS_j over the alignment parameters, Γ_i and β_i include only derivatives of ΔS_j over track parameters and G_i and G_i^T contain mixed terms of type $(\partial\Delta S_j/\partial\alpha_a)(\partial\Delta S_j/\partial\alpha_{it})$. A solution of this matrix equation *i.e.* a set of α_{it} and α_a parameters is a product of the inverse matrix and the right hand side vector. The time needed for a matrix inversion is proportional to n^3, where n is its size. Inversion of a symmetric 5000×5000 matrix requires a few CPU 2.6 GHz hours. This size of the matrix is easily achieved using 1000 tracks (4 parameters in each track) and about 1000 alignment parameters which are used in COMPASS (300-350 planes with 3 alignment parameters

each). Fortunately, the matrix in equation (4.2) has a special structure and an algebraic trick may be used. It was shown [96] that the alignment parameters are obtained from $\alpha_a = (C')^{-1}b'$ where:

$$\begin{aligned} C' &= \textstyle\sum_i C_i - \sum_i G_i \Gamma_i^{-1} G_i^T \\ b' &= \textstyle\sum_i b_i - \sum_i G_i \Gamma_i^{-1} \beta_i \end{aligned} \tag{4.3}$$

Thus only the matrix C' and matrices Γ_i have to be inverted. The core of the alignment computer program (matrix inversion) is a routine called "Millepede" which was written by Volker Blobel, the co–author of [96].

4.3 ΔS function and derivatives

The expression for ΔS depends on the assumed track model and on the alignment parameters which one wants to tune. During the alignment runs magnetic fields of SM1 and SM2 are off and therefore the tracks may be approximated by straight lines:

$$\begin{aligned} x_j &= x_0 + \tfrac{dz}{dx}(z_j - z_0) - x_j^c \\ y_j &= y_0 + \tfrac{dz}{dy}(z_j - z_0) - y_j^c \end{aligned} \tag{4.4}$$

here x_j, y_j and z_j, are the track positions in the 'j' detector, x_0, y_0, z_0 are track coordinates in the reference plane, usually chosen the plane closest to the target which contains a hit associated with the track and finally x_j^c, y_j^c, are positions of the 'j' detector centre.

Taking into account the alignment parameters: δu, $\delta\theta$, δz and $\delta pitch$, ΔS becomes:

$$\Delta S = (1 + \delta pitch)\left[\cos(\theta + \delta\theta)[x_0 + \frac{dz}{dx}(z_j - z_0)] + \sin(\theta + \delta\theta)[y_0 + \frac{dz}{dy}(z_j - z_0)] - \delta u\right] \tag{4.5}$$

where θ is the angle between the u and x axes.
After linearization the partial derivatives over the track parameters become:

$$\begin{aligned} \tfrac{\partial \Delta S}{\partial x_0} &= \cos\theta \\ \tfrac{\partial \Delta S}{\partial y_0} &= \sin\theta \\ \tfrac{\partial \Delta S}{\partial \frac{dz}{dx}} &= \cos\theta(z_j - z_0) \\ \tfrac{\partial \Delta S}{\partial \frac{dy}{dx}} &= \sin\theta(z_j - z_0) \end{aligned} \tag{4.6}$$

After linearization the partial derivatives over the alignment parameters become:

$$\begin{aligned} \tfrac{\partial \Delta S}{\partial \delta u} &= -1 \\ \tfrac{\partial \Delta S}{\partial \delta\theta} &= -x_j \sin\theta + y_j \cos\theta \\ \tfrac{\partial \Delta S}{\partial \delta z} &= \tfrac{dz}{dx}\cos\theta + \tfrac{dz}{dy}\sin\theta \\ \tfrac{\partial \Delta S}{\partial \delta pitch} &= x_j \cos\theta + y_j \sin\theta \end{aligned} \tag{4.7}$$

4.4 The alignment procedure

There are special runs taken by COMPASS for the alignment purposes. During these runs the SM1 and SM2 magnetic fields are off, so tracks of charged particles can be approximated as a straight lines[1]. The alignment runs are taken with a low intensity of the beam: about 10^6 muons/spill. Special types of triggers are used for these runs (cf. section 3.4).

To make the reconstruction possible an initial description of the COMPASS spectrometer is needed. It is contained in the so called *detector.dat* file. This file contains estimated values of the parameters of the detectors (*e.g.* their x, y, z positions, θ angle, pitch value *etc.*). Position of a detector is usually taken from the surveyors measurements. Those measurements have a precision of about 0.3 mm. However, this precision is lost after subsequent transformation of coordinates system. Instead of 0.3 mm, detectors position is known with a precision of 1-2 mm. Usually as the θ angle a nominal rotation angle of the detector is taken, also the pitch value is usually set to a nominal value.

At the beginning of the alignment procedure events are reconstructed by the CORAL. For the reconstruction the initial *detector.dat* is used. At this stage of the alignment procedure tracks from about 20k events are reconstructed. As an output a ROOT tree with information about reconstructed tracks, hits and clusters is obtained. These information items form an input for the Millepede. The next stage of the procedure is the χ^2 minimalization by the alignment program resulting in corrections to the alignment parameters. During minimalization some of the parameters have to be fixed because a shift or a rotation of the whole spectrometer does not change the χ^2 value. Usually the alignment parameters of GM04 and GM10(9) are fixed. The last step of the alignment is an update of the *detector.dat* file by the results obtained from the Millepede.

To summarize, the alignment procedure is performed in three steps:

- creating a ROOT tree, with track, hit and cluster parameters in the reconstruction performed by CORAL[2],
- χ^2 minimalization using Millepede,
- updating of the reference *detector.dat*.

Solution given by the Millepede is an exact one. However, usually a few iterations of the above procedure are needed since: *i*) the Millepede solves a linear equation system but in fact a dependence of the alignment on the track parameters might be non-linear, *ii*) initial miss-alignment is large which might introduce a bias in the reconstruction, *iii*) a track model which is used in the Millepede is too simple. Usually two or three iterations are needed. Their exact number depends upon the size of the correction compared to the detector resolution.

4.5 Quality criteria

After the alignment procedure checks have to be done to investigate the quality of it. The quality criteria may be divided into two groups: the absolute and the relative criteria.

[1] There exist certain residual fields in SM1 and SM2 but the straight line fit approximately holds.
[2] Which works with a reference *detector.dat*.

4.5.1 Absolute criteria

The absolute criteria are these for which the expected value is known as *e.g.* the mean value of χ^2/ndf of the tracks or masses of particles like K^0, D^0, J/Ψ. The χ^2 and masses give a global estimate of the alignment quality. This quality may also be defined for each detector plane separately. A criterium describing the quality value might be a mean value of the residuum in a particular plane, Δu, where $\Delta u = u_{cluster} - u_{track}$ is a difference between the position of a hit cluster and of a reconstructed track. The Δu is in fact a *biased* residuum because the detector in which Δu is computed is not switched off during the tracking procedure. Three distributions are important:

- Δu
- Δu as a function of u
- Δu as a function of v

where u and v, are the positions of a hit in a detector in the direction perpendicular to the wires and along the wires, respectively. The mean value of the Δu, $< \Delta u >$, is a biased estimator of the transverse misalignment, δu (cf. section 4.1). A slope $\partial\Delta u/\partial u$ is sensitive to the 'z' misalignment and the pitch variations while a slope $\partial\Delta u/\partial v$ is sensitive to the rotational offset $\delta\theta$. For a properly aligned detector, the values of $< \Delta u >$, $\partial\Delta u/\partial u$ and $\partial\Delta u/\partial v$ are equal to zero.

4.5.2 Relative criteria

All but absolute criteria are called relative criteria. The latter used in COMPASS are global. This means that they give information about the quality of the alignment for the whole spectrometer. Some of them are listed below:

- number of reconstructed tracks (with defined momentum) per event in the spectrometer,
- number of reconstructed vertices per event,
- number of tracks per vertex,
- number of reconstructed events which contain both μ and μ',
- reconstructed widths of particle, *e.g.* K^0, D^0, J/Ψ, mass distributions.

These criteria are checked for the standard COMPASS data taking runs and not in the alignment runs. The number of reconstructed tracks per event in the spectrometer (t.p.e.) only gives a rough estimate of the alignment performance since it is not a monotonic function of the alignment quality. In a perfectly aligned spectrometer the t.p.e. will be lower than in a case of a less precise alignment. This surprising effect can be understood: the COMPASS spectrometer has two magnets. Therefore a single track which crosses both the SM1 and the SM2 in a not perfectly aligned spectrometer might be reconstructed as two tracks, one in the LAS and one in the SAS. This leads to the fact that the t.p.e. increases if the spectrometer alignment is less accurate. A better criterium seems to be the number of tracks which pass through both the SM1 and the SM2 magnets. The most

important estimate of the alignment quality, which can be checked with a relatively small number of reconstructed tracks, is the number of events which contain both a μ and a μ'.

The decay width of a particle, *e.g.* K^0, cannot be checked for a statistics as low as about 20k raw events, which is typically used for the alignment purposes. To get an estimate of the K^0 width with 10% uncertainty one needs at least about 2.5M raw events. Moreover 10% uncertainty is large; within such large error the sensitivity to the alignment quality is very poor. More sensitive are the positions of the mass peaks, which are considered to be absolute criteria. Indeed for the 2002 data a large (2.0 MeV) discrepancy for the K^0 peak position was found. However, this discrepancy was not caused by the alignment of the detectors but by a 0.85% underestimate of the magnetic field strength of the SM2.

4.6 Alignment with magnetic field

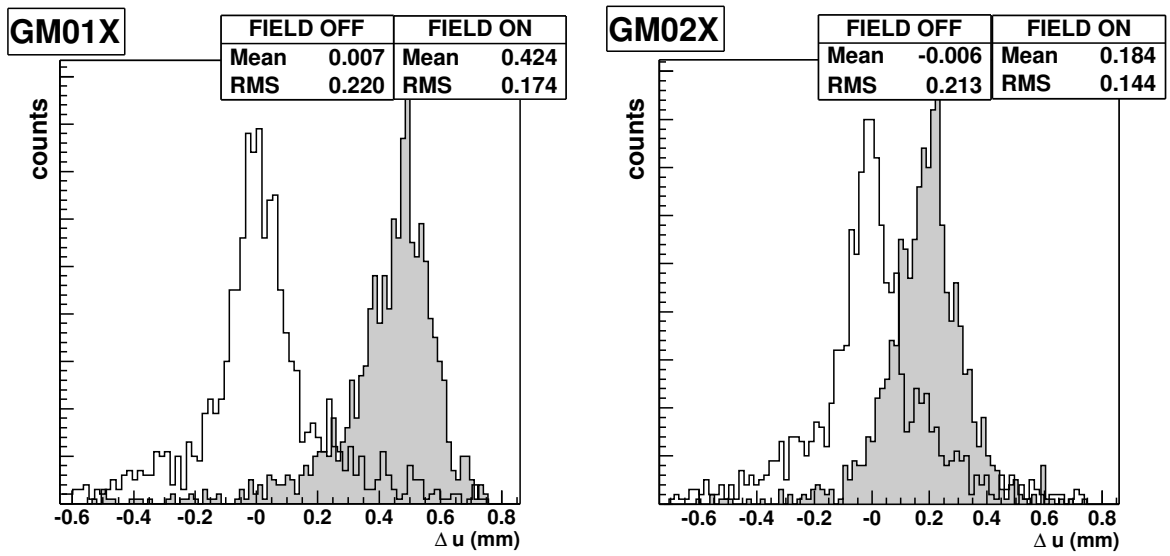

Figure 4.1: Residuals in GM01X and GM02X detectors before (white) and after (grey) the magnetic field was switched on.

The residual distribution, Δu, for GM01X and GM02 detectors after the alignment is shown in figure 4.1 (white background). The mean values of the Δu distributions are close to zero, *i.e.* the detectors are properly aligned. The same Δu distribution was obtained for a "physics" run, which was taken just after the alignment run (grey background in figure 4.1). A large discrepancy is observed between the mean values of the residuals before and after switching on the magnetic field. The effect does not exist for Y-planes of the GM detector. The signal in GM is transferred by electrons. GM01-03 are placed close to the SM1 which has a large fringe field outside the magnet aperture and therefore the Lorentz force $q\vec{v} \times \vec{B}$ acts on the electrons in the GM. Due to that force the electron trajectory is deflected, the so called Lorentz effect. The impact of it on the registered electron position is large. For the GM01-X plane it is about five times larger than the detector resolution. Some of the detectors also have magnetized supports so they can move when the magnetic field is switched on after the alignment run.

Because of the above mentioned effect, alignment with the magnetic field on has to be performed. The other important reason for performing a field-on alignment is that the tracks have completely different four momenta during the physics run than during the alignment run which *e.g.* leads to different sensitivity to the 'z' alignment.

The field-on alignment is much more complicated than the one without the magnetic field. Tracks can no longer be approximated as straight lines and tracks multiplicities are larger. Another problem is that the alignment of the detectors before the target cannot be performed simultaneously with the rest of the spectrometer. During the alignment with the magnetic field tracks are no longer parametrized; instead a linear deviation with respect to the parameter obtained during the data reconstruction is used. It was shown, [95], that in such a situation the derivatives over local and global parameters are not changed[3] compared to the alignment without the magnetic field.

The whole alignment procedure described in section 4.4 is made for a physics run. Typically 20k events are used during the alignment with the magnetic field. Iterations are also made. During the alignment with the magnetic field they are even more needed than in the field-off runs. This is so because tracks have another degree of freedom, their momentum, which is not taken into account in the alignment program.

After the field-on alignment the detectors before the target (FI01, FI02 and SI) are aligned. This alignment cannot be done simultaneously with the rest of the spectrometer. A beam track always ends in the primary vertex (its continuation in the spectrometer is a scattered muon track), therefore there is no information flow between the detectors which are before and after the target. In the alignment of the detectors before the target off-time tracks which have not interacted in the target are employed. They can be extrapolated through the whole spectrometer. The only detectors which are used during the tracks reconstruction are FI and SI. During the χ^2 minimalization the alignment parameters of FI03-FI08 are fixed. Still the alignment of the detectors before the target is a difficult task. Many iterations are needed and there appear difficulties which the alignment program cannot solve, cf. section 4.7.4.

4.7 Results of the alignment

In this section a comparison of results obtained using two different alignment methods is presented. Different phenomena observed during the alignment procedure are discussed.

4.7.1 Comparison of the alignment methods

Results of the comparison between the different alignment methods are presented in table 4.1, [95]. The first method is based on χ^2 minimalization, and was described in section 4.2. The second is a commonly used method based on distributions of residuals. In this method the position of any pair of detectors is fixed and only these two detectors are used during the track reconstruction. After the track reconstruction the residuals distributions for detectors, which have to be aligned, are plotted. Depending on the mean value of the residuals a correction to the positions of the detectors is made. This method was used in COMPASS before the χ^2 minimalization method was implemented.

[3] Observe that there are no track parameters, but linear corrections to them.

method	t.p.e.	χ^2/ndf	PV [%]	tracks in PV	μ/μ' [%]
(1)	3.09	3.07	45.7	3.38	33.1
(2)	1.71	7.98	36.1	2.96	14.2

Table 4.1: Comparison of the tracking performance for different alignment methods. See text for details.

In table 4.1 a PV is a percentage of events for which the primary vertex was reconstructed and μ/μ' is a percentage of the events for with both the beam and the scattered muon were reconstructed. A large difference in the tracking performance for these two alignment methods is observed. For every parameter the χ^2 minimalization method gives much better results than the residual one.

4.7.2 Cross-check of the alignment

In table 4.2 a cross-check of the reconstruction performance for one of the runs is given. Data were reconstructed using different *detector.dat* files, which came from independent alignments: one was done at the end of 2002 and the other in 2003. Different versions of CORAL were used (different reconstructions). The comparison was made separately for semi–inclusive and inclusive triggers. Relative differences in percent between tracking performance for these two alignments are shown. Positive numbers indicate that reconstruction with the 2003 alignment resulted in a larger value of a given variable.

relative number of	semi–inclusive	inclusive
all tracks	-0.13 ± 0.12	0.08 ± 0.15
tracks in SM1	-0.18 ± 0.11	0.16 ± 0.10
tracks in SM2	-0.11 ± 0.14	0.13 ± 0.19
μ' tracks	-0.02 ± 0.09	0.34 ± 0.26
beam tracks	0.13 ± 0.10	0.06 ± 0.20
PV	0.35 ± 0.23	0.7 ± 1.3
tracks in PV	0.10 ± 0.10	0.13 ± 0.15
μ/μ' events	0.97 ± 0.28	-0.2 ± 1.0

Table 4.2: Tracking performance for two independent alignments. A relative change of parameters in percent is shown.

The results of both alignments are in a very good agreement. The later alignment might give more μ/μ' events, however the difference most probably comes from the fact that CORAL was improved between the alignments.

4.7.3 Target polarization reversal and the FI movement

The target polarization is reversed usually every eight hours. After the polarization reversal the magnetic field of the solenoid changes its direction. In the upper row of the figure 4.2

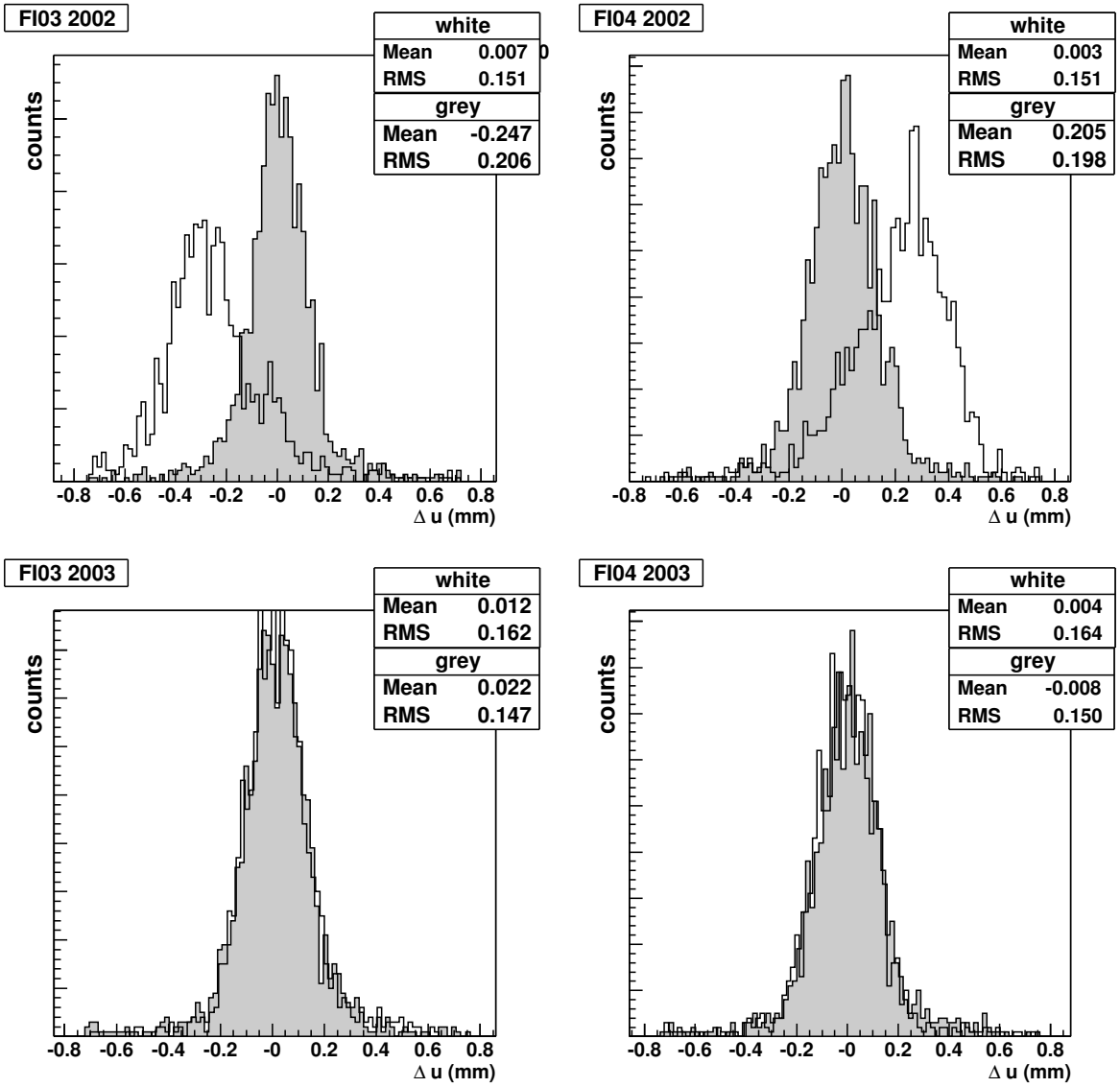

Figure 4.2: The residuals in FI03Y and FI04Y detectors before (white) and after (grey) reversal of the polarization. Data for 2002 and 2003 are shown in the upper and lower part of the picture, respectively.

distributions of the biased residuals Δu for FI03Y and FI04Y, obtained for the 2002 data, before (white background) and after (grey background) the target polarization reversal, are shown. Mean values of the biased residuals after the reversal are shifted by a few hundred micrometers compared to the situation before the reversal. Moreover the mean value of Δu for FI03 and FI04 are shifted in the opposite directions.

Two possible explanations of the observed effect were given:

- the frames of the FI detectors are magnetized, therefore when the magnetic field changes the FI03 and FI04 move.
- FI03 was attached to the target magnet. The fringe field of the SM1 overlaps the magnetic field created by the target solenoid. As a result the whole target magnet may move, and therefore also the FI03.

Between the 2002 and 2003 data taking the FI03 was separated from the target magnet. In the 2003 data mean values of Δu distribution do not change after the field reversal, cf. bottom row in figure 4.2. It was proved that the source of the Δu mean value shift was a movement of the target platform as a whole during the polarization change. The described problem also shows a limitations of the alignment procedure: in reality only the FI03 moved whereas positions of both detectors had to be changed according to the alignment results. The target platform movement can be a source of the asymmetry bias. Therefore it is discussed in more detail in section 5.7.5.

4.7.4 Alignment with magnetic field and the momentum bias

To check the alignment program the following test was done. In the *detector.dat* obtained after the whole alignment procedure, positions of the FI01 and the FI02 were artificially changed by 1 mm, in both X and Y directions. Afterwards the data from a standard physics run were reconstructed. Only FI detectors were included in the tracking procedure. CORAL was run in a special mode where the alignment of the FI detectors before the target was possible. Several iterations of the alignment procedure were made. Tests were repeated with the -1 mm bias in both X and Y directions. Figures 4.3 and 4.4 present the results. For each iteration shown are the positions of the FI01 and the FI02 detectors obtained after the alignment procedure.

Two important things are manifested in the figures:

- the bias is recovered much faster for FI02 than for FI01
- there is a large difference between the results obtained for the X and Y planes.

The first observation might be explained by the fact that the FI01 is the over-most tracking detector. Hits in such detectors have large weights in the reconstruction algorithm. Therefore the introduced bias on the FI01 positions will be artificially reduced by a change of the track parameters.

The second, more important, observation is a reflection of the fact that in the X plane there is one additional track parameter - the particle momentum. This parameter is not taken into account in the alignment procedure. The observation leads to a conclusion: if the detector movement biases the momentum then the detector movement cannot be found by the alignment procedure.

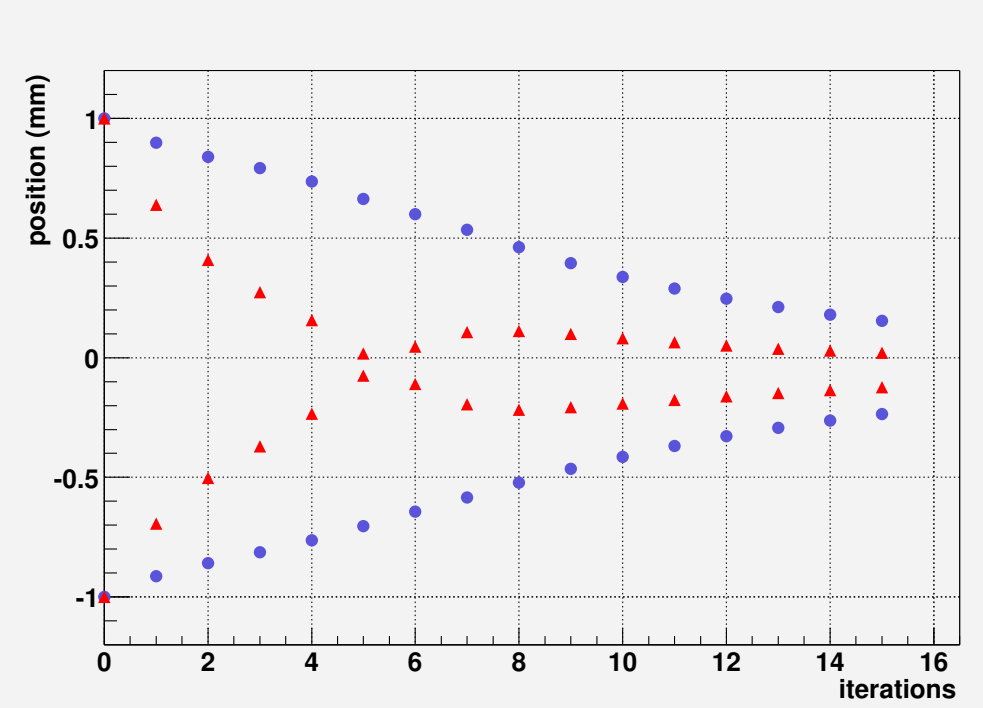

Figure 4.3: Bias recovery after each iteration of the alignment procedure for FI01 (blue) and FI02 (red), Y-planes.

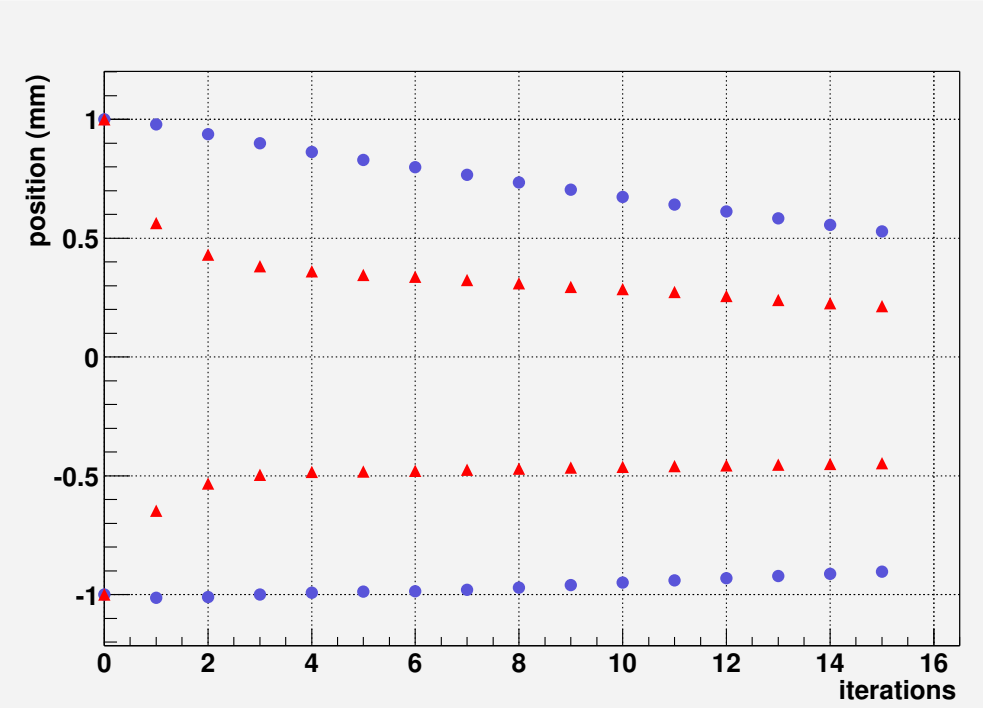

Figure 4.4: Bias recovery after each iteration of the alignment procedure for FI01 (blue) and FI02 (red), X-planes.

The beam momentum is determined in the BMS, not in the spectrometer, so the above problem is not critical for the beam reconstruction. The situation is different for the detectors at the end of the spectrometer. These detectors measure scattered muons. The momentum bias would affect many kinematic variables like y, x, Q^2. These quantities are later used for the A_1^d asymmetry measurement. Therefore the muon momentum bias gives rise to false asymmetries. To limit these effects it is crucial that the alignment without the magnetic field is of a very good quality.

4.7.5 Alignment along the beam direction

In COMPASS particles are produced at relatively small angles in the laboratory frame due to the Lorentz boost. Comparing $\partial\Delta S/\partial\delta u$ and $\partial\Delta S/\partial\delta z$ from the equations (4.7) it is clear that the precision of the 'z' alignment is much worse than that for the 'u' alignment.

Because a sensitivity to the 'z' alignment is limited other effects may play a role for the 'z' alignment results. In SAS there is a significant correlation between δu and δz. The shift of a detector by a few hundred micrometers in the 'u' direction may be compensated by a shift by a few millimeters or centimeters in the 'z' direction and still the value of χ^2 will be close to the minimal. Also the internal structure of the detectors may play a role. If a pitch varies much, than the 'z' alignment would give results which are a reflection of the weighted pitch value rather than the real 'z' position of the detector.

For the physics runs the alignment of the LAS spectrometer was done using δu, $\delta\theta$ and δz parameters. To estimate the accuracy of the 'z' alignment relative distances between different planes of the detector were used. These are usually known much more precisely than the position of the detector itself. The only reasonable results were obtained for the DC and the MM detectors. For all of them the corrections derived from the alignment program were around 0.1 mm. For the MM there were some systematic shifts. They pointed towards a hardware error and indeed it turned out that the distance between the planes should be enlarged. In table 4.3 the results of the 'z' for alignment for the ST detectors are presented. In the first column there are detector planes for which the distance is computed. In the second and third column there are the nominal plane distances and those obtained from the 'z' alignment, respectively. In the last column there is a difference of the values in the second and third column.

detector planes	nominal distance (mm)	alignment results (mm)	difference (mm)
ST03X1ub ST03X1db	6.6	0.6	6.0
ST03Y1ub ST03Y1db	6.6	6.1	0.6
ST03U1ub ST03U1db	6.6	6.8	0.1
ST03V1ub ST03V1db	6.6	1.2	5.4
ST03X2ub ST03X2db	6.6	7.3	-0.6
ST03Y2ub ST03Y2db	6.6	6.9	-0.3
ST04V1ub ST04V1db	6.6	-0.3	6.9
ST04Y1ub ST04Y1db	6.6	6.7	-0.1
ST04X1ub ST04X1db	6.6	3.1	3.5

Table 4.3: Results of the 'z' alignment for the ST detectors

For some of the ST planes the results of the 'z' alignment look unreasonable - the upstream and downstream planes have been found at almost the same place. Analogous problem was observed for the GM. Here the relative distance between X-Y and U-V planes should be zero. Unfortunately after the alignment this distance was not equal to zero; moreover, differences increased for detectors which were further downstream the target. There were attempts to fix the relative distances between planes in a detector. This was done but there is no simple way to check whether the obtained results are correct.

The pitch alignment was introduced after the observation that the 'z' alignment had failed. The pitch correction was introduced to partially recover the 'z' misalignment, cf. section 4.1. The impact of the pitch correction on the data reconstruction performance was checked. The alignment was done with and without the pitch correction. The reconstruction quality was checked for both alignments. In table 4.4 the differences between tracking performance for these two alignment procedures are shown. A comparison was done for semi–inclusive and inclusive triggers separately. The relative change of the parameters in percent is presented. Positive numbers indicate that reconstruction with the pitch correction resulted in a larger value of a given variable.

	semi–inclusive	inclusive
all tracks	0.22 ± 0.14	0.00 ± 0.15
tracks in SM1	0.16 ± 0.10	-0.14 ± 0.21
tracks in SM2	0.10 ± 0.11	0.09 ± 0.12
μ' tracks	-0.09 ± 0.17	-0.18 ± 0.21
beam tracks	0.03 ± 0.05	-0.06 ± 0.04
PV	0.8 ± 0.7	0.9 ± 0.6
tracks in PV	-0.16 ± 0.26	0.20 ± 0.08
μ/μ'	0.4 ± 0.2	1.3 ± 0.4
χ^2_{all}	-5.6 ± 0.4	-2.1 ± 0.8
χ^2_{SM1}	-6.1 ± 0.2	-2.4 ± 1.0
χ^2_{SM2}	-2.0 ± 0.4	-1.9 ± 0.5
χ^2_{μ}	-1.3 ± 0.7	-2.4 ± 1.0

Table 4.4: Comparison of the tracking performance for alignment with and without the pitch tuning. The relative change of the parameters in percent is shown for inclusive and semi–inclusive triggers.

For the most important reconstruction parameters, cf. section 4.5, the difference between the two alignments is close to zero - no improvement was found. The only change is a slightly better value of χ^2/ndf for the alignment where the pitch was used. The improvement of the K^0 reconstructed mass width was not checked. However, the value of χ^2/ndf did not change significantly, therefore no big improvement in the reconstruction was expected.

4.7.6 The day-night effect

Mean value of the residuals, $< \Delta u >$, for a few tenths of runs as a function of time when the run was taken is shown in figure 4.5. A clear periodic structure is visible. Observed effect

is connected to the temperature changes during the day in the experimental hall. Due to the temperature variations the detectors change their positions. In many cases the position change is larger than the resolution of detectors. To cancel this effect a special procedure, run-by-run alignment, was implemented. In this procedure for each run an alignment was performed. Although the movement of the detectors was large, the improvement for the reconstruction performance was found to be small. Since the procedure consumed a lot of CPU time run-by-run alignment has not been continued.

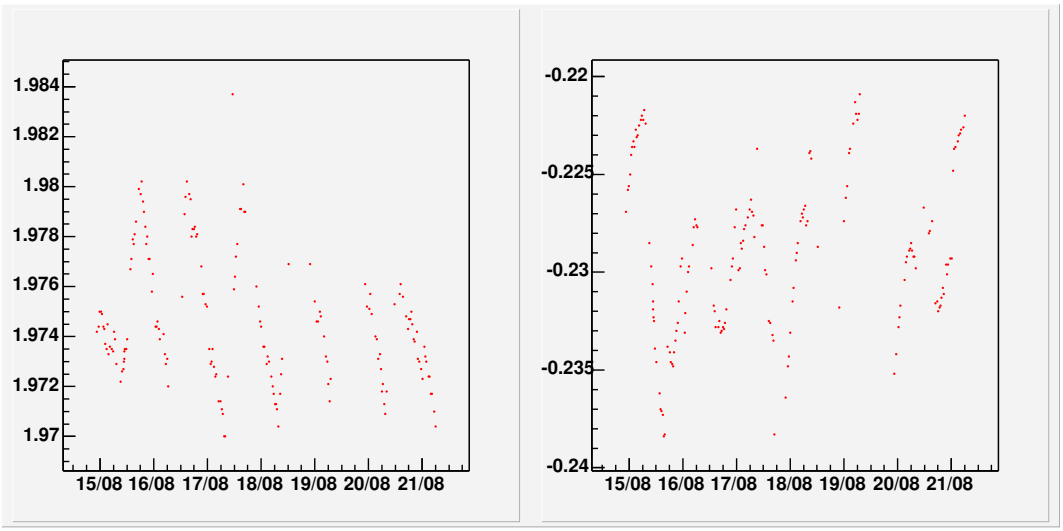

Figure 4.5: The day-night movement of GM05 centre. The values on the 'y' axis are x (left) and y (right) centre position and are given in centimeters. The values on the 'x' axis are days. Figure thanks to [97].

Chapter 5

Data analysis

In this chapter details of the data analysis are given. First the events selection is presented. Then the external information needed for A_1^d extraction are discussed. Finally different methods of the asymmetry extraction are given. A large part of the chapter is dedicated to a description of the systematic studies which were done in order to search for the asymmetry bias.

5.1 Data grouping in COMPASS

The COMPASS data are grouped into "configurations". In each of the so called "consecutive configuration" there are data with (usually) only one field reversal in between. There is also the so called "global configuration" containing data from certain period of data taking, usually one week. During that time the experimental area is supposed to be closed. The former type of data grouping is used in analyses which have a lot of data *e.g.* A_1^d, the latter is used in the opposite case.

5.2 Event selection

The A_1^d asymmetry is an inclusive quantity. This means that to measure it only information about incoming and scattered muons is needed. Information about hadron states created in the interaction is not necessary. Unfortunately a purely inclusive measurement is impossible in the low x and low Q^2 region. The main reason is a precision of the vertex resolution. Because of the small μ' scattering angle the uncertainty of the vertex position is so large that one cannot conclude in which target half the interaction occurred. In such a situation asymmetry measurements are impossible. The way to overcome the problem was found by the SMC [11]: A_1^d is measured only for events in which at least one hadron is detected, this is the so called "hadron method". An additional track in the vertex fit improves the vertex precision enough to distinguish between the target cells in which an interaction has occurred. COMPASS does not detect inclusive events in the low x, Q^2 region as are semi-inclusive triggers are used, see section 3.4. So the hadron method has to be used anyway.

This section is devoted to event selection for the A_1^d and g_1^d measurements using the "hadron method". Certain cuts were chosen to be compatible with the g_1^d analysis in COMPASS for $Q^2 > 1$ GeV^2 [56].

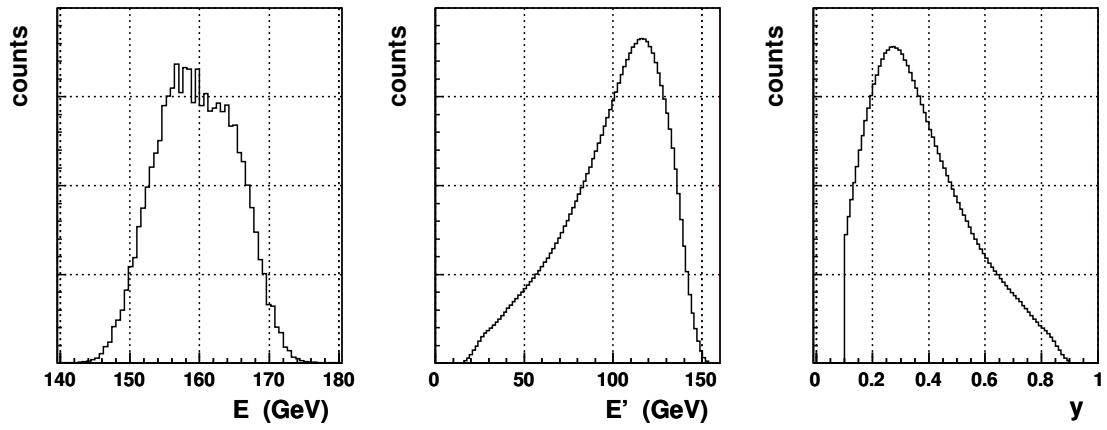

Figure 5.1: Distribution of the beam and scattered muon energy and y for finally selected events.

5.2.1 Kinematical cuts

Selected events have to contain a reconstructed beam (μ) and a scattered muon (μ') tracks. The primary interaction vertex, PV, has to be reconstructed too. The PV should contain both the beam and the scattered muon as well as at least one additional track (a hadron candidate).

The beam momentum has to be in the range between 140 and 180 GeV. The next cut, $y = \nu/E < 0.9$, removes events for which large radiative corrections are expected. The cut removes events with low μ' momentum too. A muon with low momentum may come from a pion decay and later be incorrectly identified as a μ'. Because of the $y < 0.9$ cut no additional requirement concerning the minimum μ' momentum was set. An additional cut, $y > 0.1$, removes events with poorly reconstructed scattered muons or beam halo muons misidentified as scattered ones. Because of small y values these events have a very small depolarization factor which means that the information about A_1^d is highly diluted. The distribution of the beam and a μ' energy as well as y is presented in figure 5.1.

The Q^2 *versus* x plots before and after y cuts are shown in figure 5.2. A clear difference between the plots is visible. It comes mainly from the $y > 0.1$ criterium. For a fixed Q^2 the x interval is only of the order of or less than one decade. This is an important issue for Regge model tests, cf. section 6.4. For very low Q^2 the x range is even smaller. It is due to the large muon mass squared compared to Q^2 in the kinematic limit one reads: $Q^2_{min} = y^2 m_\mu^2/(1-y)$. For small Q^2 only small y values are allowed.

In order to prevent fake triggers the scattered muon track must have associated clusters from both stations of the hodoscope which caused the trigger (*e.g.* HI04 and HI05). A pure calorimetric trigger is a special case. For these events none of "muon" triggers should fire. The pure calorimetric trigger is in fact important for large Q^2, where the scattering angle is so large that the μ' is outside the hodoscopes' acceptance. This trigger is almost irrelevant in the low Q^2 range.

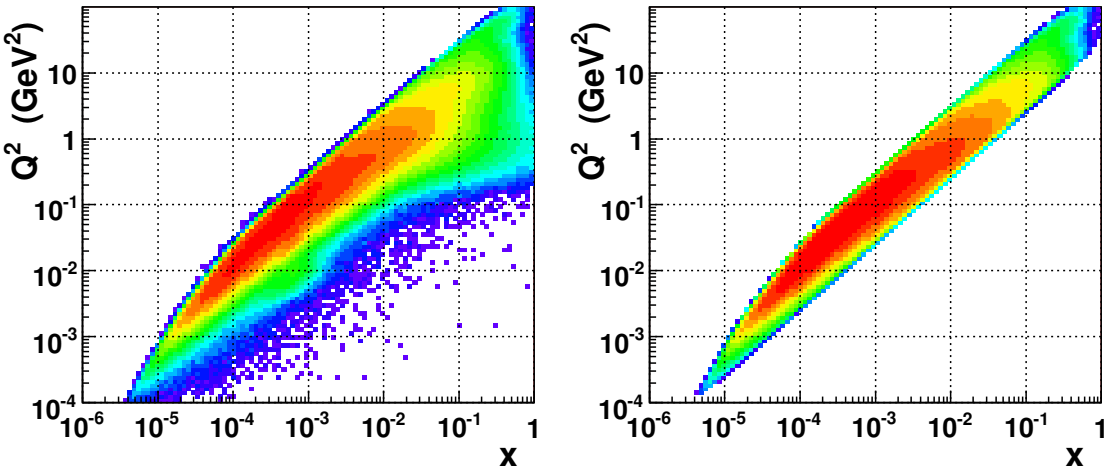

Figure 5.2: Q^2 *versus* x plot for the data sample before (left) after (right) y cuts.

5.2.2 Vertex cuts

For the A_1^d extraction only events which occurred inside the polarized target are interesting. Only events with reconstructed 'z' coordinate of the primary vertex, PV_z in the range $(-100, -40) \cup (-30, 30)$ cm are selected, cf. figure 5.3. The two cells are clearly visible as well as a gap between them; the gap is not empty but filled with liquid helium. The nominal position of the target is also marked in the figure. In the plane perpendicular to the beam axis the distance between the position of the PV and the target centre should be smaller than 1.3 cm. This conservative limit[1] is used because of the following reasons:

- the target radius is (1.50 ± 0.05) cm [98];
- position of the target with respect to the rest of the spectrometer is known with a precision of ~ 0.05 cm;
- during the COMPASS analysis, the position of the target is fixed for the whole data taking year. Between different periods the target is shifted by ~ 0.05 cm [2];
- the target moves between the field reversals by ~ 0.06 cm. More details are given in section 5.7.5. This effect is taken into account during the sample selection.

In order to cancel most of systematic errors the target cells are polarized in opposite directions. For the A_1^d measurement it is crucial to know if the interaction happened in the upstream or in the downstream cell. There is a 10 cm gap between the two cells but for small μ' scattering angle and only one additional hadron the precision of the position reconstruction of the PV along the beam axis, δPV_z, may be larger than the gap size.

[1] Other COMPASS analyses use 1.4 cm cut.

[2] In fact most of the effect does not come from the target movement but from changes in a relative alignment of the target with respect to rest of the spectrometer.

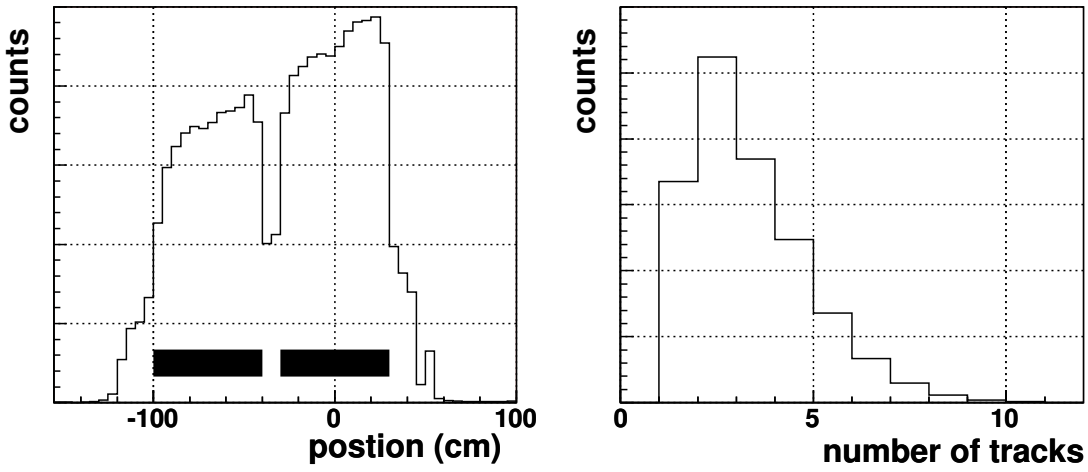

Figure 5.3: Left: reconstructed 'z' position of the primary vertex, black bands indicate the position of the COMPASS target; right: number of outgoing hadron candidates from the primary vertex for the final data sample.

Large δPV_z increase the so called vertex migration[3]. The latter effect dilute the measured asymmetry.

To minimize the dilution additional requirements on the vertex position and quality were requested, namely $PV_z \pm \delta PV_z \in (-100, -40) \cup (-30, 30)$ and $\delta PV_z < 10$ cm. The PV position in the direction perpendicular to the beam axis is known with a precision of ~ 200 μm (cf. figure 5.4) which is enough to assure that the interaction was indeed in the target as the conservative 1.3 cm radius cut is used. The last requirement is that χ^2 of the vertex must be smaller than $NDF + 3\sqrt{2 \cdot NDF}$, where $NDF = 2(NOUT+1)-3$, $NOUT$ is the number of particles emerging from the PV. A mean value of χ^2 distribution is equal to NDF, and its variation $V = \sigma^2 = 2 \cdot NDF$. For large NDF, where χ^2 distribution may be approximated by a Gaussian one, the above requirement is equivalent to a 3σ cut.

The last issue is a determination of the relative position of the target with respect to the spectrometer. The author participated in working on that subject. More details will be presented in section 5.7.5. Important things were discovered During those studies [99].

First the target turned out to be tilted. It was due to the fact that the target was supported only at the front of the upstream cell. Second, the target was not filled up completely. Therefore, an additional demand was introduced: $PV_y < 1$ cm in the target reference system. Table 5.1 contains position of the centres of the target end-cups with respect to The target tilt was found to be around 0.25 cm in the up-down direction. The target position used in this analysis is the same as in [56]. The difference between 2002 and 2003 is mostly due to the alignment[4]. In this analysis the target position is changed depending on the solenoid field: the upstream part by $\mp$ 50 μm and the downstream part by $\pm$320 μm. The position change of the upstream part is negligible compared to

[3] *e.g.* an interaction occurred in downstream cell, while PV was reconstructed in the upstream one. Moreover, outside the target there is a non-polarized liquid helium. There are events, in which muon interacted in this unpolarized material but the PV was reconstructed in one of the target cells.

[4] *i.e.* different alignment of the spectrometer with respect to global coordinate system.

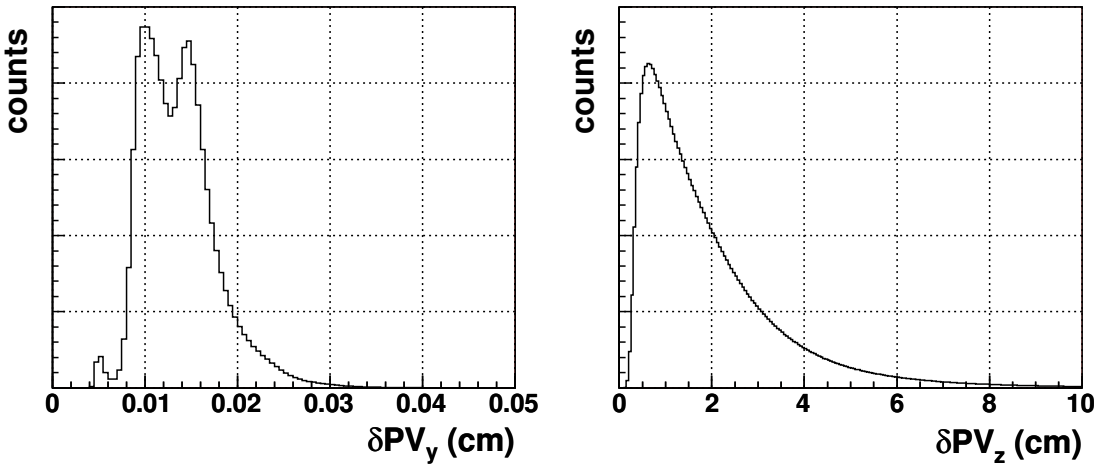

Figure 5.4: Primary vertex resolution; left: resolution along y-axis, δPV_y, which is perpendicular to the beam axis; right: resolution along z-axis, δPV_z, which is along the beam axis.

	2002		2003	
	upstream	downstream	upstream	downstream
x	-0.2	-0.3	0.0	-0.1
y	+0.1	-0.15	0.0	-0.25
z	-100	30	-100	30

Table 5.1: The target end-cups centres position in 2002 and 2003 in centimeters.

downstream part and is done for consistency.

Number of observed events depends on the muon flux. The flux is not known very precisely. Estimate of it has a large uncertainty $\sim 10 - 20\%$, [100]. Such a large error would make the asymmetries extraction impossible. However, if the flux is the same in both target cells it cancels in the asymmetry extraction, cf. section 5.4. The beam track is extrapolated to the beginning and to end of the target. Its positions after the extrapolation have to fulfill the following criteria:

- the radial distance to the target center is smaller than 1.3 cm
- $PV_y < 1.0$ cm

in this way the beam flux is the same in both target cells.

5.2.3 Hadron selection

Even if in the PV there is an additional track it does not necessarily mean that it is a real hadron track; the latter case would be a proof that a μd interaction indeed took place. Apart of hadrons and μ' outgoing from PV particles can be: *i*) beam halo muons, *ii*)

tracks created artificially by the reconstruction algorithm (ghost tracks), *iii*) electrons and positrons from photon conversion, *iv*) electrons from elastic μe scattering in the target, *v*) leptons and photons from hadrons decays.

In the first four cases the interesting μd interaction may not had happened at all. In such a case the event is a background one. It dilutes the asymmetry and should be rejected. Events with leptons and photons from hadrons decays should be kept in the sample.

Rejection of muon and ghost tracks

To reject the beam halo muons and ghost tracks it was demanded that there should be at least one track in the PV (not a beam or a μ') which fulfills simultaneously:

- $0.1 < z_h < 1$
- $p < 140$ GeV
- $z_{last} < 3500$ cm
- is not identified as a muon by the reconstruction algorithm
- $z_{last} > 350$ cm

where z_h is the hadron candidate momentum divided by the virtual photon momentum (energy) and the z_{last} is the 'z' position of the last measured hit (cluster) associated with the track. The first criterium rejects tracks which reconstruction quality may be poor. The next three remove muons. Most of the halo muons have momenta above 140 GeV. In the COMPASS spectrometer there are hadron absorbers. One of them is placed around $z = 3500$ cm. If a track has a continuation after the absorber, most probably it is a muon. Finally, the last criterium, $z_{last} > 350$ cm, is to reject tracks which do not have a continuation after SM1. Most of them are poor quality tracks; there is a large probability these are ghost tracks. At the beginning of the analysis an additional criterium was applied: the energy deposit in both HCAL is greater than 30% of the overall particle energy. This requirement was removed, information from the calorimeters was missing for many hadrons. It was checked that the A_1^d results were not biased by removing this requirement.

Rejection of elastic μe scattering events

The elastic μe scattering occurs at $x = m_e/m_p \approx 5.5 \times 10^{-4}$. To remove these events the criteria of [19] were used: ratio of the electron and the virtual photon energies was in the range $0.63 < E_e/E_{\gamma^*} < 1.27$. The cut was applied to events with only one "hadron" candidate and $3.55 \times 10^{-4} < x < 8.90 \times 10^{-4}$. In the COMPASS case too few events were rejected by this method. Distribution of E_h/ν ratio is presented in figure 5.5. No sharp peak around $E_h/\nu \approx 1$ is observed. In COMPASS the ECAL could not be used in order to distinguish between electrons and hadrons as it was not present in 2002 and only partially equipped in 2003. Finally the above method of rejecting μe scattering was not used.

Due to the momentum conservation the electron follows the virtual photon direction. The latter can be obtained from the known μ and μ' three-momenta. The angle between the virtual photon and the electron, θ, should thus be 0. The distribution of the product of θ and the charge of the hadron candidate, $q\theta$, is shown in top left plot of figure 5.6. A clear

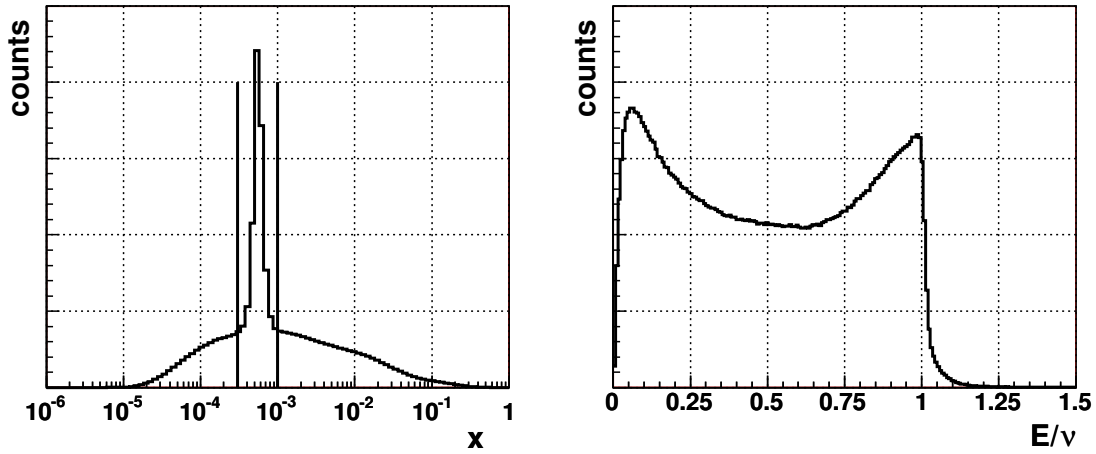

Figure 5.5: Removal of elastic μe scattering, part 1; left: x distribution for events with one negative hadron candidate outgoing from the PV. A clear peak from the elastic μe scattering is visible. Events between the vertical lines were used in the neighbouring plot; right: distribution of the E_h/ν for events contained between the vertical lines in the left figure, this variable was used by the SMC to reject the μe scattering events. Obviously in COMPASS such rejection is not effective.

peak around 0 is seen (note the logarithmic scale). There is also a small increase in the number of events which do not have reconstructed electrons but a positive particle instead. In fact these are mostly beam halo muons which anyway are rejected by other criteria. There is also an increase in the number of events with exactly two additional particles in the PV. These events were rejected too. No sign of the μe scattering was noticed for events with more than two additional particles in the PV, see top right plot in figure 5.6. An event is suspected to be a μe scattering if:

- $2 \times 10^{-4} < x < 1 \times 10^{-3}$
- $-0.005 < q\theta < 0.002$ for 1 hadron candidate
- $-0.001 < q\theta < 0.000$ for 2 hadron candidates

The spectrum of accepted events is given as a dashed line in bottom plots in figure 5.6; bottom left: x distribution for events with only one hadron candidate before (solid line) and after (dashed line) μe rejection, bottom right: the same but for the whole data sample. The μe peak is no longer visible. The estimate of remaining μe events was done using data from the last period of the 2003 run. The ECAL acceptance was largest then. Cuts to reject the μe were applied in the whole x range. Events with one hadron candidate and with $-0.05 < q\theta < 0.05$ were selected. For these events an identified electron was required in ECAL. A particle was considered to be an electron if the energy deposit in ECAL was larger than 85% of the total energy left by this particle in ECAL and HCAL. For events with a track identified as an electron the μe peak was observed and contained about 10^3 events. The total number of events accepted for the A_1^d analysis in these bins was 10^6. Next step was to estimate a probability that an electron from the μe was identified in ECAL.

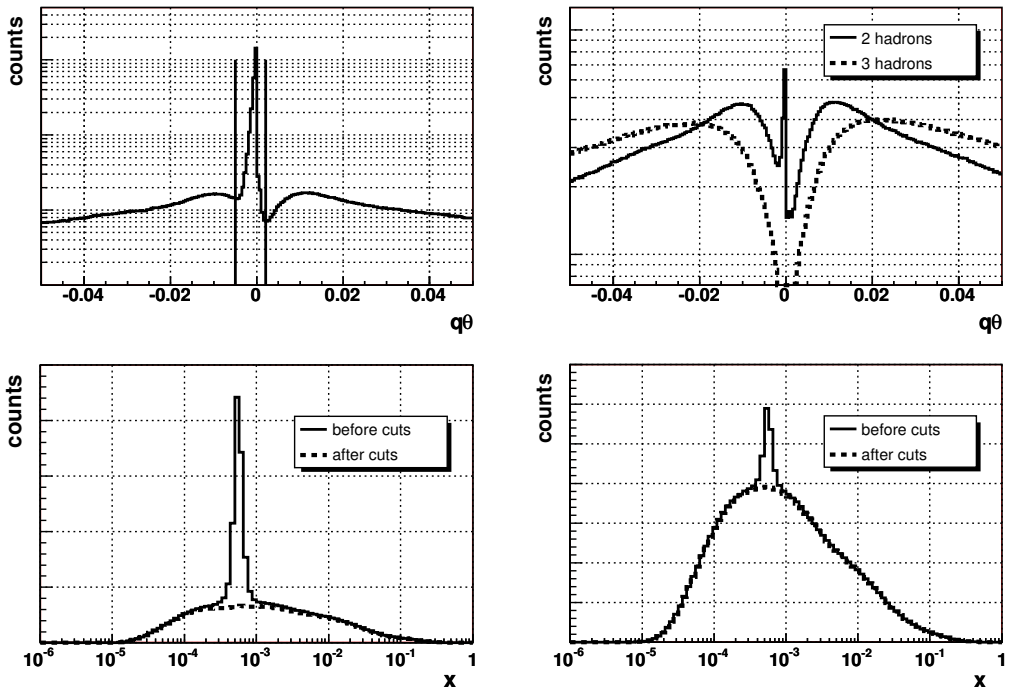

Figure 5.6: Elastic μe scattering part 2; top left: Distribution of the product of the angle between a hadron candidate and a virtual photon multiplied by the electric charge of the hadron candidate for only one additional track but muon in the PV. Events between lines are removed from further analysis; top right: same, but for two and three hadron candidates in the PV; bottom left: x distribution of events with one negative hadron candidate before and after μe rejection; bottom right: same but done for the whole data sample.

To this aim μe events fulfilling $-0.003 < q\theta < 0.000$ with one hadron candidate in the PV were selected and electron identification was performed for them. An electron was found in $(47 \pm 1)\%$ cases. Expected purity of the sample exceeded 95%. Taking into account all these factors the expected contamination of the μe scattering in the final data sample is less than 1%.

Radiative events rejection

After the above selection procedure the sample still contains unwanted radiative events in which a radiated photon converted into an e^+e^- pair so that electrons fake tracks in the PV. Most of these events are at large y and have a small angle between the direction of the photon and the converted particles, see [11]. In the kinematic range, $y > 0.6$, $|q\theta| < 0.004$, there is about 3% such events. Because of large y the depolarization factor for those events is large, which means that they are much more important from the statistical point of view than events at low y. Removing all the events in $y > 0.6$ and $|q\theta| < 0.004$ would lead to the reduction of the effective number of events by $\sim$ 13%. To estimate a yield of unwanted events data from the period where ECAL acceptance was the largest were used. The electron identification was performed and in 7% of the events, with $y > 0.6$ and $|q\theta| < 0.004$, at least one electron was identified. The expected yield of the unwanted events compared to total data sample was estimated to be: $0.03 \times 0.07 \times 4 \times 2 = 0.017$, where the factor 4 comes from a large weight of events with high y and the factor 2 takes into account the fact that only half of the electrons could be identified in ECAL. Various criteria to reject radiative events without using ECAL were tried. Finally the decision was made to use the μe rejection criteria in the whole x range. The radiative events on average were found to be below 1% as compared to 1.7% before the rejection. In the bin with highest $< y >$ about 2% of events is expected to be of radiative origin. The fact that not all these events were rejected was taken into account in the systematic error calculation of the measured asymmetry. Observe that all cuts used for electron rejection removes only tracks with a very small transverse momentum. Therefore it is expected that leptons from hadrons decays should not be removed from the data sample.

5.2.4 The final statistics

The initial data sample for the A_1^d analysis contained almost 2.1×10^9 events. The final data sample contains almost 300 million events. More details can be found in table 5.2.

The 300 million events selected in COMPASS can be compared to the SMC deuteron statistics of around 1.7 million [19]. The event kinematics is also different in the two cases. The SMC had large $< y >$ values while COMPASS has mostly moderate and small y. In table 5.3 the comparison of $< y >$ for different $< x >$ is shown.

Comparison between the two experiments has one more aspect. In the SMC the dominant error came from the statistical precision and the systematic errors were small. In COMPASS the systematic errors are as important as the statistical ones. The main issue of this analysis was a proper estimate of the systematic errors.

Criterium	events in billions	accepted events in %	accepted/initial %
initial	2.080	-	100.0
PV reconstructed	1.819	87.6	87.4
μ' reconstructed	1.417	77.9	68.1
additional track(s) in PV	0.888	62.7	42.7
PV inside the target cells	0.749	84.3	36.0
PV quality criteria	0.614	82.0	29.5
μ' signal in hodoscopes	0.537	87.4	25.8
y cuts	0.519	96.7	24.9
beam momentum cuts	0.519	99.9	24.9
μe events rejection	0.484	95.7	23.8
good hadron selection	0.413	85.7	20.4
equal flux in the two cells	0.296	71.8	14.7

Table 5.2: The number of accepted events at the different stages of the data selection.

x	$< y >$ COMPASS	$< y >$ SMC
10^{-5}	0.22	–
10^{-4}	0.52	0.68
10^{-3}	0.55	0.74
10^{-2}	0.52	0.65
10^{-1}	0.38	0.54

Table 5.3: Comparison of $< y >$ between COMPASS and the SMC; different trigger setups were used in those experiments.

5.3 Inputs to the A_1^d, g_1^d analyses

5.3.1 Beam and target polarizations

The beam and the target polarizations were discussed in sections 3.1 and 3.2 respectively. The former can be extracted on an event by event basis. Dependence of the absolute value of the beam polarization on the muon momentum is shown in figure 5.7. As it was already mentioned in 3.1 the average beam polarization for the final data sample is: -0.76. Relative uncertainty of the beam polarization is 4% as in [56].

The target polarization is measured a few times during each run. However, in the data analysis the polarization is averaged over longer periods, due to false asymmetries. More details will be given in section 5.4. For the systematic studies, the relative precision of the target polarization measurement was set to 5% as in [56].

5.3.2 $R(x, Q^2)$ parametrization

The function $R(x, Q^2) = \sigma_L/\sigma_T$, see equation (2.20), is used for the depolarization factor D calculation, cf. section 5.3.3 and for the radiative corrections calculations, cf. section

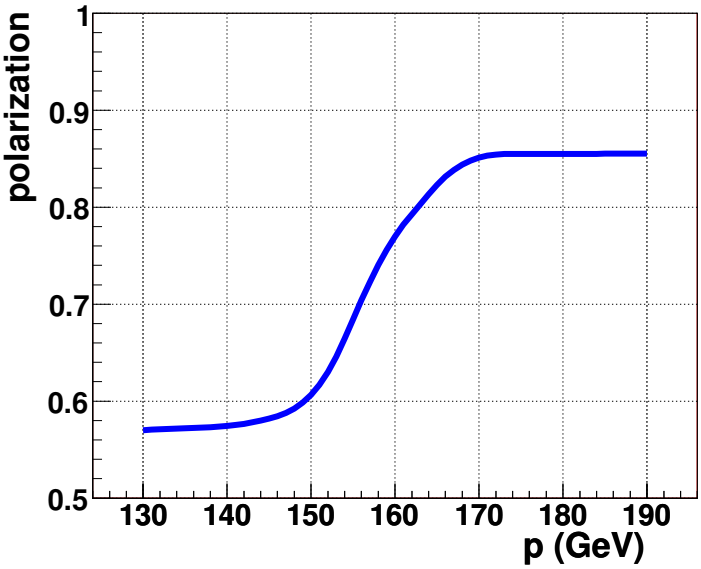

Figure 5.7: Beam polarization dependence on the incident muon momentum.

5.3.4. There is no direct measurement of R in low x and Q^2 region.

The COMPASS had used three different R parametrization depending on x:

- SLAC fit for $x > 0.12$ [101],
- NMC fit for $0.003 < x < 0.12$ [102],
- ZEUS fit for $x < 0.003$ [103].

In this analysis a new R parametrization was used. It is based on a new SLAC fit [104], for which data from several new experiments were used: E140 [105], NMC [102], CCFR [106] and CDHSW [107]. The kinematic range of data used for the fit is $0.005 \leq x \leq 0.86$ and $0.5 \leq Q^2 \leq 130$ GeV^2 [104]. However, it was suggested that the fit can be used for x as low as 10^{-6} [108]. It was checked that R values obtained from the fit are in agreement with recent H1 measurements at low x [109], [110].

In this work the low Q^2 behaviour of R obtained from [104] was modified. The simplest solution would be to have $R = 0.2 \pm 0.2$ in the whole range of x and $Q^2 < 0.5$ GeV^2. This gives a 1σ agreement with the photo-production limit, where R should be equal to zero and on the other side $R = 0.4 = 0.2 + 0.2$ is in agreement with R measured at higher Q^2 at HERA. However, that was not used. The requirements for the low Q^2 parametrization (R_{low}) were the following:

- $R_{low} \sim Q^2$ at $Q^2 \to 0$ see *e.g.* [111]
- $R_{low} = R_{SLAC}$ at $Q^2 = 0.5$ GeV^2
- $\partial R_{low}/\partial Q^2 = \partial R_{SLAC}/\partial Q^2$, at $Q^2 = 0.5$ GeV^2.

Parametrization of R at low Q^2 was thus chosen as:

$$R_{low}(Q^2 < 0.5\text{GeV}^2, x) = R_{SLAC}(Q^2 = 0.5\text{GeV}^2, x) \times \beta \left[1 - exp(-Q^2/\alpha)\right] \qquad (5.1)$$

where $\alpha = 0.2712$ GeV^2, $\beta = 1/(1 - exp(-0.5/\alpha)) = 1.1880$. As the error of the parametrization $\delta R = 0.2$ was chosen, the same as in the simplest approach. This parametrization together with [104] was used in this analysis. The comparison between NMC [102], ZEUS [103] and "new" R parametrization for $x = 0.003$ is shown in table 5.4. The value $x = 0.003$ was chosen as it was the border between NMC and ZEUS parametrization in the old R parametrization.

Q^2 (GeV^2)	NMC [102]	ZEUS [103]	this analysis
3	0.24 ± 0.06	0.26±?	0.30 ± 0.05
1	0.39 ± 0.10	0.13±?	0.40 ± 0.07
0.75	0.47 ± 0.09	0.10±?	0.39 ± 0.06
0.5	0.56 ± 0.10	0.08±?	0.36 ± 0.07
0.3	0.75 ± 0.14	0.05±?	0.30 ± 0.20
0.2	0.75 ± 0.14	0.04±?	0.24 ± 0.20

Table 5.4: Comparison of different parameterizations of R at $x = 0.003$.

In figure 5.8 the comparison between the old R parametrization and the new one used in this analysis is shown. The COMPASS kinematic range is within lines. The knowledge

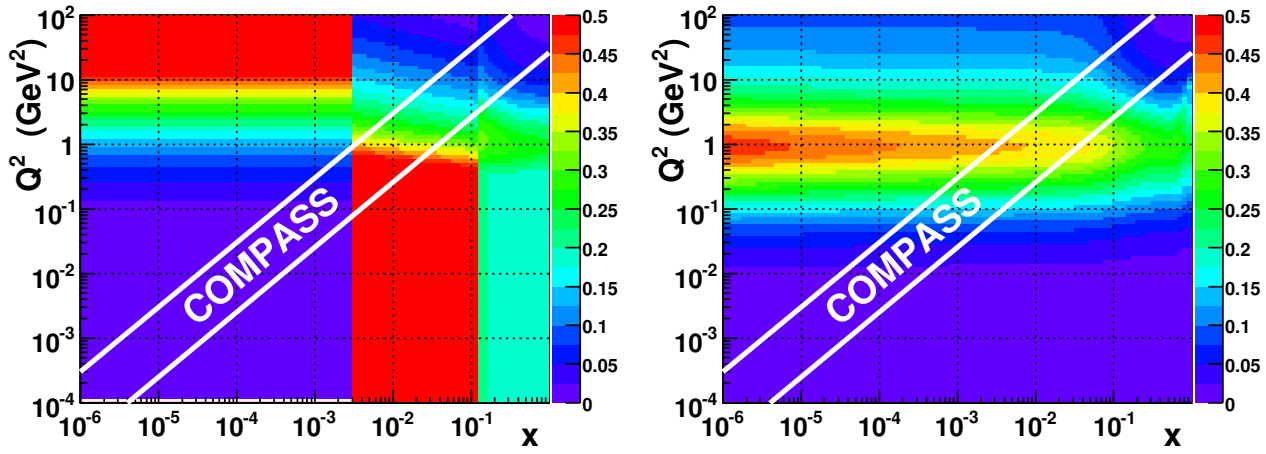

Figure 5.8: Comparison between old R parametrization and the one used in this analysis.

of R is very important for the depolarization factor evaluation. Uncertainty of R may be the highest contribution to the A_1^d systematic error at the lowest x.

5.3.3 Depolarization factor

Depolarization factor D is given by [19]:

$$D = \frac{y[(1+\gamma^2 y/2)(2-y) - 2y^2 m^2/Q^2]}{y^2(1-2m^2/Q^2)(1+\gamma^2) + 2(1-y-\gamma^2 y^2/4)(1+\gamma^2)(1+R)} \tag{5.2}$$

The distribution of D as a function of x is presented in the top left part of figure 5.9. The mean values $< D >$ as a function of x are given in the bottom-left part. The top-right plot shows D distribution as a function of y. The curves denote the depolarization factor values for three different R values, after neglecting the muon mass corrections, m^2/Q^2. Indeed these corrections must be important in this kinematic region since there are many events observed above the $R = 0$ line. Finally in the bottom-right plot of figure 5.9, $< \delta D/D >$ values as a function of x are presented. The error of the depolarization factor is large in the small x region where it exceeds 100%. Such effect was not observed in the SMC, cf. [19]. The $\delta D/D$ is larger in COMPASS compared to the SMC because of lower y in the former experiment; the relative error $\delta D/D$, which is connected to dR/R, is larger for small y values.

5.3.4 Radiative corrections

The A_1^d asymmetry as well as structure functions g_1^d and F_2 are defined in the so called one-photon approximation (Born approximation), which means that only one photon is exchanged in the μN interaction. Therefore contributions from the so called radiative events have to be subtracted from "raw" asymmetries in order to obtain A_1^d, g_1^d in Born approximation. Examples of Feynman diagrams for radiative processes are shown in figure 5.10. Corrections are applied to the leptonic current, the vertex and to the virtual photon. Corrections to the hadron current were estimated in [112] and found to be negligible, thus neglected.

Relation between the spin independent (dependent) total cross-section $(\Delta)\sigma^T$ and the cross-sections in the one-photon exchange approximation $(\Delta)\sigma^{1\gamma}$ can be written as:

$$\bar{\sigma}^T = v\bar{\sigma}^{1\gamma} + \bar{\sigma}_{tail} \qquad\qquad \Delta\sigma^T = v\Delta\sigma^{1\gamma} + \Delta\sigma_{tail} \tag{5.3}$$

where $v \approx 1$ takes into account the vertex and the vacuum polarization corrections. The $(\Delta)\bar{\sigma}_{tail}$ can be expressed as a sum of three different contributions:

$$\bar{\sigma}_{tail} = \bar{\sigma}_{tail}^{el} + \bar{\sigma}_{tail}^{qel} + \bar{\sigma}_{tail}^{inel} \qquad\qquad \Delta\sigma_{tail} = \Delta\sigma_{tail}^{el} + \Delta\sigma_{tail}^{qel} + \Delta\sigma_{tail}^{inel} \tag{5.4}$$

The elastic tail, $\bar{\sigma}_{tail}^{el}$, and quasi-elastic tail, $\bar{\sigma}_{tail}^{qel}$, take into account the elastic scattering of muons off the nucleons and nuclei which are in the target. If an energetic photon is emitted in an elastic scattering and only the incoming and scattered muons are measured, such the event will be misidentified as a DIS event. For events at small x and large y the contribution from the elastic tail can be much larger than $\bar{\sigma}^{1\gamma}$ itself. Finally the inelastic tail $\bar{\sigma}_{tail}^{inel}$ takes into account events where an inelastic interaction μN took place but a radiative photon was emitted, therefore the event kinematic has been changed. In the

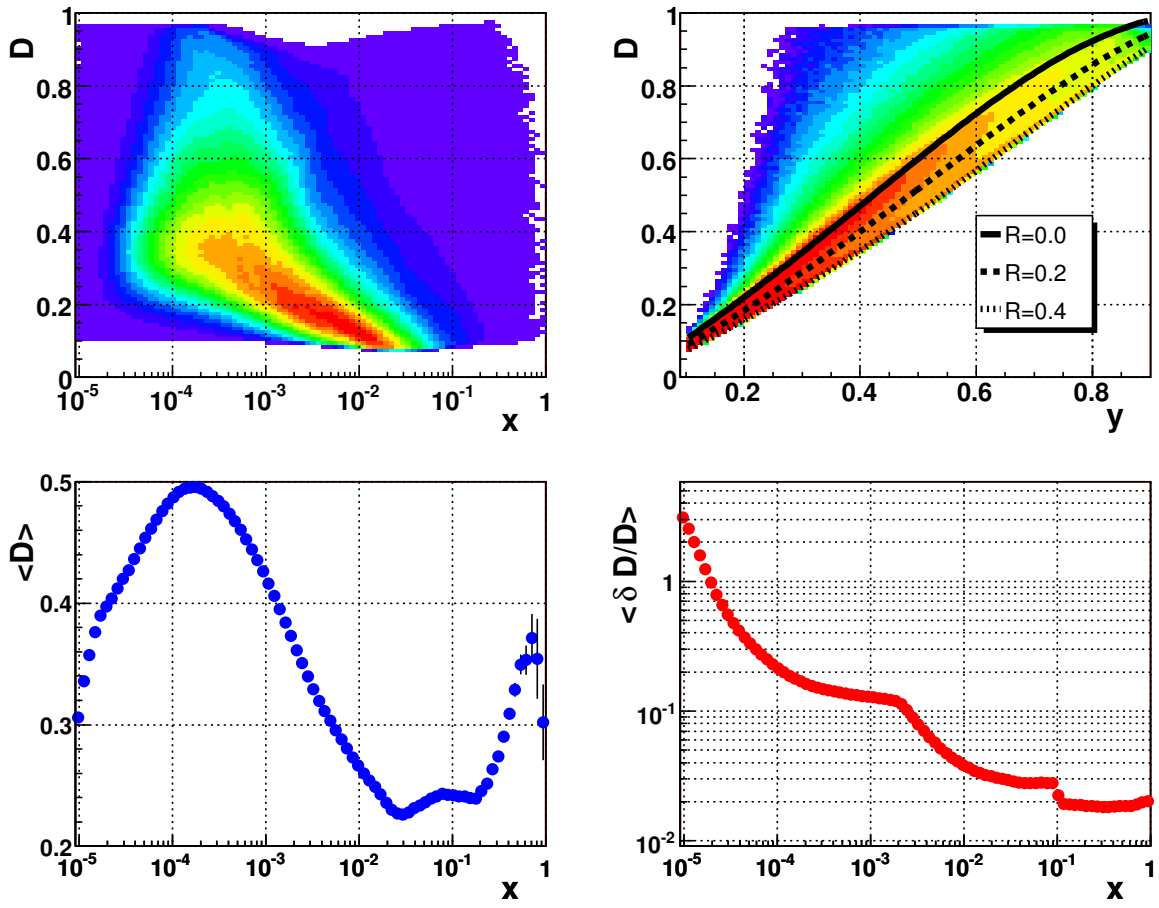

Figure 5.9: Depolarization factor in COMPASS; top left: depolarization factor as a function of x for the final sample; top right: depolarization as a function of y, the lines indicate the depolarization factor value without the muon mass correction for three different R values; bottom left: average value of the depolarization factor as a function of x; bottom-right average value of the $\delta D/D$ as a function of x.

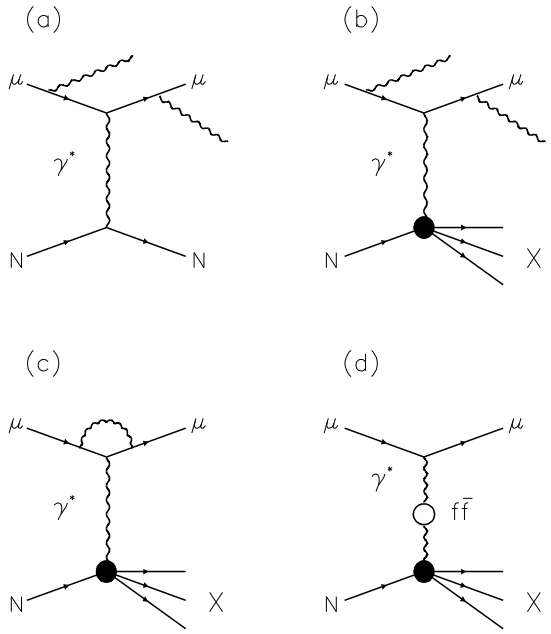

Figure 5.10: The Feynman diagrams of the radiative processes. a) "elastic tail", b) "inelastic tail", c) "vertex correction", d) "vacuum polarization" ($f\bar{f}$ denotes a fermion loop)

case of the "hadron method" used in this analysis the elastic and quasi-elastic tails can be neglected, as a reconstructed hadron is a proof that an inelastic interaction took place.

In this analysis the radiative corrections have to be included in two stages of the analysis: first in the dilution factor, cf. section 5.3.5, and second as additive corrections to A_1^d asymmetry which are discussed below.

In events where a radiative process took place the value of x is always smaller than the real x of the interaction. Since A_1 raises with x, the radiative events with higher x and therefore larger asymmetry will be on average reconstructed at lower x. Because of this the measured asymmetry, at a given x is larger than in a case where radiative events would be removed.

The measured asymmetry, A_1^T, can be expressed as:

$$A_1^T = \rho(A_1 + A_{rc}) \tag{5.5}$$

where $\rho = v\bar{\sigma}^{1\gamma}/\bar{\sigma}^T$, was taken into account in the dilution factor cf. section 5.3.5. Both factors ρ and A_{rc} were calculated using the POLRAD program, [113], [114]. The results for A_{rc} and $A_{rc}/\delta A_1^d$ are shown in figure 5.11. Values of A_{rc} are small, below 0.01 at all x. For the low x region they were found to be less than 0.001. To decide whether A_{rc} can be neglected the quantity $A_{rc}/\delta A_1^d$ was checked. It was found that for moderate $x \sim 0.1$ the radiative corrections are large compared to the statistical error of A_1^d, $A_{rc}/\delta A_1^d \approx 0.3$, and cannot be neglected. Systematic studies of A_{rc} were performed. The A_{rc} were obtained using different input information: R, F_2, A_1^d. The maximum difference between A_{rc} obtained during these studies was associated with a systematic error of A_{rc}. This error was taken into account in the total systematic error of A_1^d and g_1^d.

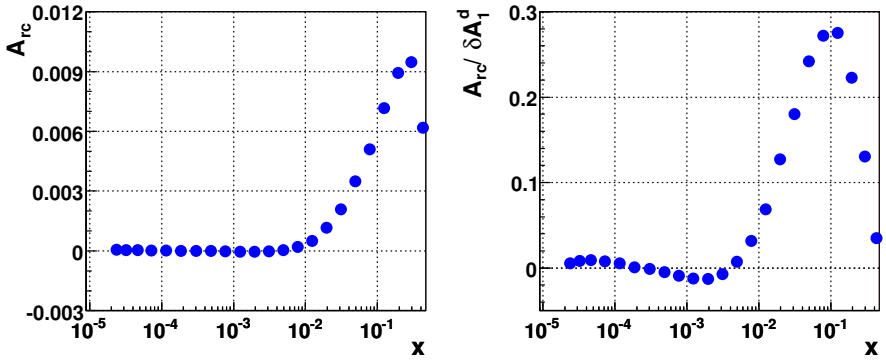

Figure 5.11: Left: The additive corrections A_{rc} to A_1^d; right: $A_{rc}/\delta A_1^d$, where δA_1^d is the statistical error of the measured asymmetry.

5.3.5 Dilution factor

The dilution factor f is introduced to estimate how much material in the target can be polarized. In this thesis only a brief description of the dilution factor is presented. It is based on [78] where details are given.

In the case of the COMPASS ^{6}LiD target four nucleons out of eight can be polarized, see section 3.2. Thus the maximal fraction of the polarizable material to the total material is $f = 0.5$. In fact the target contains not only ^{6}LiD, cf. table 3.1. Using again the simple model one gets $f \approx 0.43$. However, such approximation is too simple. The dilution factor is defined as:

$$f_{bare}(x, Q^2) = \frac{n_d \bar{\sigma}_d^T(x, Q^2)}{n_d \bar{\sigma}_d^T(x, Q^2) + \sum_{A \neq d} n_A \bar{\sigma_A}^T(x, Q^2)} \tag{5.6}$$

where n_i corresponds to the number of nuclei of type-i in the target, $\bar{\sigma_i}^T$ is the double differential cross-section for unpolarized muon– type-i nucleon scattering. Information that there are two deuterons in the ^6LiD molecule is not included in equation (5.6). This equation can be rewritten in the following form:

$$f_{bare}(x, Q^2) = \frac{n_d}{n_d + \sum_{A \neq d} n_A \left(\frac{\bar{\sigma}_A^T(x,Q^2)}{\bar{\sigma}_d^T(x,Q^2)} \right)} \tag{5.7}$$

The ratio $\bar{\sigma}_A^T(x, Q^2)/\bar{\sigma}_d^T(x, Q^2)$ is proportional to the F_2 structure functions ratio:

$$\frac{\bar{\sigma}_A^T}{\bar{\sigma}_d^T} = \frac{F_2^A}{F_2^d} \cdot \frac{2}{A} \cdot \frac{RC_A}{RC_d} \tag{5.8}$$

The explicite dependence on x and Q^2 has been omitted for simplicity. The factor A/2 comes from the fact that structure functions F_2 are defined per nucleon. The $(RC)_i$ stands for radiative corrections. Various F_2 ratios were measured in: NMC (He, C, Ca, Li) [115], [116]; EMC (Cu) [117]; E665 (Xe) [118].

The dilution factor defined in equation (5.7) is later multiplied by $C_1 \approx 1.9$. The factor C_1 takes into account:

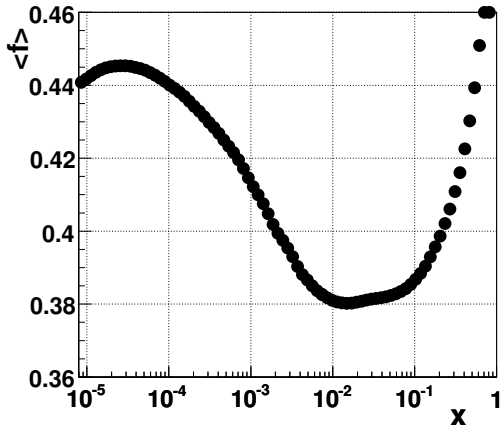

Figure 5.12: The semi-inclusive effective dilution factor f for this analysis.

- the fact that there are two deuterons in the ^{6}LiD,
- purity of the D, Li during the target production,
- the time that spins of quasi-free p, n in Li are aligned with respect to each other (when they can be treated as a deuteron),
- the probability that the deuteron is in the so called S state (not in D)

For simplicity the dilution factor, $C_1 f_{bare}$, can be multiplied by the ρ factor to take the unpolarized radiative corrections into account. These corrections where calculated using the TERAD program [119]. The ρ factor is included in the dilution factor just for convenience. The final effective dilution factor definition is therefore:

$$f = \rho C_1 f_{bare} \tag{5.9}$$

The effective dilution factor f for this analysis is shown in figure 5.12. It was calculated for semi-inclusive events which are selected using the hadron method. In the inclusive case that dilution factor is smaller, as radiative corrections are larger. At $x = 0.0001$ the ratio of the inclusive to the semi-inclusive dilution factor is 0.6, while for the SMC deuterated-butanol target it was only 0.2, cf. [11]. The difference comes from the fact that the COMPASS target is built from a lighter material than the the SMC target so the radiative corrections in the former experiment are smaller than in the latter.

The uncertainty of the dilution factor has many sources like: C_1, the target mass measurements, the cross-section ratio $\bar{\sigma}_A^T/\bar{\sigma}_i^T$, the unpolarized radiative corrections. In the COMPASS kinematic range the average relative error of the dilution factor is in the range of $6 - 8\%$.

5.3.6 $F_2(x, Q^2)$ parameterizations

The spin independent structure function F_2 is needed for the g_1^d extraction, cf. equation (2.25). Four parametrization of F_2 were considered here:

- ALLM97 [120] which is a fit to the proton world data valid for $3 \cdot 10^{-5} < x < 0.85$ and 0 GeV$^2 < Q^2 < 5 \cdot 10^3$ GeV^2 (later denoted by p1).
- a model based on parton and GVMD ideas valid for the proton and deuteron at $x < 0.1$ and any Q^2 [121], [122] (later denoted by p2)
- a model for proton based on saturation idea [123] for $10^{-6} < x < 0.1$ and 10^{-5} GeV$^2 < Q^2 < 10^3$ GeV^2 (later denoted by p3).
- a fit to the deuteron world data made by the SMC collaboration [11] valid for $9 \cdot 10^{-4} < x < 0.85$ and 0.2 GeV$^2 < Q^2 < 220$ GeV^2 (later denoted by p4).

The F_2 values for these parameterizations are shown in figure 5.13; top left: p1, top right: p2, bottom left: p3, bottom right: p4. The white background in the plots indicates that a parametrization was not available or the F_2 value was smaller than 10^{-3}. COMPASS acceptance is within lines. The g_1^d values in this thesis were extracted using the so called SMC parametrization: where possible p4 was used, while in the rest of the phase–space p2. Only data for $Q^2 < 1$ GeV^2 were used.

The SMC parametrization and the relative differences between the SMC and other F_2 parameterizations are shown in figure 5.14; top left: the SMC parametrization, top right: the SMC parametrization compared to p1, bottom left: the SMC parametrization compared to p2, bottom right: the SMC parametrization compared to p3. COMPASS kinematic range is between lines. The differences between the SMC parametrization and other parameterizations are usually smaller than 30% in the COMPASS kinematic range. As the uncertainty of the F_2 we take the largest difference between the SMC parametrization and other parameterizations[5].

5.4 Methods of asymmetry evaluation

A connection between the measured asymmetry and the virtual photon-nucleon cross section asymmetry A_1^d, cf. section 2.1.4 is discussed in details in appendix A. Here only the summary is given.

In the first approximation the following relation holds:

$$A_1 \sim \frac{1}{fDP_bP_t} A_{raw} \tag{5.10}$$

where f is the effective dilution factor, D is the depolarization factor, P_b and P_t are the beam and the target polarization, respectively and finally A_{raw} is an asymmetry extracted from the data.

Four different methods of the asymmetry extraction were used:

- 1st order method,
- 1st order weighted method,
- 2nd order method,

[5]Note, that F_2 of parametrization p1 and parametrization p3 are for the proton case; F_2^p and $F_2{}^d$ can be compared for small x where the expected difference is less than about a few percent.

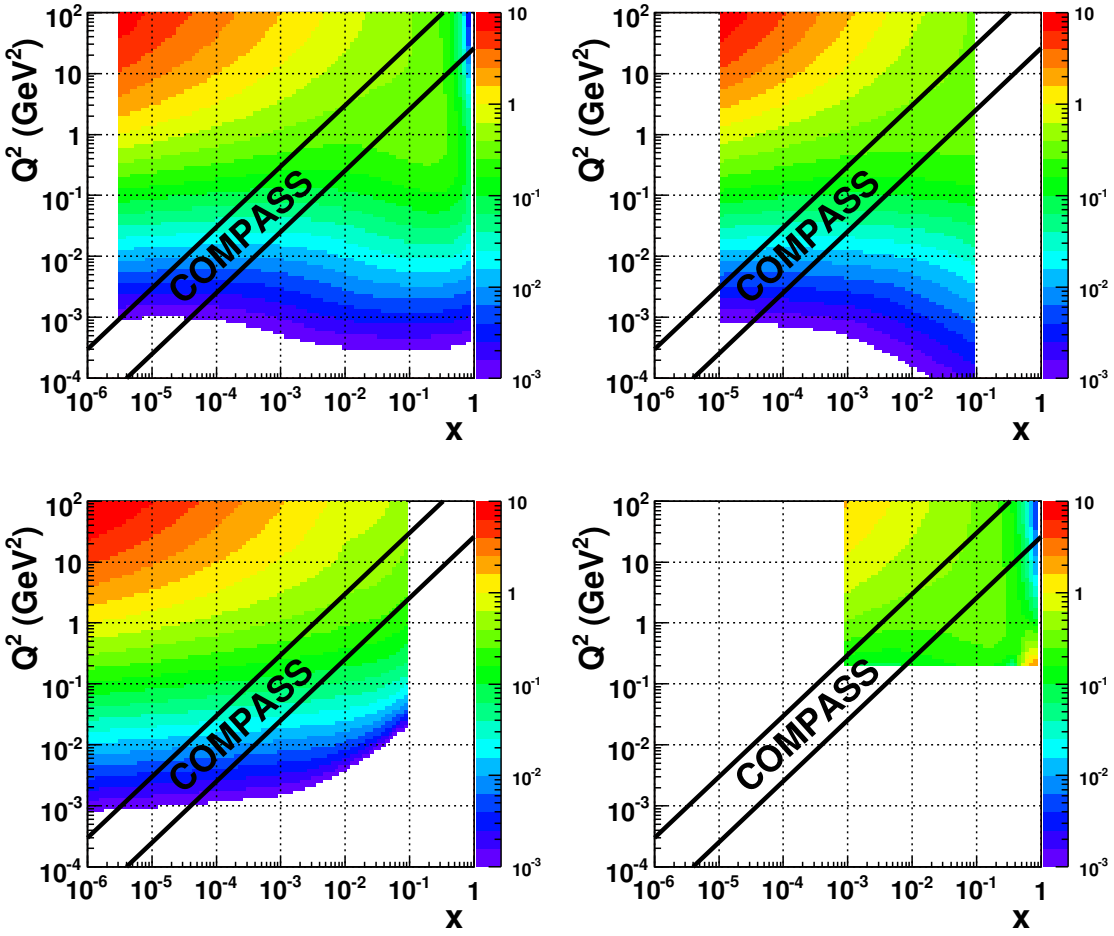

Figure 5.13: The F_2 values for different parameterizations. See text for details.

- 2nd order weighted method,

The 2nd order weighted method of the asymmetry extraction was the main method used in this analysis. It gives smaller statistical error compared to non-weighted methods and its stability is better than the 1st order methods.

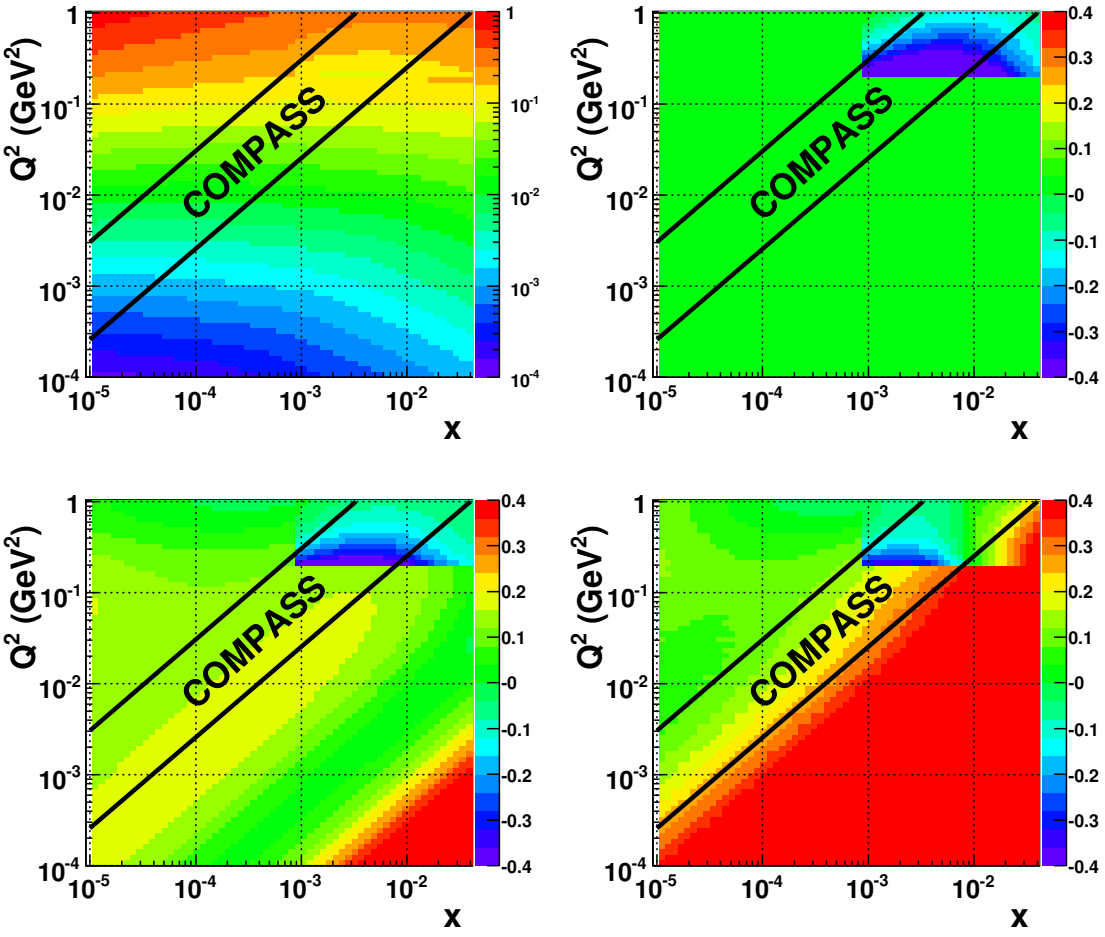

Figure 5.14: Relative differences between the SMC– and other F_2 parameterizations. See text for details.

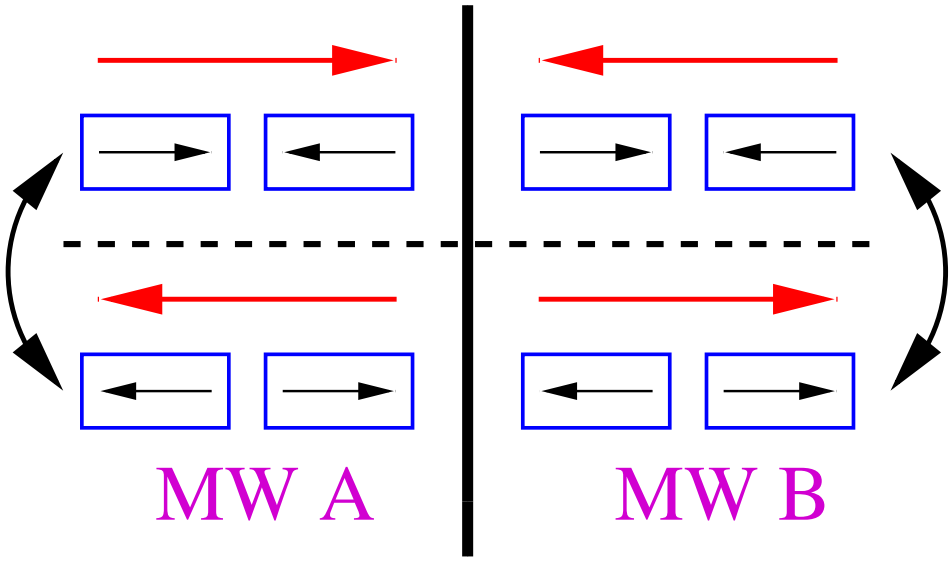

Figure 5.15: Two possible Micro Wave settings. See text for details.

5.5 False asymmetry studies

This section is dedicated to the studies of false asymmetries. Most of these were found to be consistent with zero.

5.5.1 False asymmetries

The false asymmetries may appear if the ratio of the acceptances, r, changes during the field reversal. The problem is discussed in section A.2. As it is mentioned there the field reversal should reduce a large false asymmetry which is generated by the different acceptances of the upstream and the downstream target cells. The reversal is done on average every eight hours. This gives an odd number of three reversals per day. The oddness is important: the day-night movement of the detectors is observed, cf. section 4.7.6, therefore the acceptance changes. Three reversals per day means that after two days the data from different field settings are taken at the same time of the day – a fact preventing certain false asymmetries.

Another potential danger which is taken care of is a relative polarization of the target with respect to the solenoid field. The latter is changed a few times during the year. It is said that the data were taken with different Micro Wave settings. The name comes from the fact that in order to obtain a different sign of the polarization a different MW frequency has to be used, see section 3.2. The idea of two possible MW configurations is shown in figure 5.15. Arrows indicate the polarization of target cells (black) and the direction of the solenoid current (red). For a certain MW-setting two polarization configurations are possible. Switching between them is done during the field reversal. To change the MW-setting the target has to be polarized from scratch[6]. Data from different MW-settings give a chance to cancel the effect of the acceptance changes during the field reversal.

[6]This means time losses; thus the change is done only a few times per year.

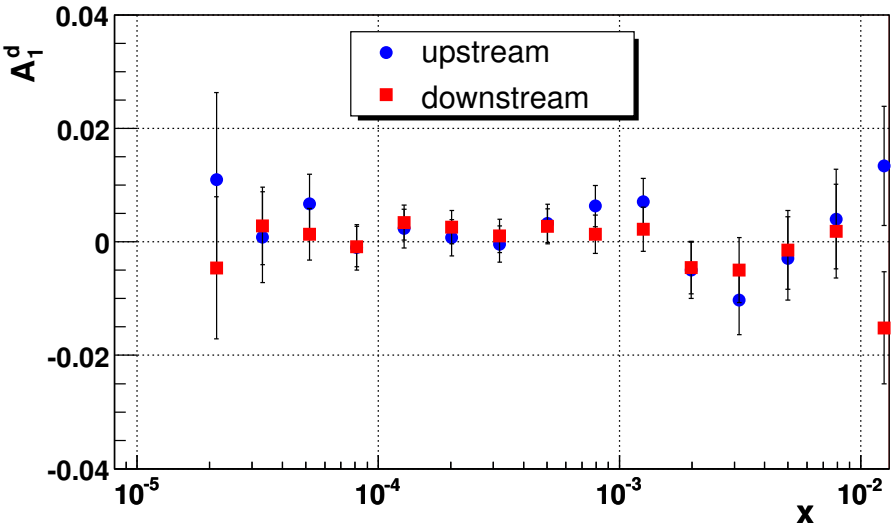

Figure 5.16: False *upstream* − *downstream* asymmetry.

Finally to prevent false asymmetries the so called bad runs and spills are removed from the analysis. A quality of every spill is checked through: average number of PV in an event, average number of tracks in an event, average number of tracks attached to a PV, the detector efficiency and many other. If the obtained numbers are far away from the average, a spill is removed from the analysis. If any of those numbers deviate for a longer period *e.g.* after the field reversal, then the data before and after the deviation cannot be combined. Taking into account all the mentioned safety procedures it is expected that for the COMPASS data false asymmetries should be small.

False asymmetry studies are made on the final data sample. This means that the precision of the false asymmetry estimation is the same as the asymmetry measurement itself. Their estimation could be done using the MC technique but it is impossible here due to a large amount of MC data required. Usually it is expected to have a MC sample at least 10 times larger than that of measured data. For the A_1^d analysis this would mean $3 \cdot 10^9$ events. Unfortunately the available MC sample is 6000 times smaller. Besides producing and storing $3 \cdot 10^9$ MC events is presently impossible.

5.5.2 Upstream–downstream false asymmetry

The first false asymmetry considered here is the so called *upstream* − *downstream* one. Each target cell is divided into 2 halves. The data from each half of a cell are combined. The expected asymmetry is zero. The non zero asymmetry could be due to the acceptance change after the field reversal or to the inhomogeneity of the target polarization. The asymmetries for the upstream and the downstream target were obtained separately. The results were found to be consistent with zero and they are presented in figure 5.16.

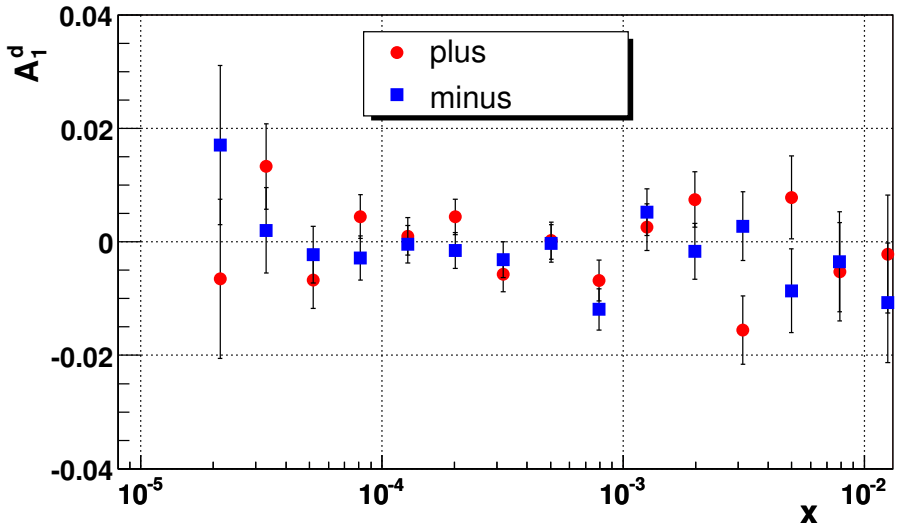

Figure 5.17: False consecutive configuration for two solenoid currents.

5.5.3 False consecutive configurations

Another way of combining data is to extract the asymmetry from the sample taken with the same direction of the solenoid field, *i.e.* after two polarization reversals. This asymmetry should be zero. However, if it is not this does not mean that there is a real problem in the data used for A_1^d measurement. The reason is that the data is grouped into configurations according to the stability of the spectrometer. It usually happened that the combined data for that false asymmetry came from different configurations[7]. This means that *e.g.* the acceptance might have changed in the meantime and the false asymmetries were generated. The observed asymmetries in the data are consistent with zero see figure 5.17. It means that stability of the spectrometer is good; it was expected that some false asymmetries could be observed but they are not.

5.5.4 Up-upstream–down-downstream false asymmetry

A way of combining data is given in figure 5.18. The target cells are divided in halves. The data from the upstream part of the upstream cell are combined with the data from the downstream part of the downstream cell. Such a combination measures a real A_1^d asymmetry. To measure false asymmetry, one has to subtract the A_1^d asymmetry obtained from data which come from the central parts of the target.

A difference of the above asymmetries is sensitive to the acceptance changes. In fact, it should be more sensitive than the previously described $upstream - downstream$ asymmetry as the combined cells are much further away from each other. Moreover, the described asymmetry is sensitive to a possible bias if too simple a method of the asymmetry extraction, *i.e.* 1st order method, was used. It was described in section A.2 that the simplest, 1st order, method introduces a bias if the acceptance ratio, r, is not equal to one. It should

[7]Usually data with only one field reversal in between are combined for A_1^d measurement.

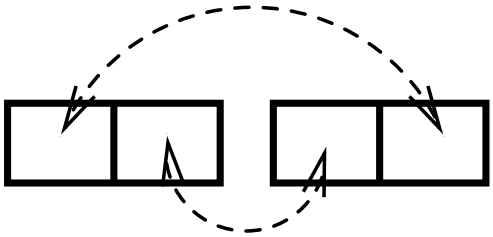

Figure 5.18: The method of combining the data for the *up-upstream* − *down-downstream* asymmetry.

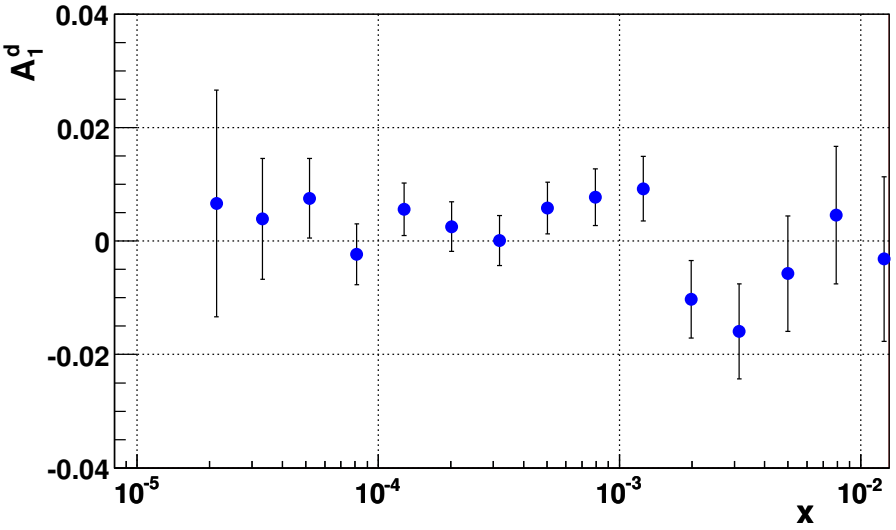

Figure 5.19: False *up-upstream* − *down-downstream* asymmetry.

be remembered that the measured asymmetry is extracted using the 2nd order weighted method, where the bias from the r factor is supposed not to exist. The false asymmetry was found to be consistent with zero[8]. The results are shown in figure 5.19.

5.5.5 Day–night asymmetry

The *day* − *night* asymmetry can be sensitive to the acceptance changes due to detector movements. The asymmetry is traditionally called *day* − *night* but in fact the data are divided according to the temperature in the experimental hall. The highest temperature was observed around 7 o'clock in evenings and the lowest around 6 o'clock in mornings. Therefore the data samples were divided into two classes: from midnight to noon and from noon to midnight. The results are presented in figure 5.20. The false asymmetry was found to be consistent with zero. A non-zero value of the false asymmetry should not be critical.

[8]The false asymmetry was also checked when the simplest, 1st order, extraction method was used. These results were consistent with zero too.

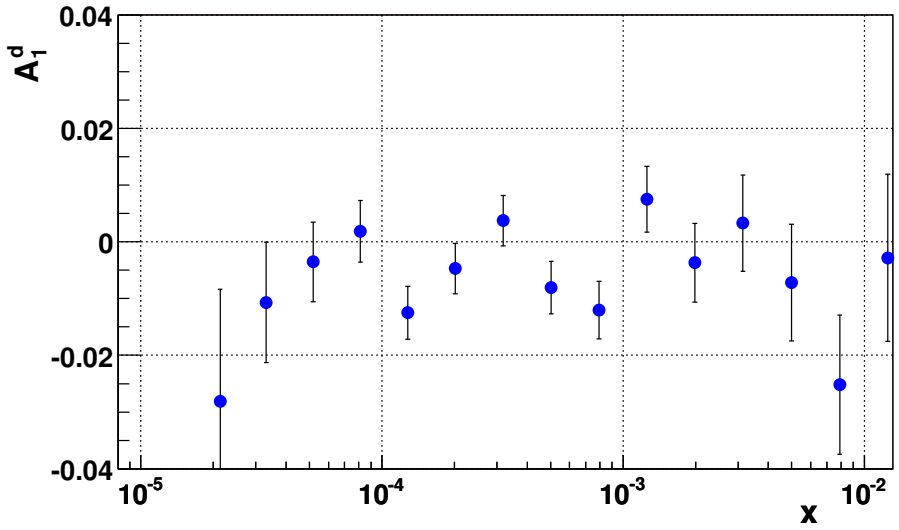

Figure 5.20: *Day* − *night* false asymmetry.

The reason is that to cancel the *day*−*night* false asymmetry the solenoid field was reversed odd number of times per day.

5.5.6 Left–right and top-bottom false asymmetries

These false asymmetries were created in the following way: the data was divided into four groups depending upon the angle of the scattered muon at the PV. The groups were: top, bottom, left, right. In each group the A_1^d asymmetry is measured, therefore interesting observables are the differences between the top-bottom and left-right sub-samples. The left-right asymmetry was found to be consistent with zero. The top-bottom was consistent with zero only for the 2003 data. The observed false asymmetries for a part of 2002 data were large, cf. figure 5.21. Finally, the cause of the problem was found. In the 2002 data, two independent alignment files, for two different solenoid currents, were needed. It was found out that for part of 2002 data, in one of the files, the dead zones of the detectors responsible for the muon identification were shifted by about 3 cm with respect to the second alignment file. The mismatch of the dead zones created large acceptance changes, which were of course a reason of large false asymmetries. The mistake was corrected and the data were reproduced. The false asymmetry for the reproduced data was finally consistent with zero.

5.5.7 Inner-outer false asymmetry

For the *inner*−*outer* asymmetry the data sample was divided according to the PV distance from the target centre. If the distance from the centre (in the plane perpendicular to the beam axis) was smaller than 8 mm the event was qualified to the *inner* sub-sample, accordingly the event with the PV distance from 8 mm to 13 mm belonged to the *outer* sub-sample. This was a test of the homogeneity of the target and of a possible bias due to

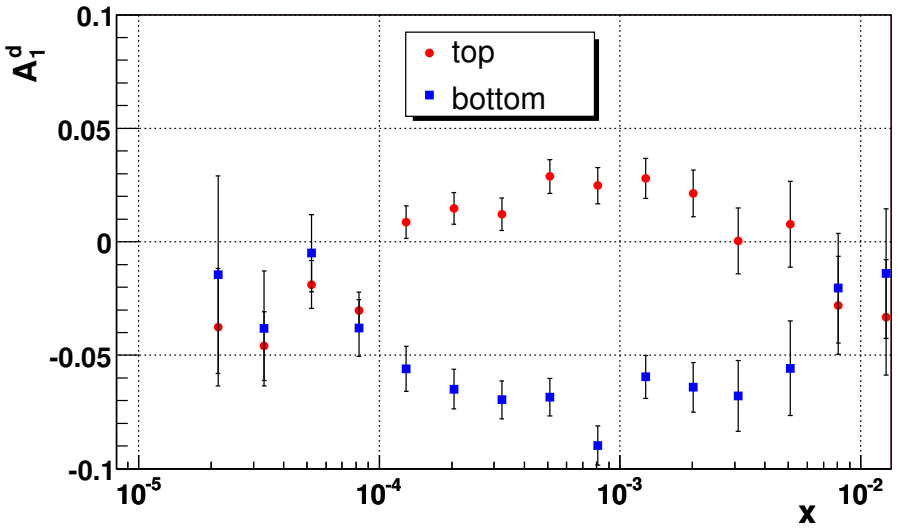

Figure 5.21: The effect of the dead zones misalignment: the *top* − *bottom* asymmetry.

the target movement between the field reversals.

In each sub-sample the A_1^d asymmetry was measured. Therefore, the false asymmetry can be observed for difference of the two. Large false asymmetries were observed for the whole data set. The reason was that described way of the sub-samples selection was wrong: the beam flux did not cancel in the asymmetry extraction resulting in an asymmetry bias.

The data were finally divided in the following way: the first set was the final data sample and the second set contained events for which the beam track was contained within 8 mm from the target centre, cf. section 5.2.2. The difference between the asymmetries from the two data sets was measured. Note that data in two sets are correlated, which had to be taken into account during the error estimation. For the above mentioned samples the square of the correlation factor is simply the ratio of the number of events in the samples. The error of the asymmetry has the following form: $\delta(A_{S1} - A_{S2}) = \sqrt{(\delta A_{S2})^2 - (\delta A_{S1})^2}$, where $\delta A_{S1(2)}$ denotes the asymmetry error for a given sample. The results are shown in figure 5.22. As expected they are consistent with zero.

5.5.8 Microwave setting false asymmetry

The data were divided depending upon the MW-setting and false asymmetries were searched for between the corresponding data sets. Note that the data were taken with two MW-settings in order to cancel a possible false asymmetry! However, it would be much better if the asymmetry did not appear at all. That would be a proof of a good performance of the COMPASS spectrometer.

At the beginning of the analysis a non zero false asymmetry was observed in the data. It was observed mostly in the 2002 data. The average value of the false asymmetry was 0.02, which was approximately six standard deviations away from zero. The situation changed after more quality checks were added to define a good hadron in an event. Results from the final data sample are shown in figure 5.23. In the upper plot the samples for 2002 and

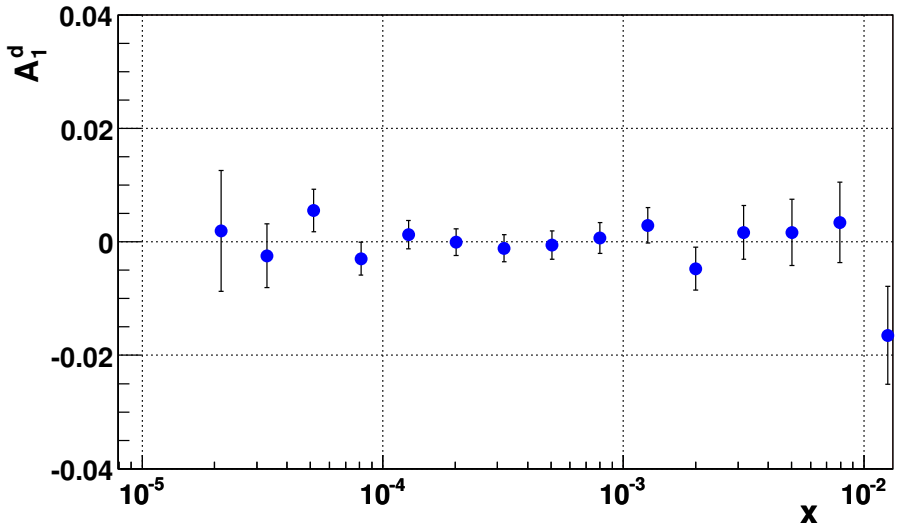

Figure 5.22: False *inner* − *outer* asymmetry.

	2002		2003	
	MW A	MW B	MW A	MW B
1-2 hadron(s)	2.1 ± 3.1	-21.0 ± 3.0	-5.8 ± 2.4	2.3 ± 2.4
3-4 hadrons	1.9 ± 3.1	-5.1 ± 2.9	2.6 ± 2.3	-3.2 ± 2.3
5+ hadrons	0.4 ± 4.1	14.5 ± 3.9	10.0 ± 3.0	-8.1 ± 3.0

Table 5.5: The $10^3 \cdot A_1^d$ asymmetries averaged in $x \in (10^{-5} - 10^{-2})$ for different years and MW-settings as functions of the event multiplicity.

2003 data are presented separately; in the lower on the whole data set is shown. Results are consistent with zero. The fact that no false asymmetry was observed came as a surprise as other analyses reported a non zero false asymmetry here [124], [125].

The data were divided into more sub-samples to search for a false asymmetries. The only correlation which was found was that the false asymmetry depends upon the number of the tracks outgoing from the PV. The results are summarized in table 5.5. The values of the asymmetry were averaged for $x \in (10^{-5} - 10^{-2})$ and multiplied by 10^3. Large deviations from zero are observed.

Using the table 5.5, it is also possible to explain, why different analyses saw non-zero false asymmetries. In [124], [125] at least two hadrons with high transverse momentum are required. Apart of the case of 1-2 hadrons in table 5.5, the difference between asymmetries for MW A and MW B, for 2002 data is around -0.6 ± 3.4, therefore negligible, while for 2003 data the difference is 10.4 ± 2.5. The same tendency was observed in [124] and [125].

A simple model was constructed to explain the observed phenomenon, namely the large differences between 1-2 hadron case and 5+ hadron case, cf. table 5.5. Due to different acceptances the average number of hadron reconstructed in the PV from the upstream and the downstream cells is different. Also, different parts of the detectors are irradiated by

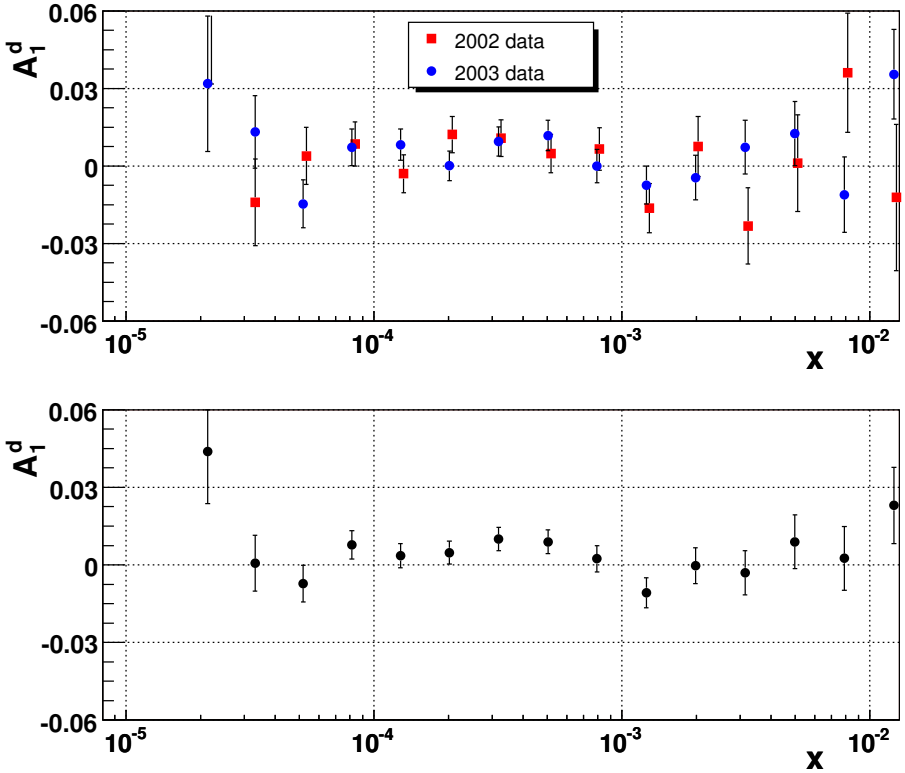

Figure 5.23: The false asymmetry between the different MW-settings.

	2.7	3	3.3	3.6	4	4.4
1-2 hadron(s)	4264	3734	3225	2754	2198	1729
3-4 hadrons	3693	3921	4032	4037	3907	3660
5+ hadrons	1371	1847	2374	2936	3712	4488
total	9328	9502	9631	9727	9817	9877

Table 5.6: Expected number of events for Poisson distribution for different values of μ, shown in the first row. Initial data sample was 10000.

	symmetric part	antisymmetric part
1-2 hadron(s)	23.2	-93.0
3-4 hadrons	23.1	-1.4
5+ hadrons	15.9	121.5
whole sample	2.3	6.2

Table 5.7: Asymmetries multiplied by 10^3 obtained with the simple model. See text for details.

tracks outgoing from the two cells. It is possible that the variation of the reconstruction probability is cell dependent.

It was assumed that average track multiplicities follow the Poisson distribution with the averages: $\mu_u = 4$, $\mu_d = 3$. Here 'u' and 'd' stand for the upstream and downstream target cell, respectively. After the field reversal the averages change. Their change can be composed of two parts: symmetric and antisymmetric. The symmetric part was assumed to be a reduction of the $\mu_{u,d}$ by 10% for the both cells. For the antisymmetric part: the average in the upstream part was decreased by 10% but it was increased by 10% in the downstream part. The 10% change of the average means 10% change of the probability of a track reconstruction. This is a very large number. However, during an asymmetry computation, for simplicity, it was assumed that $fDP_bP_t = 1$. Therefore, for A_1^d analysis, the track probability would have to changed by about 0.6% to generate the same results.

In table 5.6 a number of events, which are expected to be observed with certain track multiplicity is given. The mean values μ of the Poisson distribution are shown in the first row. The initial sample was 10000 events. These numbers were used in the asymmetry computation. The second order method of the asymmetry extraction was used. Calculated asymmetries were multiplied by 10^3 and are given in table 5.7.

The symmetric and antisymmetric parts behave in completely different ways. For the symmetric part we observe that there is almost a constant bias, if one treats separately cases with different hadron numbers. For the anti-symmetric part the bias is larger and it changes sign. This behavior is very similar to observed in the data. Note that the bias for the whole data sample, which would be used for A_1^d measurement, is around ten times smaller than for the sub-samples. To summarize: dividing the data in sub-samples depending on the number of hadrons outgoing from the PV seems to be a very sensitive test of the stability of the spectrometer. The large partial false asymmetries seem correspond to a much smaller false asymmetry if the entire data sample is used.

triggers	1st trigger	2nd trigger	1st & 2nd trigger
IT, LT	-0.6 ± 1.3	-1.5 ± 1.3	1.4 ± 3.0
IT, MT	-1.8 ± 4.3	-0.8 ± 4.2	-2 ± 10
LT, MT	-3.3 ± 3.2	-0.9 ± 4.1	5.6 ± 8.6
LT, OT	-3.8 ± 3.3	-3.3 ± 5.8	-12 ± 14
MT, OT	-8.8 ± 6.0	11.6 ± 5.8	-16 ± 12

Table 5.8: Comparison of the $10^3 \cdot A_1^d$ for different triggers.

5.5.9 Trigger-by-trigger asymmetry

The COMPASS trigger system uses four different hodoscopes (HI, HL, HM, HO) to search for a scattered muon. These detectors have different acceptance for muons outgoing the upstream and the downstream target cells. It was checked, whether there are no systematic effects between different trigger groups.

Asymmetries were measured in the region where interesting triggers overlap. A special care was taken to obtain a similar $< x >$ for the compared samples. This was important especially for OT and MT triggers, see section 3.4, as the average x was in the intermediate range where the A_1^d has a significant x dependence. Results are given in table 5.8. In the first column the compared triggers are shown. In next columns the averaged $10^3 \cdot A_1^d$ are given for the 1st, 2nd and mixed triggers. For all triggers the results are consistent at the three standard deviation level. The false asymmetries are not observed.

5.5.10 The χ^2 scan

At the first stage of this analysis the asymmetry presented in figure 5.24 was obtained. The errors seem to be overestimated[9]. A straight line fit resulted in $\chi^2/NDF = 2.81/15$; $P(\chi^2)$ is only $2.6 \cdot 10^{-4}$. The asymmetry extraction method was carefully checked but no mistake was found.

The asymmetry scan was made. In first step lower edges of bins were shifted by 1/16 of the bin size in the second step by 2/16 and so on. For measured asymmetries the straight line fit was made; χ^2 and $P(\chi^2)$ were calculated. Results are shown in figure 5.25; left: the χ^2, where NDF was always 15, right: $P(\chi^2)$. On the horizontal axis the shift of bin lower edges is given in $n/16$. The values of χ^2 and thus $P(\chi^2)$ change a lot. Note that data samples are highly correlated. A value of χ^2/NDF is important. However, it seems to be quite unstable even for highly correlated data samples.

5.6 Estimate of a limit for false asymmetries

In this section the description of the method used for the systematic error estimate connected to the false asymmetries is given. It is a modified version of a method which was previously used by COMPASS [56].

[9]Negative A_1^d values are connected with a bias discussed in 5.5.8. The bias disappear after $z_{last} > 350$ cm criterium was used for the data selection.

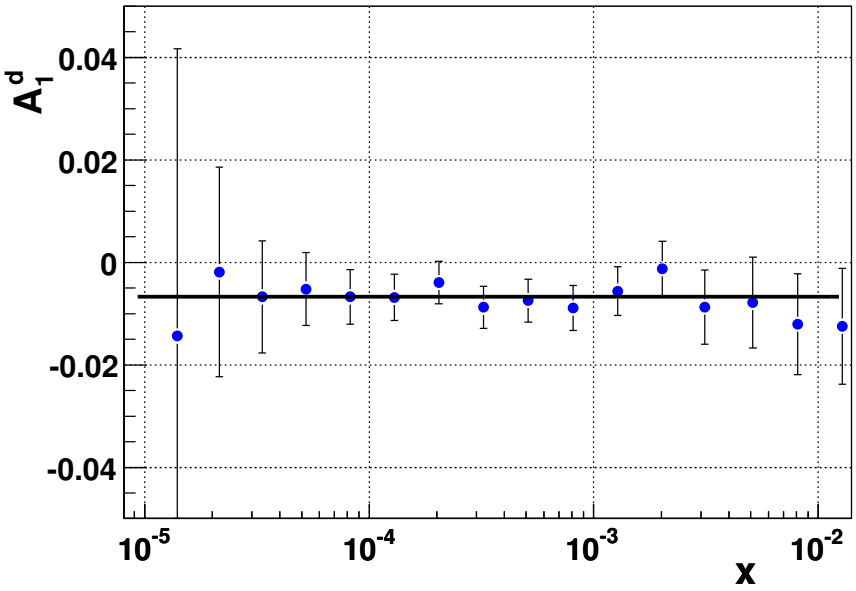

Figure 5.24: A_1^d for part of the 2003 data, first stage of this analysis.

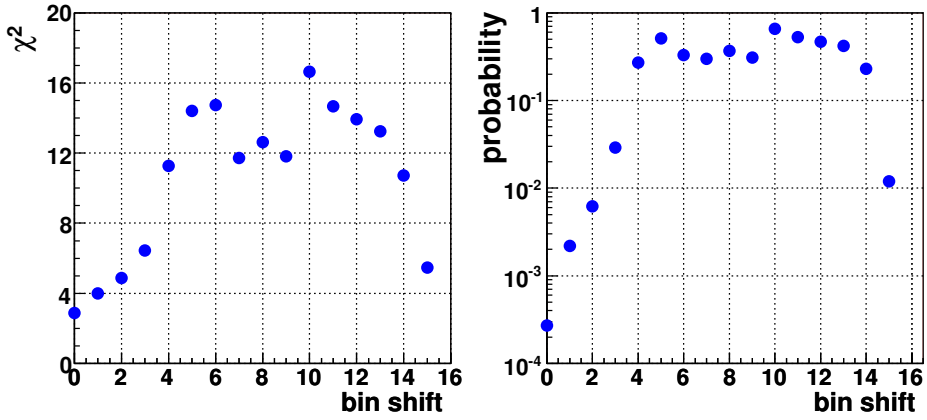

Figure 5.25: Results of the straight line fit to the data from figure 5.24 for different bin shifts. Left: χ^2 distribution, right: probability that χ^2 would be smaller.

5.6.1 Standard COMPASS method

The samples used in COMPASS analyses are divided in configurations. Let us consider the so called pull distribution:

$$\sigma_{PULL,j} = \sqrt{\frac{1}{N-1}\sum_i \left(\frac{A_{i,j} - \bar{A}_j}{\delta A_{i,j}}\right)^2} \tag{5.11}$$

where i counts the data configurations, j counts x-intervals in which the asymmetry $\bar{A}_j$ was measured, $A_{i,j}$ and $\delta A_{i,j}$ are the measured asymmetry and its error in the x-interval j and configuration i, respectively. The expected value of $\sigma_{PULL,j}$ is 1. Average values for all j intervals of $\sigma_{PULL,j}$ and $\delta\sigma_{PULL,j}$ where: $\sigma_{stat} = 1$ and $\delta\sigma_{stat} = 0.05$, respectively. The limit, σ_{sys}, for false asymmetries was constructed as:

$$\sigma^2_{MAX} = \sigma^2_{stat} + \sigma^2_{sys} \tag{5.12}$$

where $\sigma_{MAX} = \sigma_{stat} + 2\delta\sigma_{stat}$. The limit is:

$$\delta\bar{A}_{j,sys} = \sigma_{sys} \cdot \delta\bar{A}_j \tag{5.13}$$

where

$$\sigma_{sys} = \sqrt{\sigma^2_{MAX} - \sigma^2_{stat}} = \sqrt{1.1^2 - 1} \approx 0.5 \tag{5.14}$$

5.6.2 Modified pulls method

The method used in [56] was modified in two ways: *i*) by using the Bayesian 95% CL limit and *ii*) by estimating a systematic error for each measured point. It is clear that in the case of *e.g.* $\sigma_{PULL,j} = 0.8 \pm 0.1$ the limit for systematic effects is much smaller than in the case *e.g.* $\sigma_{PULL,j} = 1.3 \pm 0.1$.

Confidence limits for the signal in presence of a background are discussed in [126]. Both the signal and the background have Poisson distributions. To set the limit (*e.g.* 95% CL) the MC technique is used. Here the idea of [126] was modified to make it appropriate for the pulls distributions. A sketch of the method is shown in figure 5.26. First, a random number is generated from the $N(0,1)$ distribution. This generation is repeated until the generated sample of numbers is equal to the number of configurations into which the data are divided. For this analysis there were 97 configurations in total. The next step is the estimation of the standard deviation σ_{MC} of the obtained sample. At this point the critical decision is made: if the σ_{MC} is larger than the σ_{OBS}, which is the sigma of a pull distribution observed in the data for a certain x bin, the generation is repeated. In the case $\sigma_{MC} < \sigma_{OBS}$ the data from the generated sample are smeared by $N(0, \sigma_{sys})$. For the smeared sample the standard deviation σ_{MCsys} is calculated. If the $\sigma_{MCsys} < \sigma_{OBS}$ the "MC event" is qualified to a sub-sample A, in the opposite case to a sub-sample B. The whole procedure is repeated until the sub-samples A and B are sufficiently large. Finally, the ratio A/(A+B) is calculated. The goal of the method is to find such σ_{sys}, for which $A/(A+B) = 1 - CL = 0.05$. The method described above was used for the limit calculation in the wide range of σ_{OBS}. The typical size of the sub-samples A and B was $10^4 - 10^6$. The obtained limits are shown in table 5.9. The results were fitted by a TSpline3() function in ROOT. In this way the limit was accessible for any $\sigma_{OBS} \in (0.8 - 3.0)$.

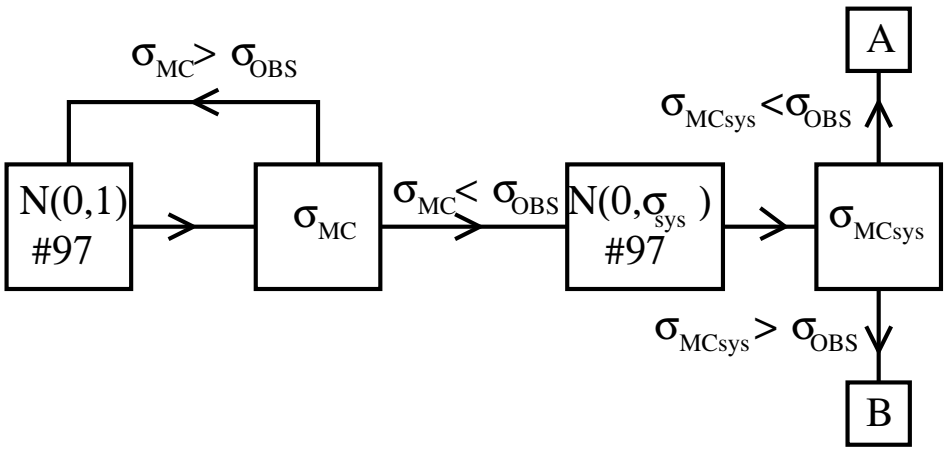

Figure 5.26: A sketch of the method used to estimate the systematic errors in this analysis.

σ_{OBS}	σ_{sys} limit	σ_{OBS}	σ_{sys} limit
0.8	0.40	1.4	1.25
0.9	0.46	1.5	1.4
1.0	0.60	1.7	1.6
1.1	0.76	2.0	2.0
1.2	0.93	2.5	2.7
1.3	1.10	3.0	3.3

Table 5.9: The 95%CL σ_{sys} limit for a given σ_{OBS}. See text for details.

5.6.3 Results

The pulls distribution for the whole data sample is shown in figure 5.27. The error of each point is $1/\sqrt{2N-2}$, where N is the number of the data configurations ($N = 97$) used for the asymmetry extraction. Most of the data points are consistent with 1. There are two points below $x = 10^{-4}$ where the difference between the observed values and expected ones is close to 3 standard deviations.

For the obtained σ_{OBS} of the pulls the 95% CL limit for the systematic effects was set using the method discussed in section 5.6.2. Results are shown in figure 5.28. For the whole x the limit is smaller than the statistical error.

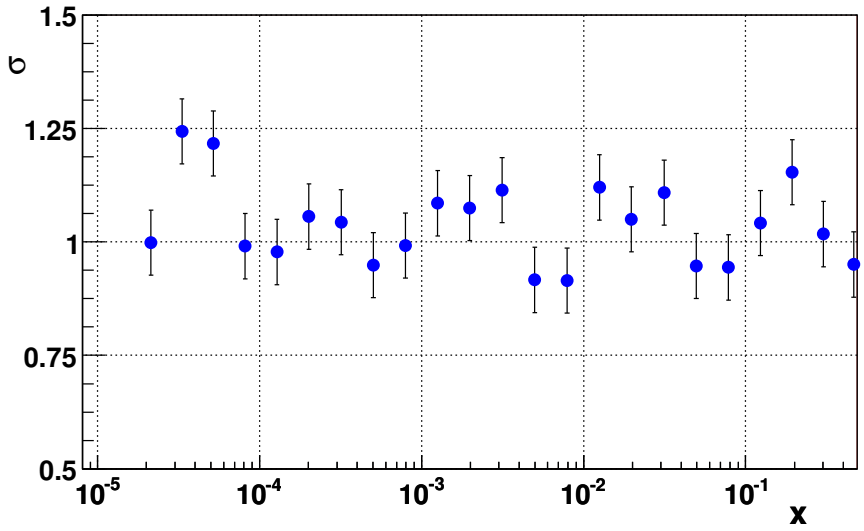

Figure 5.27: The pulls distribution for the whole data sample.

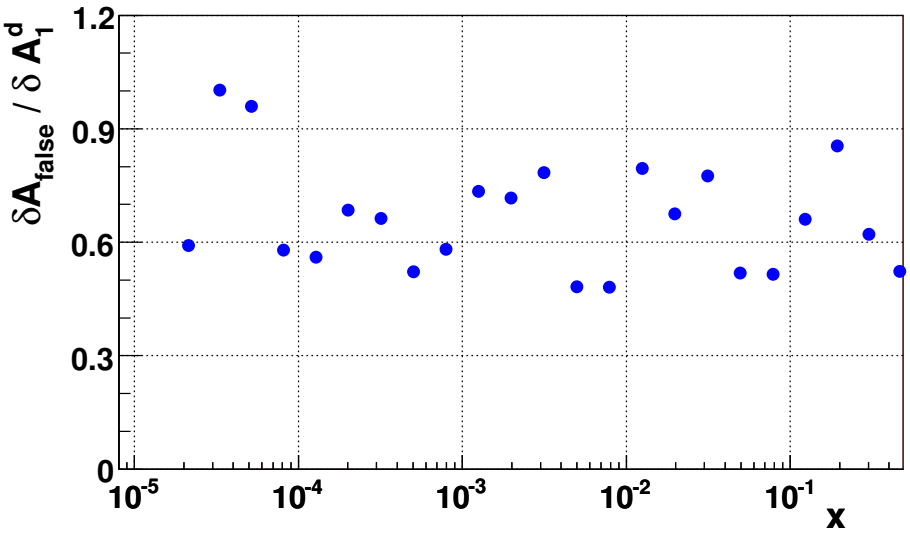

Figure 5.28: The 95%CL limit as a function of $\delta A_1(x)$ for the false asymmetries in the data. Results were obtained using the method discussed in section 5.6.2.

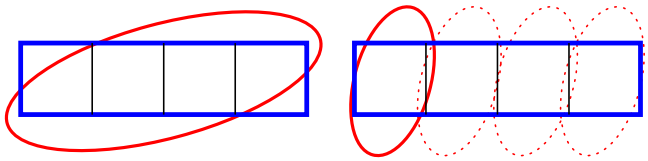

Figure 5.29: Data combining for the stability test of different methods of asymmetry extraction. See text for details.

5.7 Other systematic studies

5.7.1 Different methods of asymmetry measurement

In section 5.4 different methods of the asymmetry extraction were discussed. Here their stability is considered.

The stability was checked using virtual target setups; a way of combining the data is shown in figure 5.29. For each extraction method the data from the whole upstream cell were combined with each quarter of the downstream target. In total, 16 different asymmetries were measured. Note that they are largely correlated.

Combining the data from the whole upstream target cell with only a quarter of the downstream cell creates a large difference in the acceptance and in statistics. From section A.2 it follows that a large imbalance of the acceptance introduces a bias for the first order methods. For the second order methods such an acceptance imbalance should not matter.

Values of the obtained asymmetries are given in table 5.10. The results from part of 2003 data are presented. In the first column the asymmetry method is given. Next four columns are the results for the asymmetry computed using different quarters of the downstream cell. Finally, in the last column the results from the combination of the whole upstream and the whole downstream cells are given – a standard A_1^d measurement. The results were averaged over $x \in (10^{-5} - 10^{-2})$ and multiplied by 10^3. The errors of the measurements are about $(1.5 - 2) \cdot 10^{-3}$.

	1st part	2nd part	3rd part	4th part	total
1st order $w = 1$	0.2	1.0	-0.2	-1.0	0.0
1st order $w = fDP_b$	-5.1	-2.1	-3.2	-6.5	**+1.9**
2nd order $w = 1$	0.2	1.3	-0.3	-1.4	0.0
2nd order $w = fDP_b$	0.8	3.0	1.2	-2.0	0.8

Table 5.10: Comparison between different methods of the asymmetry extraction. Four parts refer to four quarters of the downstream target cell. Asymmetries multiplied by 10^3 are presented.

Results of the 2nd order methods and the 1st order non-weighted method are similar. Unfortunately the 1st order weighted method seems to be unstable. The results for quarters of the downstream cell are completely inconsistent with the result for the whole downstream target. Note, that even the sign of the asymmetry has changed! Indeed a bias of the asymmetry was expected but both 1st order methods were supposed to be affected in the

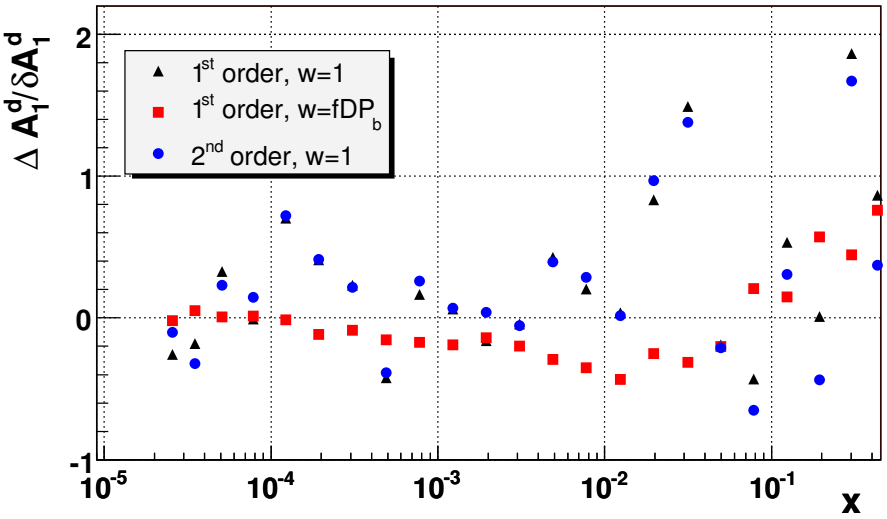

Figure 5.30: Comparison between different methods of the asymmetry extraction. The reference method is 2nd order weighted method. The difference between it and other methods divided by its statistical error is shown.

same way. As the 1st order methods were only used for consistency checks there were no extended studies of the observed phenomenon. One should remember that in the 1st order non-weighted method the asymmetry is computed using an observed event number. In such a case it is impossible to get all negative asymmetries for quarters of the target cell and then a positive one for the whole cell. The situation is different for the 1st order weighted method. The asymmetry measurement depends on two quantities: $\sum w$ and $\sum w^2$. These two, although correlated, are also partly independent from each other, thus may vary in slightly different ways. This partial independence is enough to create the situation seen in the data. Instabilities should not be seen if in the 1st order weighted method the counting asymmetry is modified as *e.g.* in section A.2.

The stability of different methods of the asymmetry extraction were checked on the final data sample too. As a reference the 2nd order weighted method was used. A difference between A_1^d obtained by it and other methods divided by A_1^d statistical error is shown in figure 5.30. The asymmetry bias for the 1st order non-weighted method is visible. It is less pronounced compared to results in table 5.10 as the acceptance ratio between the target cells is closer to one. Difference between non-weighted methods is rather small. In some cases difference between the 2nd order weighted method and non-weighted methods is larger than the statistical error of the asymmetry. Note that exactly the same data is used in all cases. The estimator of the standard deviation for the presented results is not known. Therefore, it was impossible to judge if the observed effect is just a statistical fluctuation or if it indicates a serious systematic problem.

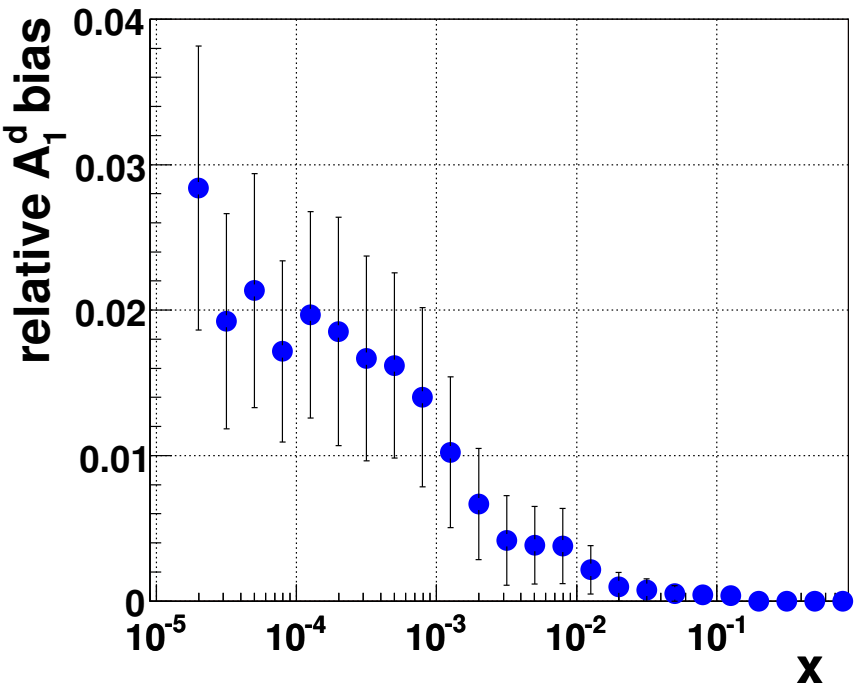

Figure 5.31: The relative asymmetry bias due to the vertex migration.

5.7.2 Vertex smearing

A typical vertex resolution along the beam axis was shown in figure 5.4. A finite vertex resolution will dilute the measured asymmetry in two ways: events may migrate between the target cells and from the outside to the inside of the polarized target. The former way of diluting the asymmetry is more dangerous as the asymmetry bias is doubled compared to the latter case.

Event migration was studied using the PYTHIA sample. Around 500k events were generated and 275k events passed the selection criteria similar to those for the real sample selection, cf. section 5.2.

As the $\delta PV_{x,y}$ are very small, cf. section 5.2.2, only the migration along the beam axis was studied. The interaction vertices were generated only inside target cells. The possibility of the vertex migration to the target cells from the outside was introduced by the author. This was done in an approximate way.

Results are shown in figure 5.31. The asymmetry bias is small, up to 2-3% for the lowest x values. Note that the vertex selection criteria were chosen to reduce the migration, cf. section 5.2.2. For the five highest x intervals the MC statistics was too small to measure the asymmetry bias precisely. Nevertheless, judging from measurement at lower x, the migration is expected to be negligible for $x > 0.1$. The estimated error of the bias was taken as a combination of the statistical accuracy and the difference between the results obtained with the migration from outside sources switched on or off.

The measured asymmetry should be corrected for the vertex migration effect; It was included in the systematic error. Compared to other sources of the systematic uncertainty, *e.g.* R, false asymmetries, *etc.* the effect of the vertex migration is completely negligible in

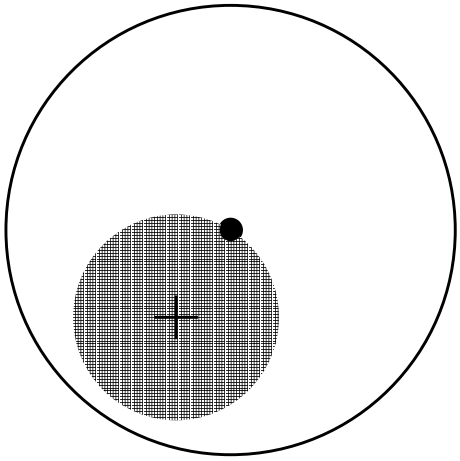

Figure 5.32: Source of $< x >$ bias: small angle scattering. See text for details.

the whole x range, cf. section 5.8.

5.7.3 The $< x >$ bias

In COMPASS the measured x value is directly connected to Q^2. For any ν and neglecting the non-zero muon mass Q^2 depends upon the angle θ between the incident and the scattered muon, $Q^2 \sim sin^2\frac{\theta}{2}$. Since $< sin^2\frac{\theta}{2} > \neq < sin\frac{\theta}{2} >^2$, in case of small scattering angles a bias on the measured angle value and thus Q^2 and x is introduced. The idea is sketched in figure 5.32. The cross denotes the θ=0 scattering. The black dot is the θ angle between the incident and the scattered muon, while the large circle centred at the dot is the precision of this measurement. The shadowed area centred at the cross shows the region where the measured Q^2 would be smaller than the real value. In remaining area the measured Q^2 is larger than the true value. The probability that the measured Q^2 is larger than the true one is higher than the opposite possibility thus the bias is introduced.

Studies of the $< x >$ bias were made using the MC technique. The same PYTHIA event sample as in section 5.7.2 was used. Results are presented in figure 5.33. The left plot shows the mean value of the $(x_{rec} - x_{gen})/x_{gen}$ as a function of x_{gen}, where x_{gen} is generated in the MC program and x_{rec} is the reconstructed value. As expected at low x the bias is large. The right plot $(x_{rec} - x_{gen})/x_{gen}$ as a function of x_{rec} might be somewhat surprising. For a moderate x range the bias behaviour is as expected, *i.e.* is larger for smaller x and the maximum of 5% is reached. For the lowest x the bias changes its sign. A reason for this behaviour is the following: the x distributions have sharp edges due to the acceptance. It is very unlikely that an event with a very low x appears, most likely the event had a larger x but accidentally a smaller x value was reconstructed. The same explanation is valid for the highest x point.

It is worth mentioning that the size of the effect, $\sim$ 5%, for $x \sim 10^{-4}$ was obtained after weighting the events, cf. section A.4. Using only events numbers the effect would be around 10%, so twice as large. To explain the difference between the two results let us note that of all factors in $w = fDP_b$ only depolarization, D, can play a non-negligible role here. High D means high y and small energy of the scattered muon, E'. Let us consider

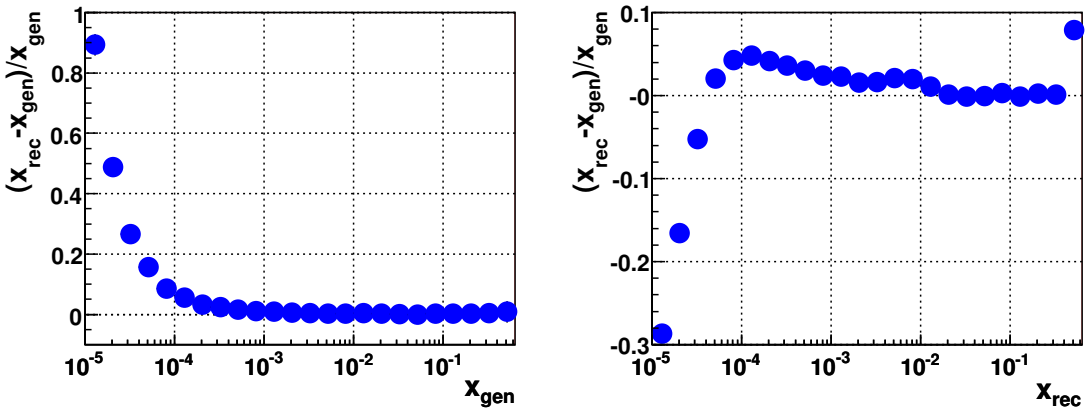

Figure 5.33: Reconstruction of x in MC; left: the $< x >$ bias as a function of x generated; right: the same but for the reconstructed x.

the formula:

$$x = Q^2/2M\nu \approx \frac{4EE'}{2M(E-E')} sin^2\frac{\theta}{2} \tag{5.15}$$

To obtain the same x value for small E' (*i.e.* large D and therefore large weight) the θ angle has to be larger. For a larger angle the expected bias on $< sin^2\frac{\theta}{2} >$ measurement is smaller. This is why event weighting reduces the observed bias. The reduction of the bias is not seen in the smallest x region as a different mechanism plays a key role there.

5.7.4 Precision of the x measurement

The results of the A_1^d and g_1^d measurement will be presented in a way that one decade of x is divided into five, equal size[10], intervals. Precision of x measurement decreases with decreasing of x. The reason is that for low x, means low Q^2, a muon is scattered at small angle, which is hard to measure. It was interesting to check the magnitude of that smearing in view of the above choice of x intervals.

The same MC sample was used as in section 5.7.2. In figure 5.34 two variables are shown; left: $\delta x/x$, right: probability that reconstructed and generated x were found in the same x interval. As expected the lower x the observed x smearing is larger and a migration of events between bins increases. For the lowest x the migration exceeds 50%.

5.7.5 Target position and target movements

The knowledge of the relative position of the target with respect to the spectrometer is crucial, as interesting events occur only inside the polarized material. A position of the reconstructed vertex was investigated in the region of the target holder. In that region there is no polarized material and therefore the holder was clearly seen. In figure 5.35 distribution of PV_x versus PV_y for different PV_z is shown. The PV_z of the verticies were the following: top-left $PV_z \in (-100, -85)$, top-right $PV_z \in (-55, -40)$, bottom-left $PV_z \in (-30, -15)$,

[10]In logarithmic scale.

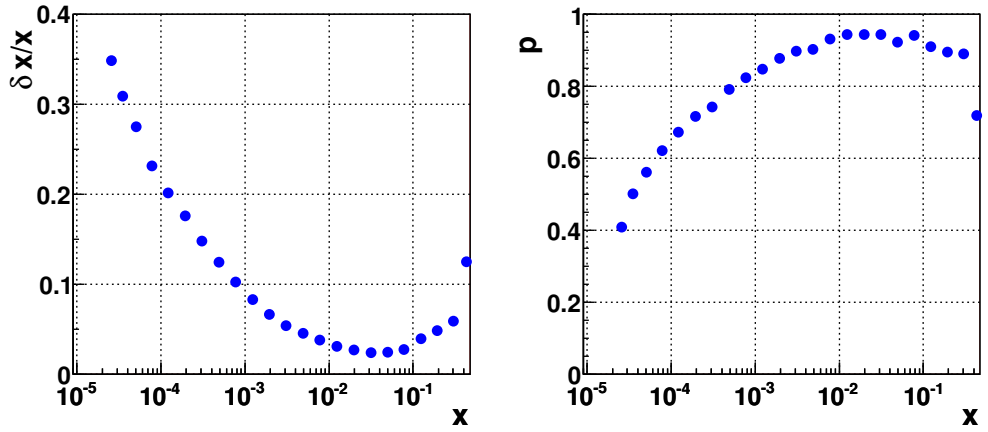

Figure 5.34: x reconstruction in MC; left: $\delta x/x$, right: probability that x is reconstructed in the same interval as it was generated.

bottom-right $PV_z \in (15, 30)$. The oval structure which in the top-left plot has a maximum at $y = 1.45$ cm is the target holder. Knowing the position of the upper part of the target holder and the target radius the position of the centre of the target can be calculated. As the PV_z increases the target holder moves down wards which indicates that the target is tilted. Another method used in COMPASS for the target position measurements was a two dimensional fit of a circle to the vertex coordinates distribution. The position of the target was given in table 5.1.

The target moves in the up-down direction when the solenoid current is reversed. The effect is due to interference between SM1 and solenoid magnetic fields. The movement of the target was measured by fitting the position of the target holder and various other items attached to the target (screws, wires), cf. figure 5.36. Twelve different points at different 'z' values were measured. Results for all the points are consistent and show that the end of the target moves by more than 600 μm during the current reversion, cf. figure 5.37. The target position in the data analysis is corrected for the observed effect, cf. section 5.2.2. Such a big target movement came as surprise. The whole solenoid moves by about 600 μm [11] while the length of the target is three times smaller than the solenoid's. It was shown [127] that due to a target support the target movement can indeed be as large as that of the whole solenoid.

The observed position of the target changes in time. Origin of these movements is the alignment stability with respect to the global coordinate system. The observed shifts during a year are of the order of 500 μm. The target position is not corrected for those shifts. The main reason is that every data (re-)production may result in a new target position. It is more convenient to have only one position for the whole year.

[11] There were special measurements as well as results of the FI03 movement observed during the alignment procedure, see section 4.7.3.

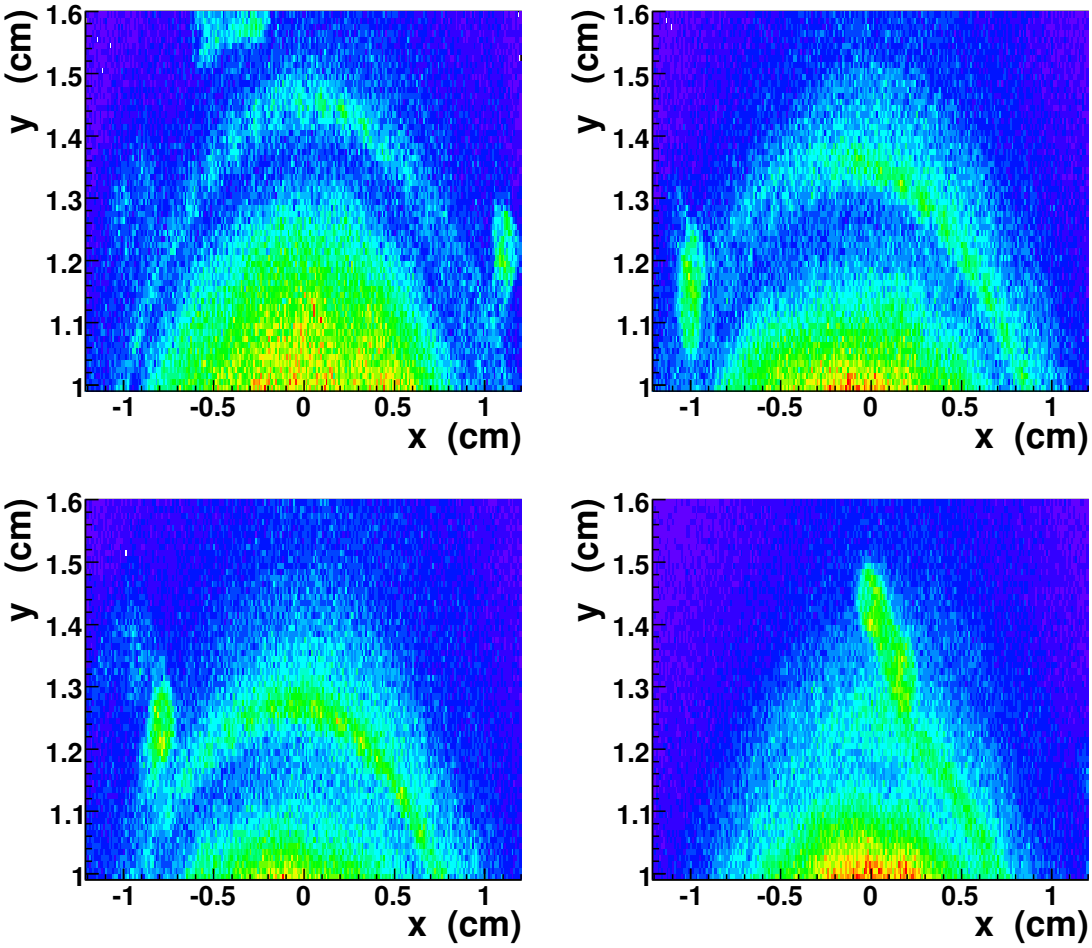

Figure 5.35: The primary vertex distribution for different 'z'. See text for details.

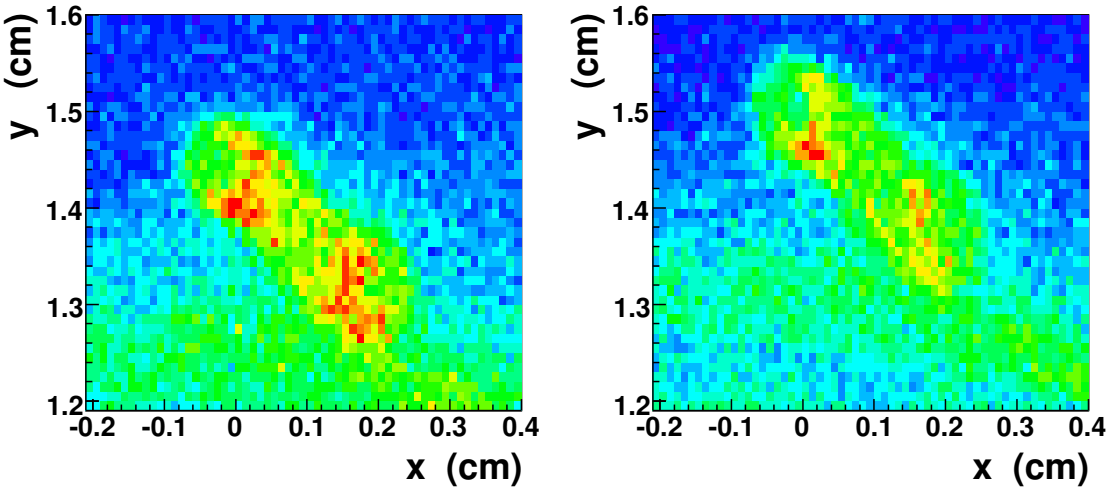

Figure 5.36: Vertex distributions for two different solenoid currents. S movement of a screw attached to the target and seen as an oval is visible.

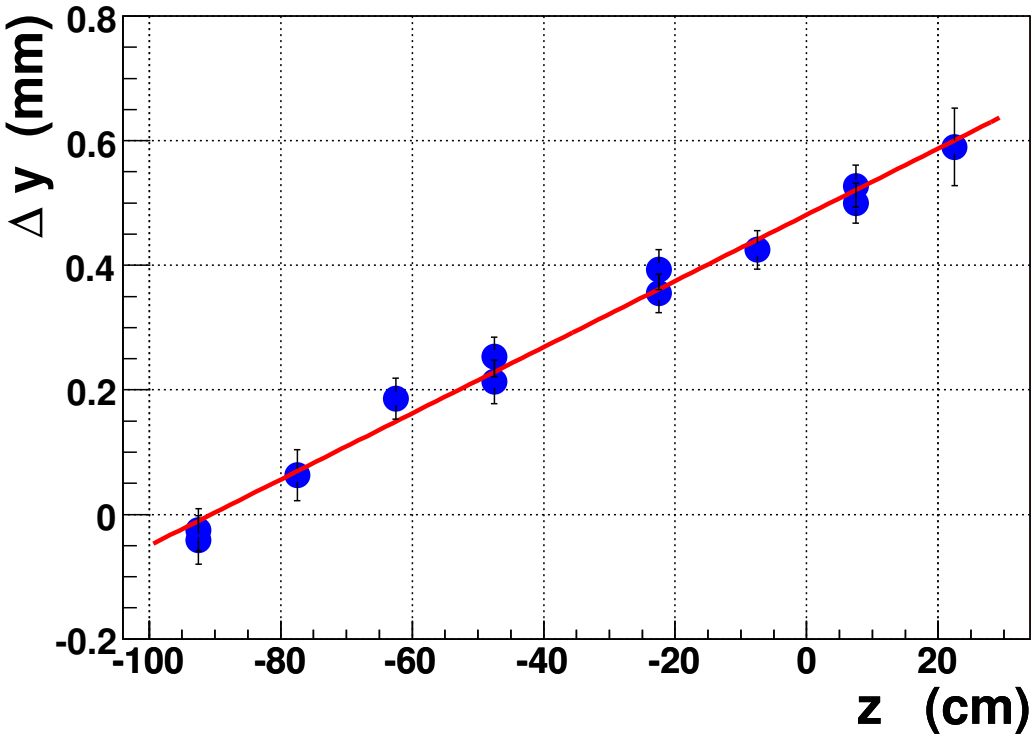

Figure 5.37: Measured target position shift caused by the solenoid field reversal for different z positions.

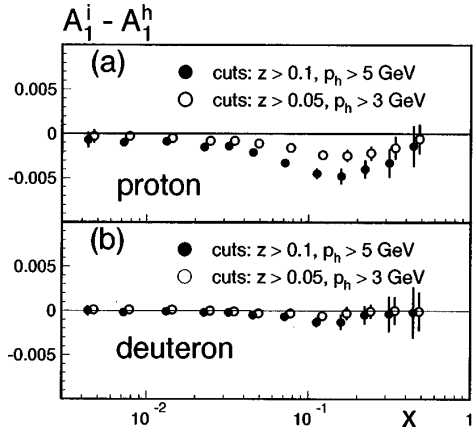

Figure 5.38: The SMC results for the hadron method bias [11]. A_1^i and A_1^h denote the A_1 asymmetries for inclusive and hadron tagged data samples, respectively.

5.7.6 The hadron method bias

In this analysis a presence of at least one hadron in the PV was required. At this point let us consider the u, d quark fragmentation in the μd reaction. The u, d quarks have different electric charges, +2/3 and -1/3, respectively. Thus the u has larger probability to fragment into a positive particle than d into a negative one. Only charged particles leaving the PV are detected. As the fragmentation probabilities into charged particles for the u, d quarks are different, the measured asymmetry using the hadron method is biased.

The above mentioned effect was studied already in the SMC [11]. The difference between the inclusive asymmetry and the asymmetry obtained using the hadron method was measured, see figure 5.38. The observed bias was found to be small for the deuteron. The SMC analysis for the deuteron was repeated in COMPASS [128] and the conclusion was identical. The possible bias due to hadron method was neglected in this analysis.

5.7.7 Bias due to A_2

During the A_1^d computation the factor ηA_2 was neglected, cf. equations (2.25). The systematic error connected to the A_2 asymmetry was estimated in the same way as in [56]: the ηA_2 was not neglected and A_2 was supposed to be equal to 0.05 for the whole x range but for $x > 0.4$ where $A_2 = 0.1$. The bias is defined as a difference between A_1^d obtained with or without the ηA_2 therm. Results are shown in figure 5.39; left: the estimated bias, right: the bias divided by the statistical error of the A_1^d asymmetry. In the interesting low x domain, the bias is small but not negligible compared to the statistical error of A_1^d. It was taken into account in the systematic uncertainty of A_1^d. A similar bias is introduced when g_1^d is extracted. The term γA_2 is neglected then. This bias is comparable with the one discussed above also here it was taken into account in the g_1^d systematic error.

5.7.8 Systematic effect in g_1^d extraction

For g_1^d, as compared to A_1^d measurements, there is one additional source of the systematic uncertainty: a precision of the F_2 structure function measurement. This was already

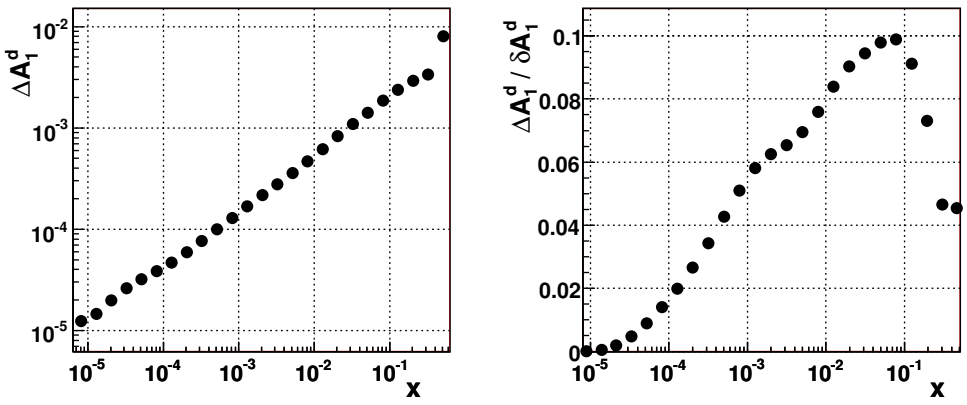

Figure 5.39: The estimate of A_1^d bias, ΔA_1^d, introduced due to the neglected term ηA_2 in the A_1^d extraction. The δA_1^d is the statistical error on A_1^d.

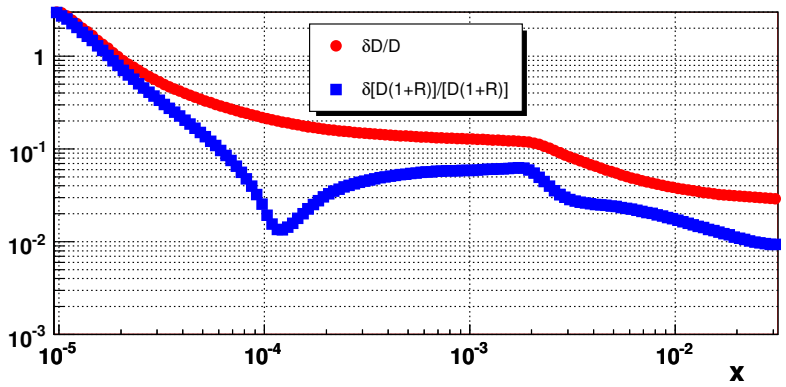

Figure 5.40: Uncertainty of depolarization factor for D and $D(1+R)$.

discussed in section 5.3.6. Here two other possible systematic effects are discussed: the depolarization factor and the weight in case of g_1 extraction.

The depolarization factor

The depolarization factor, D, was discussed in 5.3.3. The error of the depolarization factor was shown in figure 5.9. This error is associated with the R function uncertainty, cf. section 5.3.2.

In the g_1^d extraction R appears in the denominator of equation (2.25). Thus instead of the error of the depolarization factor, one has to estimate the $D(1+R)$ uncertainty. This estimate is shown in figure 5.40. Almost in the whole x range, $D(1+R)$ is much less sensitive to the uncertainty of R than to that of D. This was expected as the $(1+R)$ factor cancels partially with the $(1+R)$ factor, in the denominator of D, equation (5.2). Still, at low x the $\delta D(1+R)$ plays an important role.

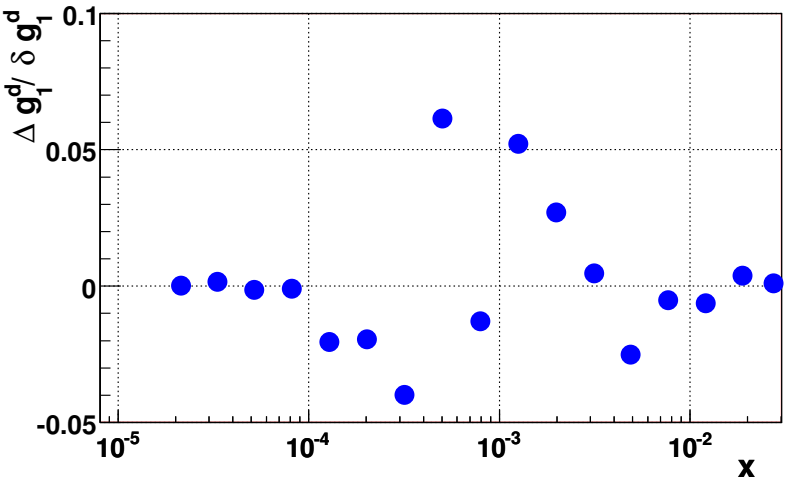

Figure 5.41: A difference between the g_1^d obtained using different weight divided by the statistical error g_1^d.

The weight for the g_1^d measurement

The weight used for the A_1^d extraction is $w = fDP_b$. When g_1^d is extracted from A_1^d the latter is divided by $(1+R)$ [12] where R is calculated for the averaged x and Q^2. Instead of such a procedure one can modify the weight, $w_{g1} = fDP_b(1+R)$. In fact, the modification is necessary: if two quantities were correlated and only one of them was included in a weight than the measured asymmetry would be biased, [129]. Here the correlated variables are D and R.

Results for the g_1^d structure function using both weights were compared. The difference of the two, Δg_1^d, divided by the g_1^d statistical error is shown in figure 5.41. The bias was found to be small in the whole x range but comparable to the P_t P_b and f uncertainties.

5.7.9 Consecutive versus global configuration

The data sample used for A_1^d measurement contains almost 300 million events. Data are divided into approximately 100 configurations the so called *consecutive configuration*. On average, in each configuration there are around 3 million events. COMPASS has different analyses, where the whole data sample contains only a few thousand events. It is not correct to divide such a small data sample in many configurations. Usually, for these analyses the data from a certain data taking period are combined together. This type of data combining is called "global configuration" One period is typically one week of data taking. During this time the experimental area is supposed to be closed, which means that quality of the data collected during the week should not change. In practice, a possible access to the experimental zone and an equipment failure may influence the data quality. It was checked how large systematic difference is observed for the data combined configuration-by-configuration and period-by-period. This can give an estimate of systematic effects in

[12] For the discussed case $F_2/2x$ factor in equation (2.25) is irrelevant.

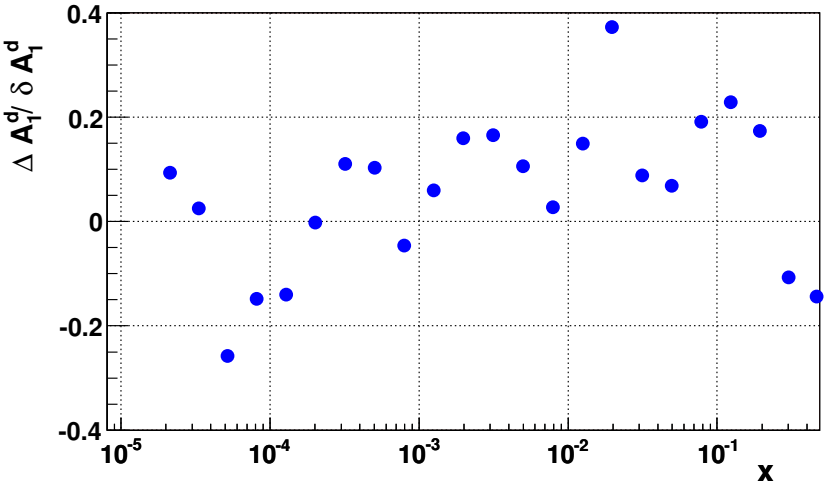

Figure 5.42: A difference between A_1^d obtained from the global and the consecutive configurations divided by the statistical error of A_1^d.

the analyses with limited data samples. Results are shown in figure 5.42 where a difference between A_1^d obtained from the two methods of the data combining divided by the statistical error of the A_1^d measurement is given. The difference between the methods is of the order of one fifth of the statistical error. No significant asymmetry bias is observed.

5.7.10 Weights and systematic effects

In this section we discuss systematic effects connected to usage of weighted methods for the asymmetry extraction. Two effects were already mentioned: an event weight must not contain a variable which changes in time (thus *e.g.* the P_t is excluded from the weight) and a weight should not contain a variable correlated with another one which is not included (thus a redefinition of the weight in the g_1^d extraction).

One of the effects which was not mentioned up to now is the error of the weight. From the statistics point of view, the weighted methods are correct only if we know the weight and not just an estimator of it. Unfortunately, in experiments we only have estimators. In the case of the depolarization factor at low x, the estimate is poorly known. Using only an estimator of a weight may introduce a bias and definitely increases the systematic error. This effect was not included in the systematic studies since there is no known methods of doing it.

The next effect, which is partially connected to the one discussed above, is the impact of $\delta D/D$, $\delta f/f$, $\delta P_b/P_b$, $\delta P_t/P_t$ and $\delta F_2/F_2$ on the systematic uncertainty of A_1^d in the case of a very small measured A_1^d value. For the non-weighted methods, cf. equation (A.21), the δA_1 is always proportional to $\delta D/D, etc.$ In the case of the weighted methods the situation is different. If the measured asymmetry is small, changing the weight may even change the sign of the asymmetry. For such cases the A_1^d error is not proportional to $\delta D/D$, *etc.*

To estimate the size of the effects the function R was changed: instead of R, the $R+\delta R$ was used as an input to the depolarization factor. Then the $A^d_{1,R+\delta R}$ asymmetry was ex-

tracted. The results were compared with the standard A_1^d measurement. The procedure was repeated twice for the weighted and non-weighted methods of the asymmetry extraction. A relative change of A_1^d may be directly compared to $\delta D/D$. Results are shown in figure 5.43 where the case of weighted and non-weighted methods of asymmetry extraction are presented in upper and lower plots respectively. Clearly, some of the points do

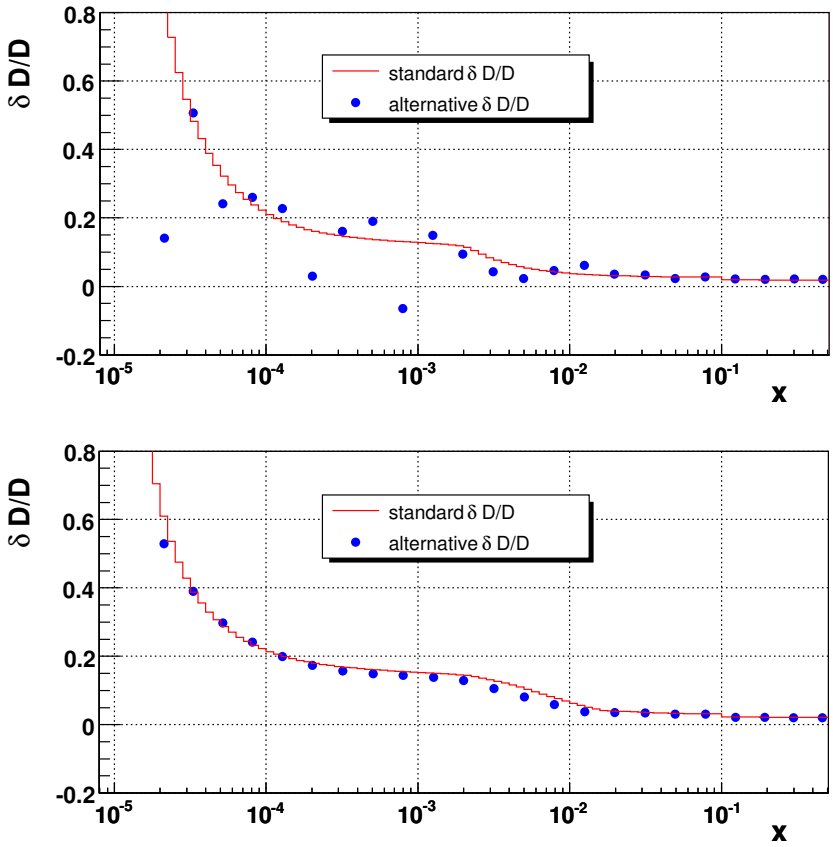

Figure 5.43: Comparison of different ways of the systematic error estimation for different methods of the asymmetry extraction; upper: weighted method, lower: non-weighted method.

not follow the $\delta D/D$ curve for the weighted method. The situation is better for the non-weighted one, where differences between the curve and the points are small. The values of $\delta A_1^d/A_1^d$ were checked for the points where there was a large deviation between them and the expected curve. Results are summarized in table 5.11. One can conclude that in most of cases the $\delta A_1^d/A_1^d$ is not proportional to $\delta D/D$ for rather small $A_1^d/\delta\ A_1^d$ values as it was expected[13]. The described effect was not taken into account during the systematic error computations as it has negligible impact on the final systematic error which is dominated by false asymmetries.

[13]For technical reasons the asymmetries were checked for the "global" configuration and not for the "consecutive" one. Therefore these results do not coincide with the final results presented in section 6.1.

x	$A_1^d/\delta A_1^d$
$2 \cdot 10^{-5}$	-0.15
$2 \cdot 10^{-4}$	-0.27
$8 \cdot 10^{-4}$	-0.11

Table 5.11: $A_1^d/\delta A_1^d$ for the cases, where large differences were observed between the different methods of the $\delta D/D$ estimate, cf. figure 5.43.

5.7.11 The μe data sample

In section 5.2.3 a method of rejecting events from the muon–atomic electron elastic scattering was shown. These events belong to the background but they may be useful for systematic studies. Pure μe was selected using the cut: $-0.002 < q\theta < 0.000$, see section 5.2.3. Selected sample contained $2.3 \cdot 10^7$ events and purity about 98%. The expected asymmetry for the μe sample is 0.0 as free electrons in target cells are all polarized in the same direction. However, these events are very sensitive to acceptance changes as all the particles in the final state have to be reconstructed. The electron is usually emitted at a small angle. This makes the PV reconstruction harder, thus even more bias prone. The μe data sample has one limitation: all events are concentrated around $x \sim 5.5 \cdot 10^{-4}$.

The asymmetry measured for this sample was indeed found to be consistent with zero. The agreement was better than $1.5\,\sigma$. This is a proof that COMPASS can measure raw asymmetries with a precision of about $1/\sqrt{2 \cdot 10^7} \approx 2 \cdot 10^{-4}$ without a mean value bias. Let us consider the distribution of pulls, cf. 5.6. Its standard deviation was found to be equal to 1.50 ± 0.07, inconsistent with 1.0. The inconsistency is a sign of a systematic bias. To estimate it the method described in section 5.6.2 was used. The 95% CL limit is $1.4\,\sigma_{stat}$, thus larger than the statistical error itself.

A raw asymmetry error obtained from the μe sample is about $2 \cdot 10^{-4}$. For the average $fDP_bP_t = 0.07$ it leads to the A_1^d asymmetry error about $3 \cdot 10^{-3}$. As it will be shown in section 6.1, the statistical error of the A_1^d measurement in COMPASS is as small as $2 \cdot 10^{-3}$. This means that the precision of the A_1^d measurement came close to the limit where the systematic effects play the most important role. The situation is not critical though. It was mentioned that the μe events are very sensitive to systematic effects, much more so than typical events used for the A_1^d measurements. Moreover, the correct asymmetry value, *i.e.* 0, was found. Therefore it is realistic that the data collected by COMPASS in 2004 and 2006 will further decrease the A_1^d uncertainty.

5.8 Summary of the systematic studies

In this section a summary of all the factors which were included in the A_1^d systematic error is given. The method which was used for the final systematic error computation is presented and discussed. Finally relative contributions of different uncertainties to the total systematic error are shown.

5.8.1 Summary of systematic effects

The following contributions to the total systematic error of the A_1^d and g_1^d measurements were included:

- δP_b - beam polarization
- δP_t - target polarization
- δD - depolarization factor
- δf - dilution factor
- δA_2 - A_2 asymmetry neglection
- δF_2- structure function F_2
- δVtx - vertex migration
- δele - radiative events with converted photons
- δRC - polarized radiative corrections
- δA_{false} - false asymmetries

For the first four quantities their relative error $\delta X/X$ is proportional to $\delta A_1^d/A_1^d$. The beam polarization uncertainty, $\delta P_b/P_b$, was set to 4%. The uncertainty of the target polarization, $\delta P_b/P_b = 5\%$. These numbers were chosen identical with [56]. For the $\delta D/D$ and $\delta f/f$ the x dependence of the error has been taken into account. The results were presented in sections: 5.3.3 and 5.3.5. The error of the dilution factor is 6-8%, while the uncertainty of D due to the unknown R function exceeds 100% for the lowest measured x. The $\delta D/D$ may thus be one of the dominant factors in the low x domain. Possible systematic effects due to the neglecting of A_2 were found to be small, as expected, cf. section 5.7.7. The F_2 systematic error was discussed in section 5.3.6; it does not exceed 20%. The contribution from the vertex migration and the radiative events with converted photons is small and it was discussed in sections 5.7.2 and 5.2.3. For both cases the error does not exceed 2%. The uncertainty of the polarized radiative corrections was also taken in to account, cf. section 5.3.4, but was small compared to other systematic sources.

Finally, the last contribution included in the systematic error is the 95% CL limit for the false asymmetries. This item was extensively discussed in section 5.6.3. The estimated limit is proportional to the statistical error of the A_1^d and was the largest contribution to the systematic error of A_1^d in the whole x range.

5.8.2 The systematic error estimate

All the systematic effects discussed in the previous section were combined together in order to get the final error estimate. The formula which was used is:

$$\delta A_{1,\,sys}^d = \left[\left(A_1^d\right)^2 \left(\left(\frac{\delta P_b}{P_b}\right)^2 + \left(\frac{\delta P_t}{P_t}\right)^2 + \left(\frac{\delta f}{f}\right)^2 + \left(\frac{\delta D}{D}\right)^2 \right) + (\delta A_2)^2 + (\delta Vtx)^2 + (\delta ele)^2 + (\delta RC)^2 + (\delta A_{false})^2 \right]^{\frac{1}{2}} \tag{5.16}$$

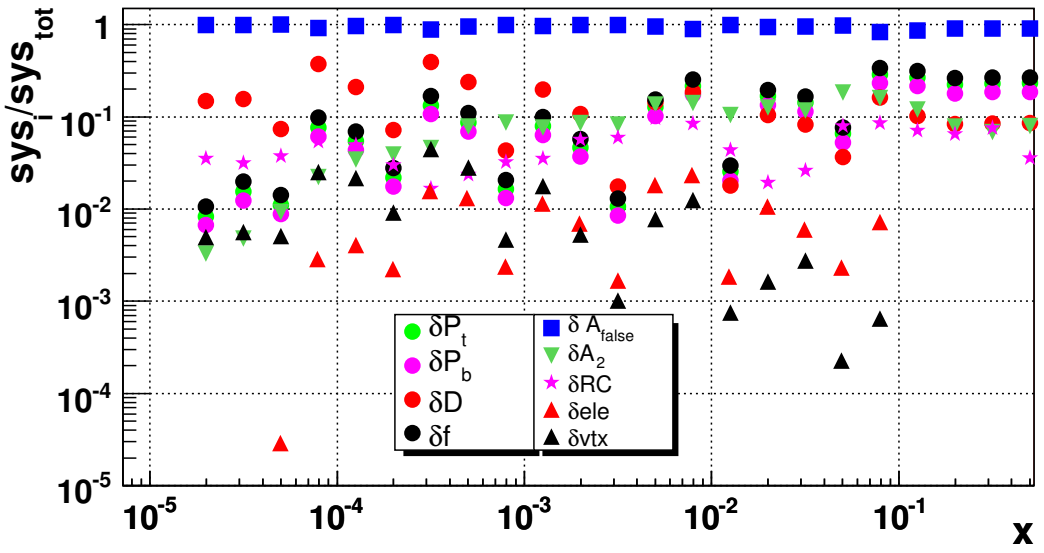

Figure 5.44: The contribution of different sources of systematic uncertainties normalized to the total systematic error.

A similar formula was used to obtain the g_1^d error except that contribution from F_2 was taken into account, $(A_1^d)^2(\delta F_2/F_2)^2$ and that the depolarization factor error was taken as $\delta D(1+R)/D(1+R)$, cf. section 5.7.8.

All the errors in equation (5.16) were added in quadrature. For factors like δF_2 and δA_{false}, such a procedure is incorrect from the statistical point of view as δF_2 and δA_{false} are not errors *per se*. A more correct way would be to divide the systematic error in a few parts but this would be very inconvenient for the later use of these results and therefore it was not done.

In figure 5.44 all relative contributions of different uncertainties to the total systematic error on A_1^d are shown. Each contribution is divided by the final systematic uncertainty. Note that even if the contribution of the given effect is as large as 20% the estimate of the systematic error after excluding this input would change only by $1-\sqrt{1-0.2^2} \approx 2\%$. To conclude: the only important factor which contribute to the final systematic error is: δA_{false}.

Chapter 6

Results

In this chapter we present the final results of the analysis. The data come from the x interval $1.6 \cdot 10^{-5} - 0.6$ and Q^2 interval $(10^{-3} - 100)$ GeV^2. They explore almost one order of magnitude into the unmeasured x interval. For $x \in (10^{-4} - 2 \cdot 10^{-3})$ previously measured by the SMC [19] the statistical precision has increased ten times.

Results of the measurement of the spin dependent cross section asymmetry A_1^d and of the spin dependent structure function g_1^d are presented at the beginning of this chapter. Both statistical and systematic errors are given. A breakup of the systematic uncertainties into different sources, discussed in section 5.8, is given as well. The presented results are compared to other experiments. Finally, results are confronted with the Regge model predictions.

6.1 A_1^d spin asymmetry

6.1.1 The A_1^d results

The results for the spin dependent cross section asymmetry A_1^d are given in table 6.1 and in figure 6.1. In the first column of the table the intervals of x in which the asymmetry was measured are shown. Then $< x >$, $< Q^2 >$ and $< y >$ are given. Finally in the last column the A_1^d results are presented. The first number indicates the measured A_1^d asymmetry, the second is the statistical error and the third is an estimate of the systematic uncertainty.

No significant spin effects are observed at low x. The obtained results are consistent with zero for $x < 0.01$.

6.1.2 The A_1^d systematic error

Estimates of the systematic uncertainties are given in table 6.1 and in figure 6.1. They were calculated according to the equation (5.16). In table 6.2 contributions to the total systematic uncertainty from different sources are presented. The x interval and total systematic uncertainty of the A_1^d measurement, $\delta A_{1,sys}^d$ are given in the first two columns, respectively. They are followed by systematic errors associated with different sources, see section 5.8. As it was discussed there the largest contribution comes from the false asymmetries.

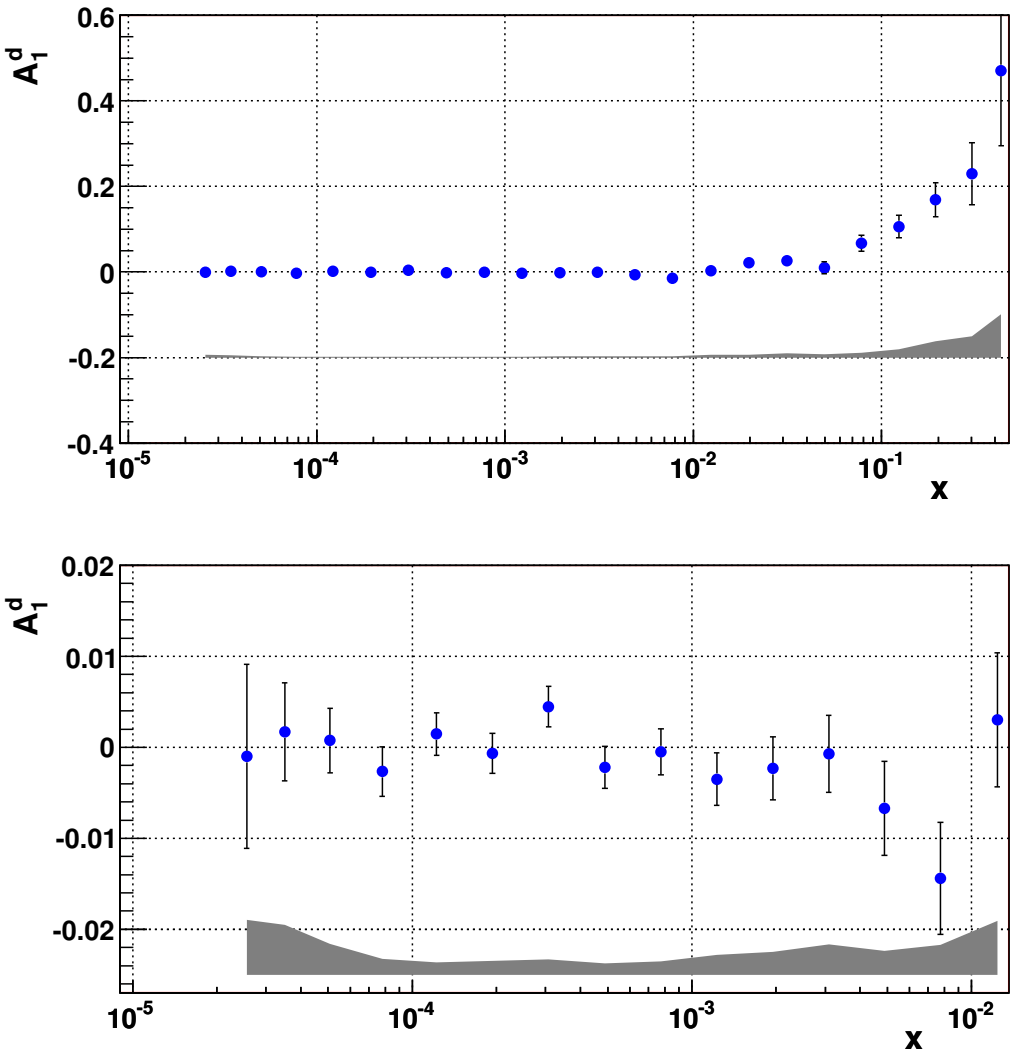

Figure 6.1: Results of this A_1^d measurement; top: A_1^d in the whole measured x range, bottom: zoom of the low x range. In both figures the error bars mark statistical errors, the shaded band indicates the systematic ones.

log10(x)	$< x >$	$< Q^2 >$	$< y >$	A_1^d
-4.8 – -4.6	0.000026	0.0024	0.32	-0.001 ± 0.010 ± 0.006
-4.6 – -4.4	0.000035	0.0040	0.38	0.0017 ± 0.0054 ± 0.0055
-4.4 – -4.2	0.000051	0.0067	0.44	0.0007 ± 0.0036 ± 0.0034
-4.2 – -4.0	0.000078	0.012	0.49	-0.0027 ± 0.0027 ± 0.0017
-4.0 – -3.8	0.00012	0.020	0.53	0.0015 ± 0.0023 ± 0.0014
-3.8 – -3.6	0.00019	0.032	0.56	-0.0007 ± 0.0022 ± 0.0015
-3.6 – -3.4	0.00031	0.052	0.56	0.0045 ± 0.0022 ± 0.0017
-3.4 – -3.2	0.00049	0.082	0.56	-0.0022 ± 0.0023 ± 0.0013
-3.2 – -3.0	0.00078	0.13	0.55	-0.0005 ± 0.0025 ± 0.0015
-3.0 – -2.8	0.0012	0.20	0.54	-0.0035 ± 0.0029 ± 0.0022
-2.8 – -2.6	0.0020	0.31	0.54	-0.0023 ± 0.0035 ± 0.0025
-2.6 – -2.4	0.0031	0.49	0.53	-0.0007 ± 0.0043 ± 0.0034
-2.4 – -2.2	0.0049	0.77	0.53	-0.0067 ± 0.0052 ± 0.0026
-2.2 – -2.0	0.0077	1.2	0.52	-0.0146 ± 0.0062 ± 0.0033
-2.0 – -1.8	0.012	1.9	0.50	0.0025 ± 0.0074 ± 0.0059
-1.8 – -1.6	0.020	2.8	0.47	0.0209 ± 0.0092 ± 0.0066
-1.6 – -1.4	0.031	4.2	0.45	0.025 ± 0.012 ± 0.009
-1.4 – -1.2	0.050	6.3	0.42	0.007 ± 0.014 ± 0.008
-1.2 – -1.0	0.078	9.2	0.39	0.062 ± 0.019 ± 0.011
-1.0 – -0.8	0.12	14	0.37	0.099 ± 0.026 ± 0.020
-0.8 – -0.6	0.19	22	0.38	0.160 ± 0.040 ± 0.037
-0.6 – -0.4	0.30	36	0.40	0.220 ± 0.073 ± 0.049
-0.4 – -0.2	0.43	53	0.41	0.46 ± 0.18 ± 0.10

Table 6.1: Results of the A_1^d measurement.

6.1.3 The consistency check

As it was mentioned earlier the COMPASS results of A_1^d for $Q^2 > 1$ GeV^2 were already published, [56]. The data sample used in this analysis contains also events for which $Q^2 > 1$ GeV^2 albeit collected by different triggers. Comparison between the two analyses in the overlap region was thus a natural data consistency check.

However, even in the overlapping region the present sample sample is not the same as that of [56]. This is mostly due to the fact that in this analysis at least one hadron was required in the PV. If this were the only difference then the present data sample would be a sub-sample of that in [56]. In that case the correlation factor between the samples would be $\sqrt{n_h/n_{incl}}$, where n_h is the number of events in the present data sample and n_{incl} is the number of events in the data sample in [56]. Now if we consider the asymmetries measured in the two analyses, A_h and A_{incl}, the correlation factor can be rewritten to a form:

$$corr(n_h, n_{incl}) = \sqrt{n_h/n_{incl}} \approx \delta A_{incl}/\delta A_h \tag{6.1}$$

As the correlation factor is known, the error of the difference $A_h - A_{incl}$ can easily be

log10(x)	$\delta A_{1,sys}$	δP_t	δP_b	δD	δf	δA_{false}	δA_2	δRC	δele	δVtx
-4.8 – -4.6	0.0061	0.0001	0.0000	0.0009	0.0001	0.0060	0.0000	0.0002	0.0000	0.0000
-4.6 – -4.4	0.0055	0.0001	0.0001	0.0008	0.0001	0.0054	0.0000	0.0002	0.0000	0.0000
-4.4 – -4.2	0.0034	0.0000	0.0000	0.0002	0.0000	0.0034	0.0000	0.0001	0.0000	0.0000
-4.2 – -4.0	0.0017	0.0001	0.0001	0.0007	0.0002	0.0016	0.0000	0.0001	0.0000	0.0000
-4.0 – -3.8	0.0014	0.0001	0.0001	0.0003	0.0001	0.0013	0.0000	0.0001	0.0000	0.0000
-3.8 – -3.6	0.0015	0.0000	0.0000	0.0001	0.0000	0.0015	0.0001	0.0000	0.0000	0.0000
-3.6 – -3.4	0.0017	0.0002	0.0002	0.0007	0.0003	0.0015	0.0001	0.0000	0.0000	0.0001
-3.4 – -3.2	0.0013	0.0001	0.0001	0.0003	0.0001	0.0012	0.0001	0.0000	0.0000	0.0000
-3.2 – -3.0	0.0015	0.0000	0.0000	0.0001	0.0000	0.0015	0.0001	0.0000	0.0000	0.0000
-3.0 – -2.8	0.0022	0.0002	0.0001	0.0004	0.0002	0.0021	0.0002	0.0001	0.0000	0.0000
-2.8 – -2.6	0.0025	0.0001	0.0001	0.0003	0.0001	0.0025	0.0002	0.0001	0.0000	0.0000
-2.6 – -2.4	0.0034	0.0000	0.0000	0.0001	0.0000	0.0033	0.0003	0.0002	0.0000	0.0000
-2.4 – -2.2	0.0026	0.0003	0.0003	0.0004	0.0004	0.0025	0.0004	0.0003	0.0000	0.0000
-2.2 – -2.0	0.0033	0.0007	0.0006	0.0006	0.0009	0.0030	0.0005	0.0003	0.0001	0.0000
-2.0 – -1.8	0.0059	0.0001	0.0001	0.0001	0.0001	0.0059	0.0006	0.0003	0.0000	0.0000
-1.8 – -1.6	0.0066	0.0010	0.0008	0.0007	0.0012	0.0062	0.0008	0.0001	0.0001	0.0000
-1.6 – -1.4	0.0094	0.0012	0.0010	0.0007	0.0014	0.0090	0.0011	0.0002	0.0001	0.0000
-1.4 – -1.2	0.0077	0.0003	0.0003	0.0002	0.0004	0.0075	0.0014	0.0006	0.0000	0.0000
-1.2 – -1.0	0.011	0.0031	0.0025	0.0017	0.0037	0.0097	0.0019	0.0010	0.0001	0.0000
-1.0 – -0.8	0.020	0.0050	0.0040	0.0019	0.0058	0.017	0.0024	0.0014	-	-
-0.8 – -0.6	0.037	0.0080	0.0064	0.0030	0.0094	0.034	0.0029	0.0025	-	-
-0.6 – -0.4	0.049	0.011	0.0088	0.0040	0.013	0.045	0.0034	0.0037	-	-
-0.4 – -0.2	0.10	0.023	0.019	0.0086	0.027	0.092	0.0080	0.0036	-	-

Table 6.2: Contributions from different sources to the total systematic uncertainty of A_1^d.

obtained:

$$\delta(A_h - A_{incl}) = \sqrt{\delta A_h^2 + \delta A_{incl}^2 - 2corr(n_h, n_{incl})\delta A_h \delta A_{incl}} = \sqrt{\delta A_h^2 - \delta A_{incl}^2} \qquad (6.2)$$

In fact, the data sample n_h used in the analysis was not a sub-sample of the n_{incl}. The reason is that in the data sample used in [56] in the class of events where a hadron was required, the hadron had to have $z_h > 0.2$. This criterium means that the hadron did not come from the so called *target fragmentation region* (corresponds to small values of z_h) but rather from the so called *current fragmentation region* (large z_h). In the presented analysis there was no need to use a $z_h > 0.2$ cut and $z_h > 0.1$ was applied instead. The correlation factor between the two samples had thus to be extracted from the data samples on the event-by-event basis. It was found to be 0.80 ± 0.01. Its x dependence was weak and therefore neglected.

The results of the comparison are shown in figure 6.2. Due to a large difference between the size of the errors for the low and high x the pulls distribution $(A_{incl} - A_h)/\delta(A_{incl} - A_h)$ is shown. The results obtained in the two analyses are consistent with each other. The χ^2 is 16 for 12 degrees of freedom.

The comparison was repeated but this time $z_h > 0.2$ cut was applied in present data sample. The data obtained in this way were a sub-sample of that from [56]. Again the A_1^d results were found to be consistent.

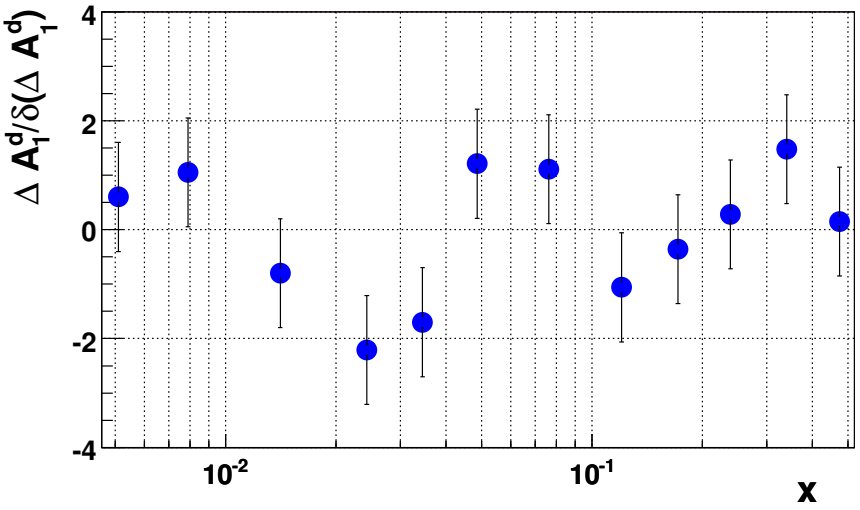

Figure 6.2: Comparison of the A_1^d results obtained in this analysis and in [56]. The pulls distribution $(A_{incl} - A_h)/\delta(A_{incl} - A_h)$ is shown.

6.2 The g_1^d structure function

6.2.1 The g_1^d results

In the past, see *e.g.* [56], the g_1^d structure function was obtained from the A_1^d spin asymmetry by the relation:

$$g_1^d(x, Q^2) \approx F_1(x, Q^2) A_1^d(x, Q^2) \tag{6.3}$$

i.e. equation (2.25), where the contribution from the A_2 spin asymmetry was neglected and F_1 was obtained from:

$$F_1(x, Q^2) = \frac{F_2(x, Q^2)}{2x(1 + R(x, Q^2))} \tag{6.4}$$

In both equations x and Q^2 are the mean values in a given x interval. Extraction of the g_1^d from the formulas above may introduce a bias, cf. section 5.7.8, as the weighted method of the asymmetry extraction was used for the A_1^d measurement. To prevent this the weight for g_1^d extraction was changed into, $w_{g1} = fDP_b(1 + R)$. Using it one measures "an asymmetry" which we denote as: $A^d_{1,(1+R)}$. Then the g_1^d is extracted from:

$$g_1^d(x, Q^2) \approx \frac{F_2(x, Q^2)}{2x} A^d_{1,(1+R)}(x, Q^2) \tag{6.5}$$

here again, x and Q^2 are the mean values in a given x interval.

For the g_1^d measurement the structure function F_2 and the function R, which were discussed in sections 5.3.6 and 5.3.2 respectively, were used. The values of the g_1^d structure function are presented in table 6.3. The table is organized in the same way as the table 6.1 but instead of A_1^d the values of g_1^d are given. The same results are shown in figure 6.3.

log10(x)	$< x >$	$< Q^2 >$	$< y >$	g_1^d
-4.8 – -4.6	0.000026	0.0024	0.32	-0.06 ± 0.57 ± 0.34
-4.6 – -4.4	0.000035	0.0040	0.38	0.11 ± 0.36 ± 0.36
-4.4 – -4.2	0.000051	0.0067	0.44	0.05 ± 0.27 ± 0.26
-4.2 – -4.0	0.000078	0.012	0.49	-0.23 ± 0.23 ± 0.14
-4.0 – -3.8	0.00012	0.020	0.53	0.13 ± 0.21 ± 0.12
-3.8 – -3.6	0.00019	0.032	0.56	-0.06 ± 0.19 ± 0.13
-3.6 – -3.4	0.00031	0.052	0.56	0.37 ± 0.18 ± 0.14
-3.4 – -3.2	0.00049	0.082	0.56	-0.17 ± 0.17 ± 0.09
-3.2 – -3.0	0.00078	0.13	0.55	-0.03 ± 0.16 ± 0.09
-3.0 – -2.8	0.0012	0.20	0.54	-0.11 ± 0.09 ± 0.10
-2.8 – -2.6	0.0020	0.31	0.54	-0.07 ± 0.10 ± 0.08
-2.6 – -2.4	0.0031	0.49	0.53	-0.03 ± 0.10 ± 0.08
-2.4 – -2.2	0.0048	0.62	0.43	-0.11 ± 0.10 ± 0.06
-2.2 – -2.0	0.0075	0.67	0.30	-0.17 ± 0.11 ± 0.09
-2.0 – -1.8	0.012	0.73	0.20	0.08 ± 0.13 ± 0.09
-1.8 – -1.6	0.019	0.81	0.14	0.08 ± 0.20 ± 0.09

Table 6.3: Results of the spin dependent g_1^d structure function; measurements at $Q^2 < 1$ GeV^2.

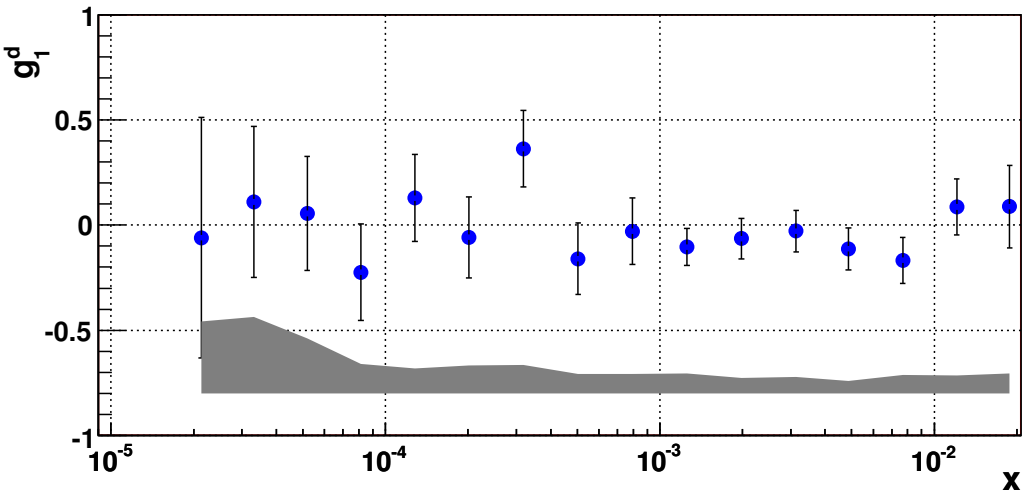

Figure 6.3: Results of the g_1^d measurement at $Q^2 < 1$ GeV^2. The error bars mark statistical errors, the shaded band indicates the systematic ones.

Note that the g_1^d results are shown only for $Q^2 < 1$ GeV^2 thus they are independent from the results published in [56].

6.2.2 The g_1^d systematic error

In table 6.4 the contributions from different sources to the total systematic uncertainty are presented, cf. section 5.8. Systematic studies of A_1^d and g_1^d differ in redefining δD and adding the δF_2 contribution. The main systematic source is the false asymmetry exactly as for A_1^d.

log10(x)	$\delta A_{1,sys}$	δP_t	δP_b	δD	δf	δA_{false}	δA_2	δRC	δele	δF_2	δVtx
-4.8 – -4.6	0.34	0.003	0.003	0.044	0.004	0.34	0.001	0.012	0.000	0.010	0.002
-4.6 – -4.4	0.36	0.005	0.004	0.032	0.007	0.36	0.002	0.012	0.000	0.016	0.002
-4.4 – -4.2	0.26	0.003	0.002	0.007	0.003	0.26	0.002	0.010	0.000	0.008	0.001
-4.2 – -4.0	0.14	0.011	0.009	0.011	0.014	0.13	0.003	0.008	0.000	0.033	0.004
-4.0 – -3.8	0.12	0.007	0.005	0.002	0.008	0.12	0.004	0.006	0.000	0.019	0.003
-3.8 – -3.6	0.13	0.003	0.002	0.002	0.004	0.13	0.005	0.004	0.000	0.008	0.001
-3.6 – -3.4	0.14	0.018	0.015	0.014	0.023	0.12	0.007	0.002	0.002	0.053	0.006
-3.4 – -3.2	0.095	0.008	0.007	0.007	0.011	0.089	0.008	0.002	0.001	0.027	0.003
-3.2 – -3.0	0.094	0.001	0.001	0.001	0.002	0.093	0.009	0.004	0.000	0.004	0.000
-3.0 – -2.8	0.097	0.005	0.004	0.004	0.007	0.067	0.006	0.003	0.001	0.069	0.001
-2.8 – -2.6	0.077	0.003	0.003	0.002	0.004	0.072	0.008	0.005	0.000	0.026	0.000
-2.6 – -2.4	0.081	0.001	0.001	0.000	0.002	0.080	0.008	0.006	0.000	0.007	0.000
-2.4 – -2.2	0.060	0.006	0.004	0.001	0.007	0.053	0.010	0.005	0.000	0.024	0.000
-2.2 – -2.0	0.087	0.009	0.007	0.000	0.010	0.078	0.011	0.003	0.000	0.035	0.000
-2.0 – -1.8	0.086	0.004	0.003	0.000	0.005	0.084	0.012	0.001	0.000	0.014	0.000
-1.8 – -1.6	0.094	0.004	0.003	0.000	0.005	0.092	0.012	0.001	0.000	0.011	0.000

Table 6.4: Contribution from different sources to the total systematic uncertainty of g_1^d.

6.3 Comparison with other experiments

The A_1^d asymmetry and the g_1^d spin structure function have been measured by several other experiments: E143 [13] and E155 [15] at SLAC, HERMES [17] at DESY, SMC [11], [19] and COMPASS [56] at CERN.

The x interval measured by these experiments was $0.0001 - 0.8$. All were (are) fixed-target ones. Therefore the Q^2 values are strongly correlated with the x values. Comparison of results from different experiments is shown in figures 6.4 and 6.5. The values of the A_1^d and the xg_1^d all with statistical errors are presented. For the A_1^d values measured in the experiment are shown. The situation is more complex for the g_1^d. For COMPASS, HERMES and the E155 experiments measured values of the g_1^d are given. The same is for the SMC data from [19]. For the two remaining, the g_1^d values were evolved to a Q_0^2 value common for each experiment, using the DGLAP formalism. In the case of the SMC [11], it was 10 GeV^2 and 3 GeV^2 for the E143. Results presented in this thesis are in agreement with the results from the previous experiments. There is a large reduction of the A_1^d error at low x as compared to the SMC; the only other measurement there. The new measurements confirm that the spin effects at $x < 0.01$ are small.

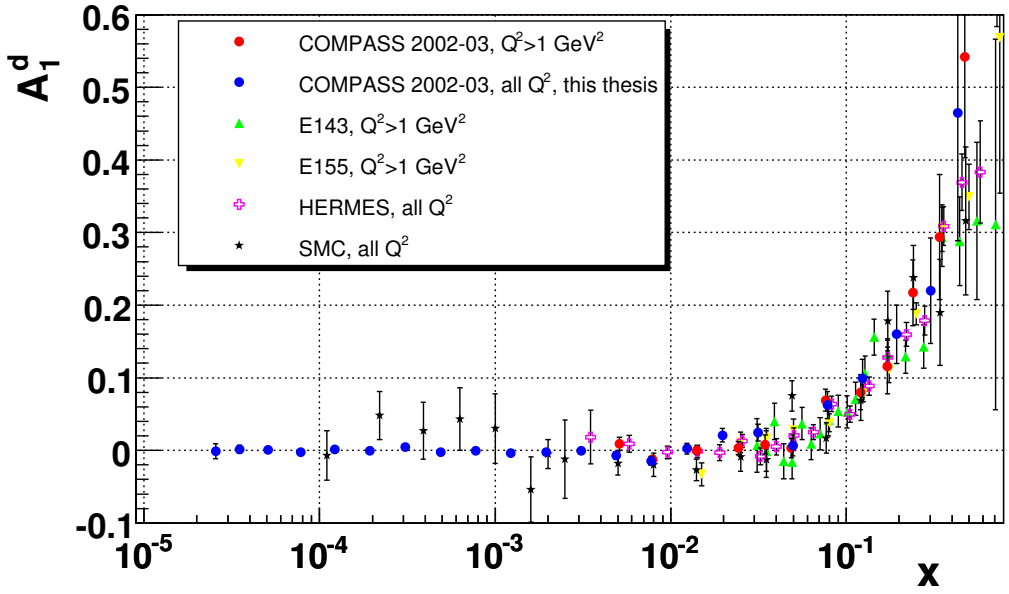

Figure 6.4: The comparison of the A_1^d spin asymmetry measured by different experiments. Errors are statistical.

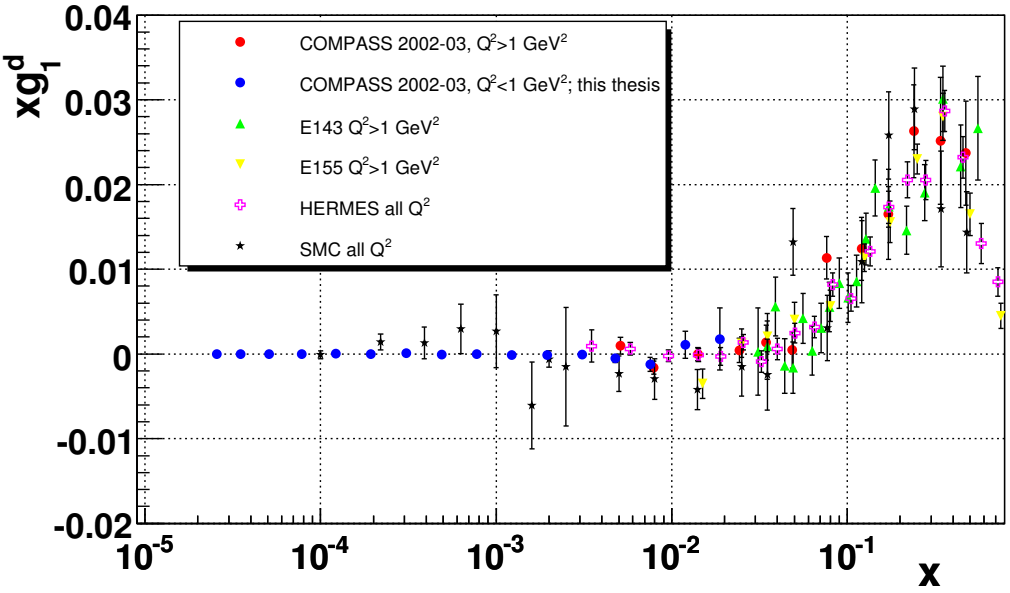

Figure 6.5: The comparison of the xg_1^d spin structure function measured by different experiments. Errors are statistical.

6.4 Regge model tests

The Regge model predicts the following behavior of g_1^d in the $Q^2 << W^2$ (or low x) limit, see section 2.2.6:

$$g_1^i(x, Q^2) \sim \beta(Q^2) x^{-\alpha_i(0)} \tag{6.6}$$

where the index i corresponds to the flavour singlet and non-singlet combination of g_1^p and g_1^n. The structure functions are defined per nucleon, therefore the following expression holds: $g_1^S = g_1^p + g_1^n \approx 2g_1^d$. The $\alpha_i(0)$ are intercepts of the corresponding Regge trajectories. They depend only on the trajectory quantum numbers. The expectations of the model are: $-0.5 < \alpha_{S,NS} < 0$. Since COMPASS used a deuteron target, only g_1^S can be compared to the model expectation.

The Regge model gives only predictions for the x dependence of g_1^d. Therefore a fixed Q^2 has to be assumed to perform the tests of the model. The data from the Q^2 range $2.5 \cdot 10^{-3} - 2.5 \cdot 10^{-1}$ GeV^2 were used. This range was divided into six sub-intervals where the Q^2 was assumed to be constant. In each sub-interval of Q^2 a few intervals of x have been selected. In all intervals the g_1^d structure function was extracted from the data. Fits were performed using the function $g_1^d(x, Q^2) = \beta(Q^2) x^{-\alpha_S(0)}$. Results were very unstable. Depending on the starting value of the fitted parameters the final value changed by a factor 2-4. This instability came from the fact that $\beta(Q^2)$ and $\alpha_i(0)$ are highly correlated. The stability of the fit increased when more x intervals were chosen in the sub-interval of Q^2. Finally 8 intervals of x were used but the obtained results were still unsatisfactory.

Another idea to compare results and predictions originated from the alignment program, where all the parameters are obtained simultaneously. Instead of separate fits for the six sub-intervals of Q^2 the fit was performed simultaneously in all of them. Six values of $\beta(Q^2)$ were fitted and **only one** $\alpha_S(0)$. The results of the fit are given in table 6.5. Values of $\alpha_s(0)$, χ^2 and $\chi^2 - \chi^2_{min}$ are shown where χ^2_{min} is a minimal value of χ^2 observed in the fit. Number of degrees of freedom was everywhere 28.

$\alpha_s(0)$	χ^2	$\chi^2 - \chi^2_{min}$
-0.50	19.7	1.5
-0.25	20.3	2.1
0.00	19.5	1.3
0.02	18.9	0.7
0.05	18.5	0.4
0.07	18.2	0.0
0.08	18.2	0.0
0.10	18.7	0.5
0.15	27.2	9.0
0.20	58.5	40.3

Table 6.5: The χ^2 values obtained in the Regge model tests.

The minimum of the χ^2 is for the $\alpha_s(0)$ from outside the range predicted by the Regge model. Positive values of $\alpha_s(0)$ larger than 0.15 can be excluded at the 3σ level. In the case of negative values, which are predicted by the model, the results are inconclusive. All the negative values of $\alpha_s(0)$ are consistent within 1.5 standard deviation with $\alpha_s(0) = 0.08$.

Observe that the χ^2 distribution of the fit results is not parabolic around the minimum. Using only the standard method of the error estimation one would get the following result: $\alpha_s(0) = 0.08^{+0.04}_{-0.07}$. This would allow to exclude **wrongly** $\alpha_s(0) < -0.13$ at 3 sigma level!

The main reason why the test failed is the limited, too narrow, x interval for a given Q^2. The x values change only by a half of the order of magnitude. The same situation is in other fixed target experiments. It seems unlikely that data from different experiments can be used together in such a test as systematic effects would then play a key role. The situation would be different in an electron-proton collider, where a larger phase space would be available. Such a test may be possible in the future eRHIC machine [60].

Chapter 7

Summary and Outlook

"A world without spin would collapse", [130]. The spin physics is used in many fields: *e.g.* in natural sciences where a transition between energy levels of hydrogen 1^3S_1 and 1^1S_0 is used to measure its abundance in the Universe, in medicine in the Nuclear Magnetic Resonance and finally even in financial trading [131].

COMPASS is an experiment at CERN which investigates internal structure of nucleons. One of the aims of the experiment is to better understand their spin properties. The collaboration consists of about 240 physicists from 11 member countries. COMPASS uses a polarized muon beam of 160 GeV energy and a polarized ^{6}LiD target.

Information about internal structure of nucleons is included in the so called structure functions. These functions are universal: they can be measured in one process and used in another. Therefore it is so important to know them at any x and Q^2. The unpolarized structure functions, especially F_2, are precisely measured. Contrary to that the polarized structure functions are poorly known. One of them, g_1, can be measured in COMPASS. This function is very interesting as $\int_0^1 g_1 dx$ gives information about how much of the nucleon spin is carried by quarks.

The region of low x is especially interesting as new phenomena are expected there, *e.g.* a parton saturation. The g_1 behaviour at low x is governed by double logarithmic corrections: $ln^2(1/x)$, which makes it more sensitive than the F_2 to the BFKL effects, which are searched for since several years. All experiments which so far measured the g_1 were fixed-target ones. This means that small values of x are reached simultaneously with small values of Q^2. For most of the COMPASS data at low x the values of Q^2 are below 1 GeV^2. These data cannot be used in the QCD analysis, nevertheless, as it was stated above, the knowledge of structure functions is important for any Q^2. Moreover physics is continuous; we must understand the region from photo-production, $Q^2 = 0$ GeV^2, to DIS, $Q^2 > 1$ GeV^2. Data at low Q^2 help a lot since they can be confronted with predictions concerning the g_1 behaviour at low x and fixed Q^2 as well as with models describing non-perturbative (*i.e.* low Q^2) effects.

In this thesis the results of the spin dependent cross section asymmetry A_1^d and spin dependent structure function g_1^d measurements in COMPASS were presented. Only the data collected in 2002 and 2003 were used. Measurements were performed in a wide kinematic range, $x \in (1.6 \cdot 10^5 - 0.6)$, $Q^2 \in (10^{-3} - 100)$ GeV^2. For the g_1^d studies the Q^2 range was restricted to $Q^2 < 1$ GeV^2. No significant spin effects were observed in the A_1^d

below $x = 0.01$. The spin asymmetry in this region was consistent with zero. The results were confronted with the Regge model predictions but the comparison turned out to be inconclusive. For $x < 0.002$ the statistical errors of the A_1^d and the g_1^d were reduced 10 times compared to results of the SMC, so far the only experiment which measured the A_1^d and the g_1^d for $x < 0.01$. COMPASS also explored the unknown region of $x \in (1.6 \cdot 10^{-5} - 10^{-4})$. The observed systematic errors of the A_1^d and g_1^d at low x are at the same level as their statistical precision. Using more COMPASS data from the 2004 and 2006 runs, will further reduce the g_1^d uncertainty even at low x. Unfortunately it seems that at present there is no other experiment which would be able to independently confirm the COMPASS results. The region of low x at both low– and high Q^2 might be explored at the future eRHIC collider [60] which should start to operate around 2020.

The spin structure of nucleons is presently investigated in other experiments: PHOENIX and STAR at RHIC, HERMES at DESY and several experiments at JLAB. At this moment the most important studies are those concerning the "spin-crisis". The EMC discovered that only a small part of the nucleon spin is carried by quarks. The rest may be carried by gluons, ΔG, or by angular momentum of quarks, L_q, and gluons, L_g. Many experiments try to determine ΔG. The recent measurement of $\Delta G/G$ from COMPASS, $\Delta G/G = 0.024 \pm 0.089 \pm 0.057$ [132], suggests that gluons do not carry much of the nucleon spin. Experiments at RHIC will probably measure ΔG more precisely. Various process connected to ΔG can be investigated there *e.g.*: $p + p \to g + q \to \gamma + jet + X$. Due to technical and theoretical problems so far the obtained results are very preliminary.

Assuming that $\Delta G \approx 0$ the spin crisis remains. It was pointed out that L_q may be accessed through the so called deeply virtual Compton scattering, *e.g.* $\gamma^* p \to \gamma p$ [133]. COMPASS as well as experiments from other laboratories *i.e* JLAB, DESY and SLAC is planning to measure this process soon.

Many physicists associate the future of high energy physics with discovering physics beyond the Standard Model (SM). It is an important motivation for building the LHC and possibly also e^+e^- linear colliders. However, a new physics is not only discovering the new particles. In searching for it spin experiments can play an important role.

Anomalous magnetic moment of the muon (a_μ) due to radiative corrections is sensitive to physics beyond the SM. Presently the value measured by the E821 Collaboration (BNL) is 2.7 standard deviations away from the SM expectation [134]. A new experiment, E969 (BNL), will reduce the error of a_μ by a factor of 2.5 compared to E821.

One can measure the weak mixing angle in *e.g.* Møller scattering. The expected asymmetries are very small, of the order of $\sim 10^{-7}$. The results of E158 Collaboration (SLAC) confirm that $sin^2\theta_W^{eff}$ is Q^2 dependent [135]. However, it agrees with the SM predictions and gives limits for masses of super–symmetric particles.

To conclude: the spin physics is an interesting subject. In the next few years new important results are expected. Hopefully, they will help to solve some mysteries of the spin.

Appendix A

Methods of asymmetry evaluation

Details about different methods of asymmetries evaluation are given here.

A.1 Observed events and the cross-section

The total available data sample for the A_1^d measurement exceeds 300 million events. These events were collected in two years of data taking. The total number of collected events depends on:

- the beam flux, ϕ, which corresponds to the number of incident muons, crossing the target;
- the number of scattering centres, n; these are all the nucleons in the target;
- the total acceptance of the spectrometer, a, which is a probability of observing an interaction, occurring in the target. The acceptance depends on several variables like x and Q^2, PV_z, and may vary with time;
- the differential cross-section $d^2\sigma/dxdQ^2$.

The acceptance variation with time may introduce false asymmetries. As the target moves, the number of the scattering centres is not constant within the target cuts. This also introduces false asymmetries. Assuming that both the acceptance and the number of scattering centres are constant over the observation (integration) time, the observed number of scattering events, N, is:

$$N = \int a\phi n \left(\frac{d^2\sigma}{dxdQ^2}\right) d\vec{\xi} \tag{A.1}$$

where $\int d\vec{\xi}$ denotes integration over variables like x, Q^2, PV_z etc. The beam and the target are polarized. The above expression can be rewritten so that the helicities of the beam and of the target are explicitly indicated. For simplicity the differential cross-section $d^2\sigma/dxdQ^2$ will be denoted by σ. The arrows $\sigma^{\uparrow\uparrow}, \sigma^{\uparrow 0}, \sigma^{\uparrow\downarrow}, \phi^{\uparrow}n^{\downarrow}$ indicate the relative spin orientations of the beam and the deuteron target. As only a relative spin orientation matters, the following expressions hold: $\sigma^{\uparrow\uparrow} = \sigma^{\downarrow\downarrow}$, $\sigma^{\uparrow\downarrow} = \sigma^{\downarrow\uparrow}$, $\sigma^{\uparrow 0} = \sigma^{\downarrow 0}$.

$$N = \int d\vec{\xi}\, a \left[(\phi^{\uparrow} n^{\uparrow} + \phi^{\downarrow} n^{\downarrow})\sigma^{\uparrow\uparrow} + (\phi^{\uparrow} n^{\downarrow} + \phi^{\downarrow} n^{\uparrow})\sigma^{\uparrow\downarrow} + (\phi^{\uparrow} + \phi^{\downarrow}) n^0 \sigma^{\uparrow 0} + (\phi^{\uparrow} + \phi^{\downarrow}) \sum_i n_i \bar{\sigma}_i \right] \tag{A.2}$$

where the $\sum_i n_i \bar{\sigma}_i$ is a sum over all elements in the target but deuteron. As most of these elements are nonpolarizable, a spin average cross-section, $\bar{\sigma}$, is used. Let us rewrite the above equation as

$$\begin{aligned} N = \int d\vec{\xi}\, a [& (\phi^{\uparrow} n^{\uparrow} + \phi^{\downarrow} n^{\downarrow})(\sigma^{\uparrow\uparrow}/2 + \sigma^{\uparrow\downarrow}/2 + \sigma^{\uparrow\uparrow}/2 - \sigma^{\uparrow\downarrow}/2) + \\ & (\phi^{\uparrow} n^{\downarrow} + \phi^{\downarrow} n^{\uparrow})(\sigma^{\uparrow\downarrow}/2 + \sigma^{\uparrow\uparrow}/2 + \sigma^{\uparrow\downarrow}/2 - \sigma^{\uparrow\uparrow}/2) + \\ & (\phi^{\uparrow} + \phi^{\downarrow}) n^0 \sigma^{\uparrow 0} + (\phi^{\uparrow} + \phi^{\downarrow}) \textstyle\sum_i n_i \bar{\sigma}_i] \end{aligned} \tag{A.3}$$

Now assuming that $\sigma^{\uparrow 0} = (\sigma^{\uparrow\uparrow} + \sigma^{\uparrow\downarrow})/2 \equiv \bar{\sigma}$ we get

$$\begin{aligned} N = \int d\vec{\xi}\, a [& (\phi^{\uparrow} + \phi^{\downarrow})(n^{\uparrow} + n^{\downarrow} + n^0)\bar{\sigma} - (\phi^{\uparrow} n^{\uparrow} + \phi^{\downarrow} n^{\downarrow})(\sigma^{\uparrow\downarrow}/2 - \sigma^{\uparrow\uparrow}/2) + \\ & (\phi^{\uparrow} n^{\downarrow} + \phi^{\downarrow} n^{\uparrow})(\sigma^{\uparrow\downarrow}/2 - \sigma^{\uparrow\uparrow}/2) + (\phi^{\uparrow} + \phi^{\downarrow}) \textstyle\sum_i n_i \bar{\sigma}_i] \end{aligned} \tag{A.4}$$

$(\phi^{\uparrow} + \phi^{\downarrow}) = \phi$ is a total flux and $(n^{\uparrow} + n^{\downarrow} + n^0) = n$ is a total number of polarized scattering centres

$$N = \int d\vec{\xi}\, a \left[\phi n \bar{\sigma} - (\phi^{\uparrow} - \phi^{\downarrow})(n^{\uparrow} - n^{\downarrow})(\sigma^{\uparrow\downarrow}/2 - \sigma^{\uparrow\uparrow}/2) + \phi \sum_i n_i \bar{\sigma}_i \right] \tag{A.5}$$

If we introduce the beam and the deuteron target polarizations:

$$P_b = \frac{\phi^{\uparrow} - \phi^{\downarrow}}{\phi^{\uparrow} + \phi^{\downarrow}} \qquad\qquad P_t = \frac{n^{\uparrow} - n^{\downarrow}}{n^{\uparrow} + n^{\downarrow} + n^0} \tag{A.6}$$

and define the measured asymmetry:

$$A_{||}^T = (\sigma^{\uparrow\downarrow} - \sigma^{\uparrow\uparrow})/(\sigma^{\uparrow\downarrow} + \sigma^{\uparrow\uparrow}) \tag{A.7}$$

then we can rewrite the equation (A.5) in a simpler form:

$$N = \int d\vec{\xi}\, a \left[\phi n \bar{\sigma} - \phi n \bar{\sigma} P_b P_t A_{||}^T + \phi \sum_i n_i \bar{\sigma}_i \right] \tag{A.8}$$

Finally if we introduce the dilution factor (cf. section 5.3.5) and use approximate formula $A_{||} \simeq D A_1$, see equation (2.25), the final form of the equation (A.8) becomes:

$$N = \int d\vec{\xi}\, a \phi n \bar{\sigma} \left[1 - f D P_b P_t A_1^{(T)} \right] \tag{A.9}$$

Here the $A_1^{(T)}$ is the spin dependent cross section asymmetry; the 'T' is in brackets as usually radiative corrections are included in the dilution factor, see section 5.3.5. In that case the A_1 asymmetry is extracted. If a simple dilution factor formula, *i.e.* equation (5.6), is used then the A_1^T can be extracted.

A.2 The 1st order method of asymmetry extraction

Let us consider the expression (A.9) as a tool for the asymmetry determination. We assume that f, D, P_b and P_t are approximately constant.

$$A_1 = \left[1 - \frac{N}{\int d\vec{\xi}\, a\phi n\bar{\sigma}}\right] \frac{1}{< f >< D >< P_b >< P_t >} \tag{A.10}$$

In COMPASS the incident flux is known with a precision of about 10 %. Thus $\delta A_1 \approx 0.1/ < fDP_bP_t >> 1.0$, where $< fDP_bP_t > \approx 0.07$ has been assumed, cf. section 5.2. The error of the asymmetry is large and its precise measurement is not possible in this way. To achieve a high precision measurement of asymmetry the flux and the cross-section should cancel out. Let us consider the ratio:

$$\Delta_{raw} = \frac{N_u - N_d}{N_u + N_d} \tag{A.11}$$

where N_u, N_d are the numbers of events observed in the upstream and the downstream target cell, respectively. The muon flux is in general not the same in the two cells but the equality can be assured during the data selection, cf. section 5.2.2. Now, if we consider a small interval of x, Q^2 where $a_{u,d}(x, Q^2, PV_z)$, $f_{u,d}(x, Q^2)$, $D(y, Q^2)$, *etc.* are approximately constant the cross-section and the flux which are hidden in equation (A.11) will cancel out. This works only in a small x, Q^2 interval because the integral in (A.9) is in general a convolution of $\sigma(x, Q^2)$, $a(x, Q^2, PV_z)$, $f(x, Q^2)$, $D(y, Q^2)$, *etc.* Using the expression (A.9) we can rewrite (A.11) in the following form:

$$\Delta_{raw} = \frac{(a_u n_u - a_d n_d) - fDP_b(a_u n_u P_u - a_d n_d P_d)A_1}{(a_u n_u + a_d n_d) - fDP_b(a_u n_u P_u + a_d n_d P_d)A_1} \tag{A.12}$$

Let us introduce $r \equiv a_u n_u / a_d n_d$ and neglect the second part of the denominator: $fDP_b(a_u n_u P_u + a_d n_d P_d)A_1$. The neglected term is small as $fDP_bP_tA_1$ is usually $\ll 0.1$ and $P_u \sim -P_d$. Note that $f_u = f_d$ was put for simplicity.

$$\Delta_{raw} = \frac{r-1}{r+1} - \frac{< f >< D >< P_b > (rP_u - P_d)}{r+1} A_1, \tag{A.13}$$

and

$$A_1 = \frac{1}{< f >< D >< P_b >< P_t >} \Delta_{raw} - \frac{1}{< f >< D >< P_b >< P_t >} \left(\frac{r-1}{r+1}\right). \tag{A.14}$$

here $< f >$, $< D >$ and $< P_t >$ are the mean values of f, D in the x, Q^2 bin and $< P_t >$ is defined as

$$< P_t >= \frac{r|P_u| + |P_d|}{r+1} \tag{A.15}$$

If $r = 1$ then $< P_t >$ becomes an arithmetic average of the $|P_i|$. For the case $f_u \neq f_d$ we can define:

$$< fP_t >= \frac{rf_u|P_u| + f_d|P_d|}{r+1} \tag{A.16}$$

In the expression (A.14) A_1 is a linear function of Δ_{raw} therefore this method of the asymmetry extraction is called the 1st order method.

The error on A_1 extracted from equation (A.14) can be derived from the standard error propagation. It is assumed that r is known precisely and $\delta N_i = \sqrt{N_i}$

$$\delta A_1 = \frac{1}{< f >< D >< P_b >< P_t >} \sqrt{\frac{4N_u N_d}{(N_u + N_d)^3}} \tag{A.17}$$

if $N_u \approx N_d$ then $4N_u N_d \approx (N_u + N_d)^2$ and equation (A.17) simplifies to a form:

$$\delta A_1 = \frac{1}{< f >< D >< P_b >< P_t >} \sqrt{\frac{1}{(N_u + N_d)}} \tag{A.18}$$

The A_1 is finally not proportional to Δ_{raw}. There is an additional term $\sim (r-1)/(r+1)$ which biases the measurement. That term is called a false asymmetry. In principle r can be determined from the data *e.g.* when the target was not polarized but this solution is inconvenient. A way of overcoming the r problem was found already in the EMC [7], [8]. The polarization of cells cannot be fixed but it should be reversed regularly. The data before and after the polarization reversal have to be combined. Let us consider the measurements:

$$\Delta_{raw} = \frac{N_u - N_d}{N_u + N_d} \qquad \Delta'_{raw} = \frac{N'_u - N'_d}{N'_u + N'_d} \tag{A.19}$$

then the A_1 is given by:

$$A_1 = \frac{1}{< f >< D >< P_b >< P_t >} \frac{\Delta_{raw} + \Delta'_{raw}}{2} - \frac{1}{< f >< D >< P_b >< P_t >} \left(\frac{r-1}{r+1} - \frac{r'-1}{r'+1} \right) \tag{A.20}$$

To assure that false asymmetry is zero or small, it is enough to fulfill $r/r' = 1$. It is much easier to achieve than the $r = 1$. In addition r does not need to be known at all. This is a large benefit as any r determination would have a finite precision and this would introduce an additional uncertainty to the asymmetry measurement. In fact this is especially important for the A_1 measurement at the low x and low Q^2 where the asymmetry is expected to be small and therefore r would have to be measured very precisely.

Stability of the COMPASS apparatus before and after the field reversal

A few remarks on the stability of r/r' in COMPASS case are in place here. As it is discussed in section 5.7.5, the COMPASS target moves during the field reversals. This may introduce an asymmetry bias as the number of the nucleons within the target cuts changes. To prevent this situation the target cuts are changed (cf. section 5.2.2) depending on the analyzed target configuration. The second possible problem is the Lorentz effect discussed in section 4.6. Due to this effect the same track might have different reconstruction probabilities depending on the solenoid field direction. Also some detectors move during the field reversals. This affects the reconstruction efficiency and may lead as well to an asymmetry bias. Due to the detector movement two different alignment files are needed for further reconstruction. As the alignment method is not fully automatic this leaves a chance for a "human error". The false asymmetry estimation is the key issue for the measurement of A_1^d, g_1^d in the low x, Q^2.

The 1st order method of the asymmetry extraction cont.

Equation (A.20) together with the assumption $r/r' = 1$ becomes:

$$A_1 = \frac{1}{2 < f >< D >< P_b >< P_t >} \left(\frac{N_u - N_d}{N_u + N_d} - \frac{N'_u - N'_d}{N'_u + N'_d} \right) \tag{A.21}$$

and the error:

$$\delta A_1 = \frac{1}{2 < f >< D >< P_b >< P_t >} \sqrt{\frac{1}{N_u + N_d} + \frac{1}{N'_u + N'_d}} \tag{A.22}$$

The above equations give the simplest estimation of the A_1^d asymmetry and its error. The presented method has at least three drawbacks: *i*) it should be used only for a measurement of small asymmetries, *ii*) the r should not be very different from one; assumptions *i*) and *ii*) are needed to assure that the factor which contains A_1 in the denominator of the equation (A.12) can be safely neglected and finally *iii*) some information is lost since the quantities f, D, P_b are measured on the event-by-event basis whereas in the equation (A.21) only mean values are used. Regaining the information would reduce the δA_1.

Improvements of the 1st order method

In this section a brief discussion of improvements of asymmetry measurement is given. More detailed information can be found in [129],[136].

In equation (A.12) one of the terms in the denominator was neglected. This permitted a linearization of the $A_1 - \Delta_{raw}$ dependence. The asymmetry measurement can be more accurate if the mentioned part of the denominator is not neglected but when two data sets Δ_{raw} and Δ'_{raw} are combined instead. The derivation of formulas is skipped. The final results are presented:

$$A_1 = \frac{(1+r)^2}{4r} \frac{1}{2 < f >< D >< P_b >< P_t >} \left(\frac{N_u - N_d}{N_u + N_d} - \frac{N'_u - N'_d}{N'_u + N'_d} \right) \tag{A.23}$$

$$\delta A_1 = \sqrt{\frac{(1+r)^2}{4r}} \frac{1}{2 < f >< D >< P_b >< P_t >} \sqrt{\frac{1}{N_u + N_d} + \frac{1}{N'_u + N'_d}} \tag{A.24}$$

Observe that the $< P_t >$ definition now becomes:

$$< P_t >= \frac{1}{4}(P_u + P_d + P'_u + P'_d) \tag{A.25}$$

In the $r = 1$ case the simplest method and the updated one give the same results. If $r \neq 1$ then there is a correction factor; moreover if r strongly deviates from 1, we can estimate if the precision of δr is sufficient not to bias the asymmetry. This was impossible for the simplest method. The new method requires a precise knowledge of r if it differs much from 1. This inconvenience can be removed by redefining of the counting asymmetry:

$$\Delta_{raw} = \frac{N_u - \tilde{r} N_d}{N_u + \tilde{r} N_d} \tag{A.26}$$

where $\tilde{r}$ is the estimator of r. Finally one gets:

$$A_1 = \frac{(1+r/\tilde{r})^2}{4r/\tilde{r}} \frac{1}{2 < f >< D >< P_b >< P_t >} \left(\frac{N_u - \tilde{r}N_d}{N_u + \tilde{r}N_d} - \frac{N'_u - \tilde{r}N'_d}{N'_u + \tilde{r}N'_d} \right) \tag{A.27}$$

$$\delta A_1 = \sqrt{\frac{(1+r/\tilde{r})^2}{4r/\tilde{r}}} \frac{1}{2 < f >< D >< P_b >< P_t >} \sqrt{\frac{1}{N_u + \tilde{r}N_d} + \frac{1}{N'_u + \tilde{r}N'_d}} \tag{A.28}$$

As an example let us compare the described methods for $r = 0.30 \pm 0.03$. Using the simplest method we do not even know that we obtained a biased asymmetry. If we use the updated method then the correction factor becomes $(1+r)^2/4r = 1.41 \pm 0.08$. Therefore independently from the event statistics we cannot extract A_1 with a relative precision better than $\approx 6\%$. Finally, if we use the method with redefinition of the counting rate, the possible bias is $(1+r/\tilde{r})^2/(4r/\tilde{r}) = 1.000 \pm 0.002$, thus reduced by a factor of 40. The assumed value $r = 0.3$ seems to be a small number but it may indeed be found in the data.

The advantage of the 1st order method is its simple, intuitive character. Yet, in some cases this method gives wrong results. Two updates of the method were presented. At least one of them strongly reduces the bias and can be used in a wide range of A_1 and r values. This updated method still has drawbacks, *i.e.* the r value has to be known *a priori* and the method losses its intuitive character. In fact, the simplest solution is not to skip any part(s) of the denominator, in *e.g.* equation (A.12), but to solve the 2nd order equation. Before this case, called *2nd order method* is discussed, another attempt to improve the 1st order method by using weights will be considered.

A.3 Weighted 1st order method

As it was mentioned before in the 1st order method only mean values of $< f >$, $< D >$, $< P_b >$ and $< P_t >$ are considered. This is not an optimal solution as far as the statistical error is considered. A more effective approach is a computation of f, D, P_b and P_t on the event-by-event basis. Let us assume a (x, Q^2) bin in which:

$$A_1 = \frac{1}{< f >< D >< P_b >< P_t >} \left(\frac{N_u - N_d}{N_u + N_d} \right) \tag{A.29}$$

$$\delta A_1 = \frac{1}{< f >< D >< P_b >< P_t >} \sqrt{\frac{1}{(N_u + N_d)}} \tag{A.30}$$

Now we divide this bin into i sub-bins. We assume that in the sub-bin i we have $(< f >< D >< P_b > \ < P_t >)_i$.

$$A_1^i = \frac{1}{(< f >< D >< P_b >< P_t >)_i} \left(\frac{N_u^i - N_d^i}{N_u^i + N_d^i} \right) \tag{A.31}$$

$$\delta A_1^i = \frac{1}{(< f >< D >< P_b >< P_t >)_i} \sqrt{\frac{1}{(N_u^i + N_d^i)}} \tag{A.32}$$

In that case the A_1 asymmetry will be weighted as an average of A_1^i measurements:

$$A_1 = \frac{\sum_i A_1^i \frac{1}{(\delta A_1^i)^2}}{\sum_i \frac{1}{(\delta A_1^i)^2}} \tag{A.33}$$

$$\delta A_1 = \left(\sqrt{\sum_i \frac{1}{(\delta A_1^i)^2}} \right)^{-1} \tag{A.34}$$

Hence:

$$A_1 = \frac{\sum_i \frac{1}{(<f><D><P_b><P_t>)_i} \left(\frac{N_u^i - N_d^i}{N_u^i + N_d^i} \right) \cdot (< f >< D >< P_b >< P_t >)_i^2 (N_u^i + N_d^i)}{\sum_i (< f >< D >< P_b >< P_t >)_i^2 (N_u^i + N_d^i)} \tag{A.35}$$

$$\delta A_1 = \frac{\sum_i (< f >< D >< P_b >< P_t >)_i (N_u^i - N_d^i)}{\sum_i (< f >< D >< P_b >< P_t >)_i^2 (N_u^i + N_d^i)} \tag{A.36}$$

Each sum in the above equations above can be performed separately, thus we can divide our data sample in such a way that in each sub-bin there is only one event.

$$A = \frac{\sum_j^{N_u} (f D P_b P_t)_j - \sum_j^{N_d} (f D P_b P_t)_j}{\sum_j^{N_u} (f D P_b P_t)_j^2 + \sum_j^{N_d} (f D P_b P_t)_j^2} \tag{A.37}$$

The error of the weighted asymmetry can be rewritten as:

$$\delta A = \sqrt{\frac{1}{\sum_j^{N_u} (f D P_b P_t)_j^2 + \sum_j^{N_d} (f D P_b P_t)_j^2}} \tag{A.38}$$

The $f D P_b P_t$ is usually called a weight and denoted as w. Note that the derived formulae are simplified, as the data combining before and after the field reversal was not included. The correct formula can be found easily as:

$$A_1 = \frac{1}{2} \left(\frac{\sum_j^{N_u} (w)_j - \sum_j^{N_d} (w)_j}{\sum_j^{N_u} (w)_j^2 + \sum_j^{N_d} (w)_j^2} - \frac{\sum_j^{N'_u} (w)_j - \sum_j^{N'_d} (w)_j}{\sum_j^{N'_u} (w)_j^2 + \sum_j^{N'_d} (w)_j^2} \right) \tag{A.39}$$

$$\delta A_1 = \frac{1}{2} \sqrt{\frac{1}{\sum_j^{N_u} (w)_j^2 + \sum_j^{N_d} (w)_j^2} + \frac{1}{\sum_j^{N'_u} (w)_j^2 + \sum_j^{N'_d} (w)_j^2}} \tag{A.40}$$

From the statistical point of view the $f D P_b P_t$ weight is optimal as it gives the smallest statistical error. Unfortunately, from the point of view of the systematics this is not so. As the weight is computed for every event, it is necessary that the mean value of the weight is the same before and after the polarization reversal. If it is not then in the equation (A.20) the part with r, r' does not cancel and false asymmetries appear [129]. In the COMPASS case P_t cannot be used in the weight. Many times during the data taking the polarized target is not in the frozen spin mode but it is still being polarized. In fact the problem with a constant weight was first found by the SMC. Large false asymmetries in some parts of the data were observed. After excluding P_t from the weight they disappeared. Therefore a **correct weight for a COMPASS** case is **w=fDP$_b$** . As for the target polarization the mean value, $< P_t >$, has to be used.

In the previous section some improvements of the 1st order method from the point of view of r and A_1 value were presented. All these formulae can be replaced by weighted ones. The replacement is intuitive.

A.4 Averages of kinematical variables

Quantities like Q^2, x, y often have to be averaged in the analysis. The convention used here is the following:

$$< X >= \frac{\sum_i X_i (\delta A)_i^{-2}}{\sum_i (\delta A)_i^{-2}} = \frac{\sum_j^N X_j^N w_j^2}{\sum_j^N w_j^2} \tag{A.41}$$

where $w = fDP_b$.

A.5 The 2nd order method

In this section a brief description of the 2nd order non-weighted method of the asymmetry extraction is given. The starting point is again the expected number of events for two data sets taken before and after the field rotation.

$$N_u = \int d\vec{\xi} a_u \phi n_u \bar{\sigma}(1 + f_u D P_b P_u A_1) = \alpha_u (1 + \beta_u A_1) \tag{A.42}$$

$$N_d = \int d\vec{\xi} a_d \phi n_d \bar{\sigma}(1 + f_d D P_b P_d A_1) = \alpha_d (1 + \beta_d A_1) \tag{A.43}$$

$$N'_u = \int d\vec{\xi} a'_u \phi' n'_u \bar{\sigma}(1 + f_u D P_b P'_u A_1) = \alpha'_u (1 + \beta'_u A_1) \tag{A.44}$$

$$N'_d = \int d\vec{\xi} a'_d \phi' n'_d \bar{\sigma}(1 + f_d D P_b P'_d A_1) = \alpha'_d (1 + \beta'_d A_1). \tag{A.45}$$

where $\vec{\xi}$ denotes the integration over all variables (x, Q^2, PV_z *etc.*). Note that the fluxes in the upstream and the downstream target cells are assumed to be the same. Here fDP_bP_t is denoted as β not as w to avoid confusion with a weight. The integrals above are equivalent to:

$$N_i =< a_i > (1 + < \beta_i >) A_1 \int \phi n_u \bar{\sigma} d\vec{\xi} \tag{A.46}$$

where the average acceptance:

$$< a_i >= \frac{\int a_i \phi n_i \bar{\sigma} d\vec{\xi}}{\int \phi n_i \bar{\sigma} d\vec{x}} \tag{A.47}$$

and the average $< \beta >$

$$< \beta_i >= \frac{\int \beta_i \phi n_i \bar{\sigma} d\vec{\xi}}{\int \phi n_i \bar{\sigma} d\vec{\xi}} \approx \frac{\sum_j^{N_i} \beta_j}{N_i}. \tag{A.48}$$

An interesting quantity is following ratio of the observed yields:

$$\delta = \frac{N_u N'_d}{N_d N'_u} \tag{A.49}$$

$$\delta = \frac{\int \phi n_u \bar{\sigma} d\vec{\xi} \int \phi' n'_d \bar{\sigma} d\vec{\xi}}{\int \phi n_d \bar{\sigma} d\vec{\xi} \int \phi' n'_u \bar{\sigma} d\vec{\xi}} \frac{< a_u >< a'_d >}{< a_d >< a'_u >} \frac{(1 + < \beta_u > A_1)(1 + < \beta'_d > A_1)}{(1 + < \beta_d > A_1)(1 + < \beta'_u > A_1)} \tag{A.50}$$

The ratio of the integrals and acceptances can be approximated by 1, hence:

$$\delta = \frac{(1+ < \beta_u > A_1)(1+ < \beta'_d > A_1)}{(1+ < \beta_d > A_1)(1+ < \beta'_u > A_1)} \tag{A.51}$$

This leads to a second order equation for the asymmetry extraction:

$$aA_1^2 + bA_1 + c = 0 \tag{A.52}$$

where:

$$a = \delta < \beta'_u >< \beta_d > - < \beta_u >< \beta_d > \tag{A.53}$$

$$b = \delta(< \beta'_u > + < \beta_d >) - (< \beta_u > + < \beta_d >) \tag{A.54}$$

$$c = \delta - 1 \tag{A.55}$$

Then if $a \neq 0$

$$A_1 = \frac{-b \pm \sqrt{b^2 - 4ac}}{2a} \tag{A.56}$$

or in the case of $a = 0$: $A_1 = -c/b$. The the error if A_1 [1] is given by:

$$\delta A_1 = \frac{1}{< \beta > \sqrt{N_u + N_d + N'_u + N'_d}} \tag{A.57}$$

Contrary to the 1st order method, r does not need to be known at all. Even small values of r do not introduce any bias.

A.6 The 2nd order weighted method

Weighting can be introduced in a natural way into the 2nd order method. The optimal weight would be fDP_bP_t but because of the reasons discussed in section A.3 the target polarization has to be removed from this expression. Following the formalism from the 2nd order method we get:

$$p_i = \int w(\vec{\xi}) N_i(\vec{\xi}) d\vec{\xi} \approx \sum_j^{N_i} w_j \tag{A.58}$$

and

$$< a_i >_w = \frac{\int a_i w \phi n_i \bar{\sigma} d\vec{\xi}}{\int w \phi n_i \bar{\sigma} d\vec{\xi}} \tag{A.59}$$

$$< \beta_i >_w = \frac{\int \beta_i w \phi n_i \bar{\sigma} d\vec{\xi}}{\int w \phi n_i \bar{\sigma} d\vec{\xi}} \approx \frac{\sum_j^{N_i} w_j \beta_j}{p_i} \tag{A.60}$$

The ratio δ is now defined as:

$$\delta = \frac{p_u p'_d}{p_d p'_u} \tag{A.61}$$

After similar assumption as in the 2nd order method we get:

[1] Here we assume $N_u \approx N_d \approx N'_u \approx N'_d$.

$$aA^2 + bA + c = 0, \tag{A.62}$$

here:

$$a = \delta < \beta'_u >_w < \beta_d >_w - < \beta_u >_w < \beta_d >_w \tag{A.63}$$

$$b = \delta(< \beta'_u >_w + < \beta_d >_w) - (< \beta_u >_w + < \beta_d >_w) \tag{A.64}$$

$$c = \delta - 1 \tag{A.65}$$

for $a \neq 0$

$$A_1 = \frac{-b \pm \sqrt{b^2 - 4ac}}{2a} \tag{A.66}$$

or in the case of $a = 0$: $A_1 = -c/b.$// The error is now

$$\delta A_1 = \sqrt{\frac{1}{< \beta^2 > N}} \tag{A.67}$$

which means that it is reduced by a factor $\sqrt{< \beta >^2 / < \beta >^2}$ compared to the non-weighted method. The above formula is in fact an approximation for the case where $N_u \approx N_d \approx N'_u \approx N'_d$. **The second order weighted method of the asymmetry extraction was the main method used in this analysis.**

Bibliography

[1] M. Gell-Mann, *Phys. Lett.* **8** (1964) 214.

[2] **SLAC-SP-017** Collaboration, J. E. Augustin *et al.*, *Phys. Rev. Lett.* **33** (1974) 1406.

[3] **E598** Collaboration, J. J. Aubert *et al.*, *Phys. Rev. Lett.* **33** (1974) 1404.

[4] R. P. Feynman, *Phys. Rev. Lett.* **23** (1969) 1415.

[5] M. J. Alguard *et al.*, *Phys. Rev. Lett.* **37** (1976) 1258.

[6] G. Baum *et al.*, *Phys. Rev. Lett.* **51** (1983) 1135.

[7] **European Muon** Collaboration, J. Ashman *et al.*, *Phys. Lett.* **B206** (1988) 364.

[8] **European Muon** Collaboration, J. Ashman *et al.*, *Nucl. Phys.* **B328** (1989) 1.

[9] J. R. Ellis and R. L. Jaffe, *Phys. Rev.* **D9** (1974) 1444.

[10] F. E. Close and R. G. Roberts, *Phys. Lett.* **B316** (1993) 165, `hep-ph/9306289`.

[11] **Spin Muon** Collaboration, B. Adeva *et al.*, *Phys. Rev.* **D58** (1998) 112001.

[12] **E142** Collaboration, P. L. Anthony *et al.*, *Phys. Rev.* **D54** (1996) 6620, `hep-ex/9610007`.

[13] **E143** Collaboration, K. Abe *et al.*, *Phys. Rev. Lett.* **75** (1995) 25.

[14] **E154** Collaboration, K. Abe *et al.*, *Phys. Rev. Lett.* **79** (1997) 26–30, `hep-ex/9705012`.

[15] **E155** Collaboration, P. L. Anthony *et al.*, *Phys. Lett.* **B463** (1999) 339, `hep-ex/9904002`.

[16] **HERMES** Collaboration, A. Airapetian *et al.*, *Phys. Lett.* **B442** (1998) 484, `hep-ex/9807015`.

[17] **HERMES** Collaboration, C. Riedl *et al.*, ,. Proceedings of the 16th International Spin Physics Symposium, Trieste, Italy, October 10-16 2004.

[18] **COMPASS** Collaboration, P. L. Anthony *et al.*, *CERN/SPSLC* **96-14** (1996).

[19] **Spin Muon** Collaboration, B. Adeva *et al.*, *Phys. Rev.* **D60** (1999) 072004; Erratum-ibid.D62:079902,2000.

[20] J. Kiryluk, PhD thesis, Warsaw University, 2000.

[21] R. P. Feynman, *Phys. Rev. Lett.* **23** (1969) 1415.

[22] F. Halzen and A. Martin, *Quarks and Leptons: An Introductory Course in Modern Particle Physics*. John Wiley & Sons, 1984.

[23] P. Hoodbhoy, R. L. Jaffe and A. Manohar, *Nucl. Phys.* **B312** (1989) 571.

[24] H. Khan and P. Hoodbhoy, *Phys. Lett.* **B298** (1993) 181.

[25] J. Soffer and O. V. Teryaev, *Phys. Lett.* **B490** (2000) 106, `hep-ph/0005132`.

[26] **E155** Collaboration, P. L. Anthony *et al.*, *Phys. Lett.* **B553** (2003) 18, `hep-ex/0204028`.

[27] **E155** Collaboration, P. L. Anthony *et al.*, *Phys. Lett.* **B458** (1999) 529, `hep-ex/9901006`.

[28] **E143** Collaboration, K. Abe *et al.*, *Phys. Rev. Lett.* **76** (1996) 587, `hep-ex/9511013`.

[29] **Spin Muon** Collaboration, D. Adams *et al.*, *Phys. Lett.* **B336** (1994) 125, `hep-ex/9408001`.

[30] S. Wandzura and F. Wilczek, *Phys. Lett.* **B72** (1977) 195.

[31] M. Breidenbach *et al.*, *Phys. Rev. Lett.* **23** (1969) 935.

[32] V. N. Gribov and L. N. Lipatov, *Sov. J. Nucl. Phys.* **15** (1972) 438.

[33] L. N. Lipatov, *Sov. J. Nucl. Phys.* **20** (1975) 94.

[34] G. Altarelli and G. Parisi, *Nucl. Phys.* **B126** (1977) 298.

[35] Y. L. Dokshitzer, *Sov. Phys. JETP* **46** (1977) 641.

[36] A. M. Cooper-Sarkar, R. C. E. Devenish and A. De Roeck, *Int. J. Mod. Phys.* **A13** (1998) 3385, `hep-ph/9712301`.

[37] V. S. Fadin, E. A. Kuraev and L. N. Lipatov, *Phys. Lett.* **B60** (1975) 50.

[38] E. A. Kuraev, L. N. Lipatov and V. S. Fadin, *Sov. Phys. JETP* **44** (1976) 443.

[39] E. A. Kuraev, L. N. Lipatov and V. S. Fadin, *Sov. Phys. JETP* **45** (1977) 199.

[40] I. I. Balitsky and L. N. Lipatov, *Sov. J. Nucl. Phys.* **28** (1978) 822.

[41] **H1** Collaboration, C. Adloff *et al.*, *Phys. Lett.* **B542** (2002) 193, `hep-ex/0206029`.

[42] **H1** Collaboration, C. Adloff *et al.*, *Phys. Lett.* **B462** (1999) 440, `hep-ex/9907030`.

[43] **H1** Collaboration, A. Aktas *et al.*, *Eur. Phys. J.* **C36** (2004) 441, `hep-ex/0404009`.

[44] **D0** Collaboration, B. Abbott *et al.*, *Phys. Rev. Lett.* **84** (2000) 5722, hep-ex/9912032.

[45] M. Ciafaloni, *Nucl. Phys.* **B296** (1988) 49.

[46] S. Catani, F. Fiorani and G. Marchesini, *Phys. Lett.* **B234** (1990) 339.

[47] S. Catani, F. Fiorani and G. Marchesini, *Nucl. Phys.* **B336** (1990) 18.

[48] L. V. Gribov, E. M. Levin and M. G. Ryskin, *Phys. Rept.* **100** (1983) 1.

[49] P. Collins, *An Introduction to Regge Theory and High Energy Scattering.* Cambridge University Press, 1977.

[50] J. J. Sakurai and D. Schildknecht, *Phys. Lett.* **B40** (1972) 121.

[51] P. Collins and A. Martin, *Hadron Interactions.* Adam Higler & Sons, 1984.

[52] **ZEUS** Collaboration, J. Breitweg *et al.*, *Phys. Lett.* **B487** (2000) 53, hep-ex/0005018.

[53] **E155** Collaboration, G. S. Mitchell, hep-ex/9903055.

[54] $http://www-h1.desy.de/h1/www/publications/H1\_sci\_results.shtml$.

[55] **Spin Muon** Collaboration, B. Adeva *et al.*, *Phys. Rev.* **D58** (1998) 112002.

[56] **COMPASS** Collaboration, E. S. Ageev *et al.*, *Phys. Lett.* **B612** (2005) 154, hep-ex/0501073.

[57] R. Windmolders, (COMPASS), private communication, 2005.

[58] R. Mertig and W. L. van Neerven, *Z. Phys.* **C70** (1996) 637, hep-ph/9506451.

[59] W. Vogelsang, *Phys. Rev.* **D54** (1996) 2023, hep-ph/9512218.

[60] A. Deshpande, R. Milner, R. Venugopalan and W. Vogelsang, hep-ph/0506148.

[61] M. A. Ahmed and G. G. Ross, *Phys. Lett.* **B56** (1975) 385.

[62] B. Badelek, *Acta Phys. Polon.* **B34** (2003) 2943, hep-ph/0306101.

[63] J. Bartels, B. I. Ermolaev and M. G. Ryskin, *Z. Phys.* **C70** (1996) 273, hep-ph/9507271.

[64] J. Kwiecinski and B. Ziaja, *Phys. Rev.* **D60** (1999) 054004, hep-ph/9902440.

[65] B. Badelek and J. Kwiecinski, *Phys. Lett.* **B418** (1998) 229, hep-ph/9709363.

[66] R. L. Heimann, *Nucl. Phys.* **B64** (1973) 429.

[67] J. R. Ellis and M. Karliner, *Phys. Lett.* **B213** (1988) 73.

[68] F. E. Close and R. G. Roberts, *Phys. Lett.* **B336** (1994) 257, hep-ph/9407204.

[69] S. D. Bass and P. V. Landshoff, *Phys. Lett.* **B336** (1994) 537, hep-ph/9406350.

[70] B. Badelek, J. Kiryluk and J. Kwiecinski, *Phys. Rev.* **D61** (2000) 014009, hep-ph/9907569.

[71] B. Badelek, J. Kwiecinski and B. Ziaja, *Eur. Phys. J.* **C26** (2002) 45, hep-ph/0206188.

[72] S. D. Drell and A. C. Hearn, *Phys. Rev. Lett.* **16** (1966) 908.

[73] S. B. Gerasimov, *Sov. J. Nucl. Phys.* **2** (1966) 430.

[74] M. Hosoda and K. Yamamoto, *Prog. Theor. Phys. Lett.* **36** (1966) 425.

[75] **E143** Collaboration, K. Abe *et al.*, *Phys. Rev.* **D58** (1998) 112003, hep-ph/9802357.

[76] **Spin Muon** Collaboration, B. Adeva *et al.*, *Nucl. Instrum. Meth.* **A343** (1994) 363.

[77] N. W. Schellingerhout, L. P. Kok, S. A. Coon and R. M. Adam, *Phys. Rev.* **C48** (1993) 2714, nucl-th/9309012.

[78] K. Gustafsson, COMPASS note 2003-3.

[79] **Spin Muon** Collaboration, D. Adams *et al.*, *Nucl. Instrum. Meth.* **A437** (1999) 23.

[80] A. Abragam and M. GoldMan, *Nuclear Magnetism: Order and Disorder*. Clarendon Press, Oxford, 1982.

[81] G. Mallot, Habilitation thesis, Johannes Gutenberg University.

[82] S. Horikawa, PhD thesis, Nagoya University, 2003.

[83] R. De Masi, PhD thesis, Technische Universitat Munich, 2004.

[84] Y. Giomataris, P. Rebourgeard, J. P. Robert and G. Charpak, *Nucl. Instrum. Meth.* **A376** (1996) 29.

[85] F.Kunne, COMPASS note 2001-2.

[86] B. Ketzer, Q. Weitzel, S. Paul, F. Sauli and L. Ropelewski, *Nucl. Instrum. Meth.* **A535** (2004) 314.

[87] V. Bychkov *et al.*, *Nucl. Instrum. Meth.* **A325** (1993) 158.

[88] P. Barberis *et al.*, COMPASS note 1998-9.

[89] G. Baum *et al.*, *Nucl. Instrum. Meth.* **A433** (1999) 207.

[90] *see http : //wwwcompass.cern.ch/compass/detector/w45/welcome.html.*

[91] G. Ingelman, A. Edin and J. Rathsman, *Comput. Phys. Commun.* **101** (1997) 108, hep-ph/9605286.

[92] G. Ingelman, J. Rathsman and G. A. Schuler, *Comput. Phys. Commun.* **101** (1997) 135, hep-ph/9605285.

[93] T. Sjostrand, L. Lonnblad, S. Mrenna and P. Skands, hep-ph/0308153.

[94] R. Brun, R. Hagelberg, M. Hansroul and J. C. Lassalle,. CERN-DD-78-2-REV.

[95] H. Pereira and J.-M. Le Goff, COMPASS note 2003-4.

[96] V. Blobel and C. Kleinwort, hep-ex/0208021.

[97] J. Zhao, (COMPASS), private communication, 2005.

[98] N. Doshita *et al.*, COMPASS note 2003-5.

[99] C. Bernet, (COMPASS), private communication.

[100] R. Herman, (COMPASS), private communication, 2004.

[101] L. W. Whitlow, S. Rock, A. Bodek, E. M. Riordan and S. Dasu, *Phys. Lett.* **B250** (1990) 193.

[102] **New Muon** Collaboration, M. Arneodo *et al.*, *Nucl. Phys.* **B483** (1997) 3, hep-ph/9610231.

[103] **ZEUS** Collaboration, J. Breitweg *et al.*, *Eur. Phys. J.* **C7** (1999) 609, hep-ex/9809005.

[104] **E143** Collaboration, K. Abe *et al.*, *Phys. Lett.* **B452** (1999) 194, hep-ex/9808028.

[105] **E140X** Collaboration, L. H. Tao *et al.*, *Z. Phys.* **C70** (1996) 387.

[106] **CCFR/NuTeV** Collaboration, U.-K. Yang *et al.*, hep-ex/9806023.

[107] J. P. Berge *et al.*, *Z. Phys.* **C49** (1991) 187.

[108] C. Keppel, (E143), private communication, 2005.

[109] **H1** Collaboration, C. Adloff *et al.*, *Phys. Lett.* **B393** (1997) 452, hep-ex/9611017.

[110] **H1 and ZEUS** Collaboration, T. Latovika, *Eur. Phys. J.* **C33** (2004) s388.

[111] B. Badelek and J. Kwiecinski, *Rev. Mod. Phys.* **68** (1996) 445, hep-ph/9408318.

[112] B. Pawlukiewicz, Diploma thesis, Warsaw University, 2005.

[113] T. V. Kukhto and N. M. Shumeiko, *Nucl. Phys.* **B219** (1983) 412.

[114] I. V. Akushevich and N. M. Shumeiko, *J. Phys.* **G20** (1994) 513.

[115] **New Muon** Collaboration, P. Amaudruz *et al.*, *Nucl. Phys.* **B441** (1995) 3, hep-ph/9503291.

[116] **New Muon** Collaboration, M. Arneodo *et al.*, *Nucl. Phys.* **B481** (1996) 3.

[117] **European Muon** Collaboration, J. Ashman *et al.*, *Z. Phys.* **C57** (1993) 211.

[118] **E665** Collaboration, M. R. Adams *et al.*, *Phys. Rev. Lett.* **68** (1992) 3266.

[119] A. A. Akhundov, D. Y. Bardin, L. Kalinovskaya and T. Riemann, *Fortsch. Phys.* **44** (1996) 373, `hep-ph/9407266`.

[120] H. Abramowicz and A. Levy, `hep-ph/9712415`.

[121] J. Kwiecinski and B. Badelek, *Z. Phys.* **C43** (1989) 251.

[122] B. Badelek and J. Kwiecinski, *Phys. Lett.* **B295** (1992) 263.

[123] J. Bartels, K. Golec-Biernat and H. Kowalski, *Phys. Rev.* **D66** (2002) 014001, `hep-ph/0203258`.

[124] C. Bernet *et al.*, COMPASS note 2005-8.

[125] C. Bernet *et al.*, COMPASS note 2005-9.

[126] O. Helene, *Nucl. Instr. Meth.* **212** (1983) 319.

[127] A. Magnon, (COMPASS), private communication, 2004.

[128] A. Korzenev, (COMPASS), private communication, 2003.

[129] J.-M. Le Goff, COMPASS note 2004-3.

[130] J. Soffer, *AIP Conf. Proc.* **675** (2003) 225, `hep-ph/0212011`.

[131] B. Rosenow, `cond-mat/0107018`.

[132] **COMPASS** Collaboration, E. S. Ageev *et al.*, *Phys. Lett.* **B633** (2006) 25, `hep-ex/0511028`.

[133] M. Diehl, *Phys. Rept.* **388** (2003) 41–277, `hep-ph/0307382`.

[134] **E821** Collaboration, D. W. Hertzog, *Nucl. Phys. Proc. Suppl.* **144** (2005) 191–200, `hep-ex/0501053`.

[135] **SLAC E158** Collaboration, P. L. Anthony *et al.*, *Phys. Rev. Lett.* **95** (2005) 081601, `hep-ex/0504049`.

[136] J. Pretz, COMPASS note 2004-11.

Acknowledgements

I would like to thank my supervisor, Professor Barbara Badełek, for her care, support and enormous patience during my studies at Warsaw University. I am thankful to her for giving me the opportunity to work on COMPASS. I am grateful to Professor Jens Bisplinghoff from Bonn University for funding me a scholarship which gave me the opportunity to work on COMPASS at CERN for one year. I am deeply indebted to Ewa Rondio and Krzysztof Kurek for many interesting discussion and comments concerning experimental and theoretical high energy physics. I would also like to thank my colleagues from Warsaw University: Beata Pawlukiewicz-Kamińska and Grzegorz Brona for their help and friendly atmosphere at work. I am grateful to all COMPASS colleagues - it was a real pleasure to work with you. Last but not least, I would like to thank: Yann Bedfer, Jean-Marc Le Goff, Horst Fischer, Jörg Pretz and my cross-checker Dmitry Pechekhonov. This work was partially supported by KBN grant No. 621/E-78/SPB/CERN/P-03/DWM 576/2003-2006, and the MNII research funds for 2005-2007.

I wish to thank my parents and sister for their patience and support as they are still not fed up with my long learning process. Finally I am deeply grateful to two of my friends, without their help and support this thesis would not be possible to accomplish. My warm thanks go to Catarina Quintans and Kinga Słomińska.